LUND UNIVERSITY

Development and Application of Single-Ended Picosecond Laser Diagnostics

Kaldvee, Billy

2012

[Link to publication](#)

Citation for published version (APA):
Kaldvee, B. (2012). *Development and Application of Single-Ended Picosecond Laser Diagnostics*. [Doctoral Thesis (compilation), Combustion Physics].

Total number of authors:
1

Development and application of single-ended picosecond laser diagnostics

Doctoral Thesis

Billy Kaldvee

Division of Combustion Physics
Department of Physics

LUND
UNIVERSITY

Billy Kaldvee
Division of Combustion Physics
Department of Physics
Lund University
P.O. Box 118
SE-221 00 Lund, Sweden

Populärvetenskaplig sammanfattning

Föreställ dig ett stort rum med bara en liten fyrkantig, ungefär tio centimeter stor, öppning på en av väggarna. Rummet har fem meter långa väggar och är flera meter högt. Golv, tak och alla andra väggar är helt utan öppningar och är inte genomskinliga.

Man misstänker att temperaturen varierar mycket så att det kan vara varmt i en del av rummet och kallt i en annan. Därför vill man kunna få reda på temperaturen i olika delar av rummet, som en väderlekskarta över rummet med temperatur angivet för varje plats.

På samma sätt är man intresserad av att få kartor på vilka ämnen och hur mycket av dem som finns i rummet. Man misstänker att flera farliga ämnen, bland annat det illaluktande ämnet ammoniak, kan finnas i rummet. Även saltångor, som får metallföremål i rummet att rosta sönder, och sot, som är farligt att andas in och kan vara en indikation på ineffektiv förbränning, misstänks finnas i luften.

De första idéerna på hur dessa mätuppgifter ska lösas blir troligen något i stil med: häng termometrar med en halvmeters avstånd i rummet och fyll behållare med luft från olika platser i rummet och skicka till ett laboratorium för provtagning. Tyvärr visar sig dessa idéer vara oanvändbara när villkoren för mätningarna presenteras: du får inte gå in i rummet och du får inte placera någon mätutrustning där inne.

I denna avhandling presenteras en lösning på hur man stående utanför rummet ska kunna ta reda på den efterfrågade informationen. Genom att lysa med laserljus in genom den lilla öppningen och titta på det ljus som kommer tillbaks ut genom öppningen går det att göra kartor över både temperatur och vilka ämnen som finns.

Tänk på en laserpuls som en centimeterlång ljuspuls bestående av många små ljuspartiklar, som flyger genom rummet. Tiden det tar för laserpulsen att färdas till en bestämd plats i rummet och tillbaka till dig igen är enkel att förutsäga eftersom hastigheten ljuspartiklarna färdas med är enormt snabb, men också mycket väl uppmätt: ungefär trehundra miljoner meter varje sekund.

Vet man till exempel att det tar en sekund för laserpulsen att färdas till en plats och tillbaks igen så vet man att den färdats etthundrafemtio miljoner meter dit och lika långt tillbaks. Det blir väldigt korta tider som ska mätas när ljuset studsar på nära håll. Till exempel om ljuspulsen färdas tio meter och där studsar tillbaks igen så tar det bara 0,000 000 07 sekunder innan den är tillbaks.

För att ta reda på temperaturen utnyttjar man sättet som temperatur påverkar luften. När gaspartiklar blir varma så rör de sig snabbare och får mer tomrum emellan sig. Jämför med människor som står tätt packade i en tunnelbanevagn och människor som dansar. När de dansar blir de varma, rör sig snabbare och får mer tomrum emellan sig. Tänk dig ljuspulsen som en boll som ska passera förbi dessa människor. Då är det mycket större chans att lyckas passera förbi dansgolvet än tunnelbanevagnen där bollen troligtvis kommer att studsa tillbaks direkt. På samma sätt är det större chans att ljuspulsen studsar tillbaks när gaspartiklarna är kalla och mer tätt packade.

För att ta reda på vilka ämnen som finns där ljuspulsen passerat utnyttjar man en speciell egenskap som laserljus har, nämligen att färgen är väldigt välbestämd. Alla ämnen absorberar ljus med färger specifika för just det ämnet. Om man låter ljus, med en färg som ett ämne kan absorbera, färdas förbi partiklar av det ämnet så kommer ett antal av ljuspartiklarna att slukas upp av partiklarna. Genom att ändra färgen på ljuset från en färg som absorberas till en som inte absorberas av ämnet går det att ta reda på hur många partiklar av ämnet som passerats av ljuset. Det finns även andra, mer komplicerade, sätt för ljus att växelverka med partiklar, som används för att bestämma om det finns specifika ämnen, sot eller partiklar i luften som ljuspulsen färdas i.

Metoden som presenteras i avhandlingen skiljer sig på två huvudsakliga sätt från de metoder som finns sedan tidigare. Det går att mäta i ett rum med bara en öppning jämfört med andra metoder som bara går att använda på rum med flera öppningar. Dessutom går kartorna över temperatur och ämnen att göra med så noggrann rumsskala (ungefär en mätpunkt varje centimeter) så att metoden är lämplig att använda i rum som är några meter stora. Detta till skillnad från tidigare liknande metoder med en mätpunkt var hundrade meter, vilket endast är användbart för mätningar i atmosfären eller över kilometerlånga sträckor.

Användningsområdet för metoden är framförallt mätningar i stora förbränningsanläggningar, som kraftverk, industriella brännare och stora motorer, till exempel i cylindrarna på fartygsdieselmotorer. Det är uppenbart att det inte går att placera ut mängder av mätinstrument inuti dessa anläggningar. Dels på grund av de hårda fysiska påfrestningar dessa miljöer innebär för mätinstrumenten, men

också för att det kan finnas rörliga delar som omöjliggör utplacering av mätinstrument.

Med möjlighet att bättre kunna karakterisera dessa anläggningar ökar möjligheten för tillverkare och operatörer att åstadkomma en effektivare och renare förbränning som i det långa loppet kan leda till mindre negativ påverkan på människa och natur.

Abstract

Light detection and ranging (lidar), a method for nonintrusive, single-ended, and range resolved measurements, has been developed and applied for combustion related diagnostics. Employing picosecond laser pulse durations and detectors providing temporal resolution on the order of picoseconds, lidar has been applied successfully for both quantitative temperature- and species concentration measurements, obtaining an ultimate range resolution of 0.46 cm.

The use of a streak camera as detector allows two-dimensional imaging in a radar-like fashion, or the possibility to extract time resolved spectral information. The experimental setup, permitting lidar measurements in the near field (<10 m), has been developed and characterized, yielding detailed knowledge of picosecond lidar (ps-lidar) and its feasibility in combustion studies.

Rayleigh scattering thermometry has been conducted in a tube furnace, various flames, and a large scale room fire experiment. The accuracy, under ambient conditions, was within 5% and the measurements were less prone to scattering off dust in the air than traditional perpendicular detection schemes. In premixed ethylene/air flames, the lidar temperatures agree very well with reference data from coherent anti-Stokes Raman Spectroscopy (CARS) measurements up to an equivalence ratio of 1.3. A filtering routine has been developed to be used for applications in which interfering scattering from particles is expected. The filtering routine was applied in the room fire measurements, which resulted in temperature images of two dimensional planes. The temperatures achieved in experiments with a methanol pool fire located in the room agree well with thermocouple measurements and computational fluid dynamics (CFD) simulations, while the signals recorded with a methane gas diffusion flame in the room are dominated by particle scattering, preventing Rayleigh thermometry, but allowing qualitative particle mapping instead.

Tunable optical parametric picosecond lasers were used for differential absorption lidar (DIAL), yielding species concentrations of acetone, ammonia, hydroxyl radical (OH), and potassium chloride (KCl). With a range resolution of 15 cm, a fractional absorption of ~5%, for example corresponding to an ammonia concentration of 40 ppm at ambient condition employing the wavelengths 212.2 and 214.5 nm, sets the detection limit.

Processes based on non-elastic light-matter interaction have been investigated for use with ps-lidar. Raman scattering from liquid samples was used for demonstration of range resolved species determination of nitromethane and hydrogen peroxide. Laser-induced fluorescence (LIF) was used in a demonstration of hydroxyl radical (OH) detection and mapping in a slot burner flame. A model for evaluation of laser-induced incandescence (LII) signals acquired with ps-lidar has been developed and demonstrated. Measurements

of spatial soot volume fraction distributions yielded results that are in excellent agreement with reference measurements carried out with regular right-angle LII.

The following major conclusions can be drawn: ps-lidar is suitable for diagnostics in large scale combustion related devices, particularly devices limited to only one optical access, and, hence, it permits measurements that are currently not possible to realize in any other way, making it a very valuable asset for today's as well as future challenges within energy science.

List of papers

This thesis is based on the following papers, which will be referred to by their Roman numerals in the text.

I. **B. Kaldvee**, A. Ehn, J. Bood, and M. Aldén (2009)
Development of a picosecond lidar system for large-scale combustion diagnostics
Appl. Opt. **48**, B65-B72

II. **B. Kaldvee**, J. Bood, and M. Alden (2011)
Picosecond-lidar thermometry in a measurement volume surrounded by highly scattering media
Meas. Sci. Technol. **22**, 125302

III. **B. Kaldvee**, C. Brackmann, M. Aldén, and J. Bood (2012)
Highly range-resolved ammonia detection using near field picosecond differential absorption lidar
Opt. Express **20**, 20688-20697

IV. **B. Kaldvee**, J. Wahlqvist, M. Jonsson, C. Brackmann, B. Andersson, P. van Hees, J. Bood, and M. Aldén (2012)
Room fire characterization using highly range-resolved picosecond lidar diagnostics and CFD-simulations
Submitted to Combust. Sci. Technol.

V. **B. Kaldvee**, C. Brackmann, M. Aldén, and J. Bood (2012)
LII lidar – range-resolved backward picosecond laser induced Incandescence
Submitted to Appl. Phys. B

VI. A. Ehn, **B. Kaldvee**, J. Bood, and M. Aldén (2009)
Development of a temporal filtering technique for supression of interferences in applied laser-induced fluoresecence diagnostics
Appl. Opt. **48**, 2373-2387

Contents

Wavelength – energy, conversion table

Energy ◄

nm	200	300	400	500	600	700	800	900	1000	1100	1200
cm^{-1}	50 000	33 333	25 000	20 000	16 667	14 286	12 500	11 111	10 000	9 091	8 333

266 nm			532 nm			1064 nm		
$\Delta\lambda$	$\Delta\nu$	Δf	$\Delta\lambda$	$\Delta\nu$	Δf	$\Delta\lambda$	$\Delta\nu$	Δf
0.0071	1.0	0.030	0.028	1.0	0.030	0.113	1.0	0.030
0.0708	10	0.300	0.283	10	0.300	1.132	10	0.300
0.7076	100	2.998	2.830	100	2.998	11.32	100	2.998
3.5380	500	14.99	14.15	500	14.99	56.64	500	14.99

$\Delta\lambda$ [nm], $\Delta\nu$ [cm^{-1}], Δf [THz]

List of abbreviations

CARS	coherent anti-Stokes Raman scattering
CFD	computational fluid dynamics
DIAL	differential absorption lidar
IACM	in situ alkali chloride monitor
lidar	light detection and ranging
LIF	laser-induced fluorescence
LII	laser-induced incandescence
MCP-PMT	microchannel-plate photomultiplier tube
OPG	optical parametric generator
OPA	optical parametric amplifier
ps-lidar	picosecond lidar
RRS	resonance Raman scattering
RST	Rayleigh scattering thermometry
TRF	temporal response function

Chapter 1

Introduction

"In the land of the blind, the one-eyed man is king" was declared by Desiderius Erasmus in the year 1500. This single statement condenses the right to exist and the importance of the measurement technique called picosecond light detection and ranging (ps-lidar) in the field of laser-based remote diagnostics in the near field in general and in combustion diagnostics in particular. Put more simply it means that for studies of combustion environments, ps-lidar offers solutions to measurement situations where currently no other techniques can deliver results.

Combustion is like many other scientific fields very wide and ranges from complex research at the molecular level to heaving undefined waste into large combustors. The aim of combustion research shows the same diversity; from the understanding of detailed chemistry when fuel and oxidizer react, often with thousands of intermediate steps, to experiments dealing with questions on where and how much ammonia should be injected in a 10-m biomass combustor to reduce pollutants. If the aim is not fundamental research, and most of the time even in the fundamental cases, the overall objective is often related to utilizing as much as possible of the chemically bound energy of the fuel, i.e. to improve the combustion efficiency, and reducing the amount of pollutants.

Within the field of laser diagnostics in combustion there is a variety of mature and reliable measurement techniques, developed for several decades, allowing measurements of temperatures, species concentrations, flow fields, etcetera, in combustion applications, mostly at short distances (dm-m). A major drawback with these techniques is that they all need the laser and the detection equipment to

be placed at different positions in relation to the measurement object (bistatic setup). If the measurement is supposed to give a spatially resolved result, one- or two dimensional, the equipment often needs to be placed in an almost perpendicular setup, unless a point measurement technique is used and the equipment is sequentially moved to map out a line or a plane consisting of the individually measured points.

Light detection and ranging (lidar) is a mature technique utilizing temporally resolved detection of the backscattered light to draw conclusions about spatial distribution of quantities such as temperature and species concentrations. It is commonly used for range-resolved remote sensing in, for example, the atmosphere at long distances (km). One of the main advantages with the lidar technique is that it is single ended, meaning that the laser and the receiver, i.e. the equipment for signal collection and detection, are positioned at the same place (monostatic setup), allowing for measurements in any direction and at any distance from the equipment without using a bistatic setup.

As might be clear to the observant reader now, it can simplified be said that ps-lidar gives people in the combustion community a possibility to use many of their traditional techniques even when only one physical access to their measurement object is available. That of course opens up for several justified objections about which techniques that can be used and the limitations of them compared with the traditional use. Hopefully these objections will be responded to in this thesis, but for now, think about the opening quote again, before getting too agitated.

With ps-lidar the highest measurement resolution expected is parts of a centimeter and feasible detection distances could probably be extended up to a couple of tens of meters, depending on which laser diagnostic method that is used, but the normal working range is 2-10 m. With this in mind it is reasonable to claim that ps-lidar is best suited for measurements in pretty large-scale combustion environments and sometimes it might be the only laser diagnostic alternative as well if the facility has only one opening, i.e. one optical access.

Laser diagnostics can be wonderfully simple and straightforward if the laser system is a "turn key – and everything works" kind of system, the diagnostic method is well known, and the optical setup stays fairly simple. If any of these three prerequisites is lacking, the challenge to perform an experiment may – in not too few cases – turn into a veritable mess. In addition, it is of utmost importance to have knowledge about and master the measurement object, or collaborate with someone who does, if the measurements shall lead to any success.

This thesis describes a ps-lidar system, addressing the possibilities and challenges that it implies for combustion diagnostics when it is combined with existing laser techniques. To understand the result of these combinations, deeper, almost – but hopefully not – exhaustively, understanding of the chosen laser technique is needed, which is conveyed in the fundamental light-matter interaction chapter.

In many cases knowledge of all the parts needed to accomplish a ps-lidar measurement campaign are not within the scope of the work presented in this thesis and collaboration with other specialists is needed.

Much of the variety of efforts needed to master the prerequisites within each part of a research project is very important, but, despite that, not necessarily something that results in a scientific paper. The most important ideas and results accomplished during the long learning process, not included in the papers, are accounted for in this thesis to make it easier for someone else working with ps-lidar, or to evaluate whether it could be applicable in a certain measurement situation.

The structure of the thesis is as follows:

- A brief survey of combustion to supply the reader with a basic understanding for a great part of the measurement objects (Chapter 2).

- A description of the most specialized experimental equipment used, including some of the fundamental physics involved (Chapter 3).

- A review of light-matter interaction and how it is utilized in the laser-based methods used in this work (Chapter 4).

- A derivation of the fundamental equations of lidar and the consequences of using picosecond laser pulses and conducting near-field detection (Chapter 5).

- Several chapters describing combinations of ps-lidar and different laser-diagnostic methods. Each chapter contains some practical – more or less useful – applications and some examples of measurement results (Chapters 6-8).

- A non-lidar-specific picosecond laser application, namely temporal filtering for reduction of interfering signals (Chapter 9).

For the part of the thesis describing the fundamental theory (Chapters 2-4) needed to better understand the papers and the part of the work that is more exclusive (Chapters 5-9), the aim is in most parts to highlight the principles of operation and the important consequences for the present work, rather than providing fully comprehensive descriptions.

The overall aim, although not strictly adhered to, is to introduce combustion and some of the basic laser diagnostics to the unfamiliar reader in a more easily digested form, and to be more of a full guide when introducing the ps-lidar concept and research results to the well acquainted combustion community.
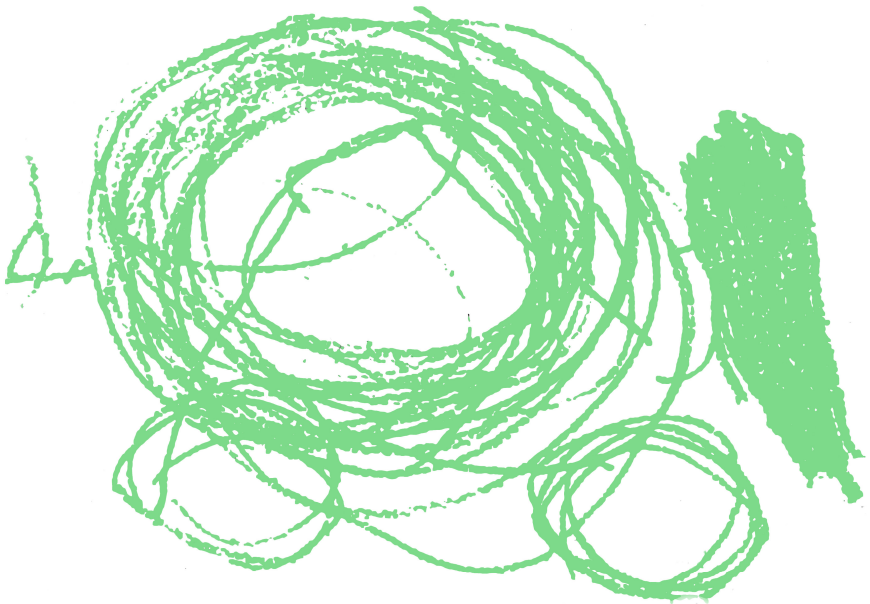
Ville, August 2012

Combustion is an important issue for all ages

Chapter 2

Combustion

Combustion is the process usually referred to as the process of burning. The general description of combustion is that fuel and oxidizer (typically air) are involved in a chemical process that generates energy in the form of heat and often also emits electromagnetic radiation, both visible and invisible for the human eye (Glassman, 1996; Turns, 2000).

The global mechanism of combustion may be expressed as Fuel + Oxidizer $\rightarrow$ Products. A seemingly uncomplicated example is the burning of methane, CH_4, where the global chemical reaction can be written: $CH_4 + 2O_2 \rightarrow CO_2 + 2H_2O$. A reaction written in this way looks very simple and is easy to understand, but the truth is that before one methane molecule has reacted with two oxygen molecules resulting in one carbon dioxide molecule and two water molecules, 163 intermediate steps, including 32 species, have been passed (Wang and Frenklach, 1991).

Some of the short-lived molecules and radicals in the intermediate steps, e.g. OH (hydroxyl radical), C_2, CN, CH, NH, HCHO (formaldehyde), and HCO (formyl radical), are possible to detect with laser diagnostics (Kiefer and Ewart, 2011; Alden et al. 2011). Typical lifetimes of these species at ambient conditions are a few nanoseconds (Eckbreth, 1996). The chemistry will off course be altered if other species are involved in the reaction or erroneous proportions of the reactants are provided in the process. In reality, despite a perfectly balanced mixture of fuel and oxidizer, which is called a stoichiometric mixture, which will be described further in the next section, the reaction never results in only carbon

dioxide and water. Depending on the fuel and oxidizer used, a lot of other minor species (Turns, 2000) will be the result of the combustion process.

2.1 Equivalence ratio

To describe the proportion of fuel and oxidizer involved in a combustion process, e.g. a flame, the equivalence ratio, ϕ, is used:

$$\phi = \frac{m_{fuel}/m_{ox}}{m_{fuel-st}/m_{ox-st}} = \frac{n_{fuel}/n_{ox}}{n_{fuel-st}/n_{ox-st}} = \frac{\dot{V}_{fuel}/\dot{V}_{ox}}{n_{fuel-st}/n_{ox-st}} , \qquad (2.1)$$

where m_{fuel} and m_{ox} are the masses of fuel and oxidizer in the actual process and the corresponding masses with subscripts ending with $-st$ are the corresponding masses in a stoichiometric mixture. A stoichiometric mixture means that fuel and oxidizer are in proportion to balance the chemical reaction to result in only carbon dioxide and water.

As shown in eq. 2.1, the masses in the equation are easily replaced by number of moles, n, or volume flow, $\dot{V}$, which is practical when controlling the equivalence ratio with flow controllers, which are commonly set in liters per minute. The last identity in eq. 2.1 is strictly valid, utilizing the ideal gas law, see eq. 2.4, only if fuel and oxidizer flow have the same temperature and pressure.

The equivalence ratio is defined so that when $\phi = 1$ the mixture is stoichiometric independent of the fuel used. When $\phi > 1$, often called rich mixture, the mixture has an excess of fuel, while $\phi < 1$, often called lean mixture, means that the mixture has a deficit of fuel.

Non-stoichiometric flames have excess molecules during the reactions, leading to products that are often referred to as pollution when speaking about exhaust gases from combustion processes, e.g. CO, nitrogen oxides (NO_x), soot, polycyclic aromatic hydrocarbons (PAH), and, for fuel containing sulfur impurities, sulfur oxides (SO_x). The nitrogen compounds are a direct consequence of having air, containing ~79% nitrogen, as oxidizer instead of pure oxygen.

In Rayleigh scattering thermometry measurements, for example ps-lidar Rayleigh thermometry, particularly PAH and soot particles are troublesome as they disturb the measurements. Both of these are products of rich mixtures as has been investigated for different purposes in e.g. premixed ethylene flames by Bengtsson and Aldén (1990), Maricq et al. (2003) and Wu et al. (2006).

2.2   Temperature effect on molecules

Temperature is a measure of the average kinetic energy, which in thermodynamics is referred to as thermal energy, in an ensemble of molecules (Reif, 1965). The diagnostic methods used in this work mainly utilize the interaction of light with gaseous matter, hence it is of significant importance to know what effect temperature have on molecules in gas phase.

The kinetic energy of a molecule, when considered a thermodynamic system of its own, is divided into internal and external energy modes. The internal energy is contained in vibrational, and rotational motion of the molecule, and in the motion of the molecular electrons. The external energy is contained in translational motion of the molecule. All energy modes are related by the equipartition principle, details of which are out of the scope of this work. Nevertheless, the relation of the energy modes enables temperature measurements by individually probing either any of the internal- or external molecular energy modes.

The dependence of internal energy on temperature is manifested in a probability distribution function over the quantum mechanically discrete energy levels of the molecules (Bransden and Joachain, 2003; Banwell and McCash, 1994).

The energy probability distribution function describes how large fraction of an ensemble of molecules that is expected to be found on each discrete molecular energy level. An increased temperature increases the probability to find a molecule at a higher energy level. The energy probability distribution function, referred to as the Boltzmann equation, can be written as:

$$P_{E_j} = \frac{N_j}{N_{tot}} = \frac{d_j \mathrm{e}^{-E_j/kT}}{Q},$$
(2.2)

where N_j is the number of molecules in energy state j with energy E_j, N_{tot} is the total number of molecules, d_j is the degeneracy of the state, accounting for multiple molecular states at the same energy level, k is the Boltzmann constant, T is temperature, and Q is the partition function, defined as the sum of the expression in the numerator over all possible energy states.

$$Q = \sum_j d_j e^{-E_j/kT} \tag{2.3}$$

Equation 2.2 is only a valid description of the energy distribution when the ensemble of molecules is in thermal equilibrium, meaning that after an interaction the molecules must have long enough time to collide and relax into equilibrium, which for rotational and vibrational energy distributions take on the order of 1 and 100 ns, respectively (Ekbreth, 1996, p. 98).

Equation 2.2 can also be shown to be valid as probability distribution function within each energy mode, meaning, for example, that the distribution of molecules in different vibrational states within a single electronic state can be described, of course using another Q, summing over only the vibrational energy levels within that electronic state.

The dependence of external energy on temperature is described by the temperature-pressure-volume-mass relation given by the ideal gas law, which can be derived from the empirical combined gas law or using statistical mechanics in the kinetic theory of gases (Loeb, 1961, pp 11-29). The ideal gas law:

$$pV = nRT \,, \tag{2.4}$$

where p is pressure, V is volume, n is number of moles, R is the ideal gas constant, and T is temperature, provides an important relation between T and $V / n = A_0 / N$, where N is number density and A_0 is Avogadro's number. In laser-based combustion diagnostics, N is for several methods directly proportional to the detected signal. Consequently, temperature, being inversely proportional to number density, can be inferred from the detected signal, assuming number density is the only temperature-dependent quantity influencing the signal.

When the ideal gas law is applied, it should always be kept in mind that it is a simplification, assuming both perfectly elastic collisions between molecules, and large intermolecular distances. It is therefore only approximately valid under certain conditions. Normal room temperature and pressure are valid conditions and the accuracy increases with increasing temperature and decreasing pressure.

If other conditions prevail, corrections to the ideal gas law exist, for instance the van der Waals equation (Loeb, 1961, p. 145).

$$\left(p + \frac{n^2 a}{V^2}\right)(V - nb) = n\mathrm{R}T \qquad (2.5)$$

The correction constants, a and b, which are species specific, compensate for the attraction between molecules and for the volume occupied by the molecules themselves, respectively.

Chapter 3

Experimental equipment

Most of the experimental equipment used are more or less standard equipment for a laser laboratory, for example optical elements, such as lenses, mirrors, polarizers, and photodiodes, and will therefore not be further discussed here. Elementary optical equipments are well described in numerous textbooks, e.g. (Hecht, 2002; Pedrotti and Pedrotti, 1996). Basic electronic equipment, such as digital delay boxes and oscilloscopes, are thought of as plug-and-play equipment and will not be treated in this chapter either. The fundamental operation of lasers (Svelto, 1989) and molecular energy structure (Bransden and Joachain, 2003) are considered areas that are well known to the readers interested in the equipment used in this work, and will neither be described in full detail here.

The focus will be on some specific features of the equipment, namely mode locking, basic operation of an optical parametric generator (OPG), and the streak camera system, of which the latter often raises a lot of questions when presented.

3.1   Mode-locked picosecond Nd:YAG laser

Mode-locked Nd:YAG lasers have been around since the late 1960's (Osterink and Foster, 1968), but the ways of realizing mode locking have developed substantially since then. A review of the progress to understand the extensive theory behind mode locking is given by Haus (2000), and a helpful description is also given by Demtröder (1993, pp. 617-625).

The cluster of lasers used in this work is based on a mode-locked Nd:YAG laser (Ekspla, PL 2143C), which can either be used directly on its own, utilizing the fundamental, 2nd, 3rd, or 4th harmonic, i.e. 1064, 532, 355, or 266 nm, respectively, or be used to pump an amplifier (Ekspla, APL 70), which 3rd harmonic radiation is used to pump two tunable OPG/OPA systems.

The laser medium, Nd:YAG, is a neodymium-doped YAG (yttrium aluminum garnet - $Y_3Al_5O_{12}$) crystal. The lasing at 1064 nm is generated through a four-level scheme, which offers the well known advantages with a long lived upper energy state, enabling population inversion to build up, and a short lived lower energy state, preventing major self absorption of the stimulated laser light.

Mode locking, also commonly referred to as phase locking, locks all existing longitudinal modes in the laser cavity to be in phase at one position in the cavity at a certain time (Svelto, 1989). The modes allowed in a cavity are determined by the length of the cavity and the gain bandwidth set by the laser medium. For Nd:YAG the gain bandwidth is typically 120 GHz corresponding to 4 cm^{-1} or 0.45 nm at 1064 nm (1064 nm $\Leftrightarrow$ 282 THz $\Leftrightarrow$ 9398 cm^{-1}).

The length of the cavity, L=1.5 m in the present laser (PL 2143C), sets the frequency separation, $\Delta \nu = c/2L = 100$ MHz, between adjacent modes experiencing constructive interference. Thus L determines the number of modes, N, within the laser bandwidth that will ideally experience gain. In our case the bandwidth of 120 GHz allows around 1200 modes with a frequency separation of 100 MHz.

The wider the total bandwidth of the phase locked modes, the shorter the resulting laser pulses will be. Note that the number of phase-locked modes sets the peak intensity of the resulting pulse, while their total bandwidth sets the pulse duration.

In the case of PL 2143C, one pulse from the pulse train, with a typical duration of 30 ps, is out-coupled from the cavity with an optical pulse picker. With L = 1.5 m it can be shown, by summing the sine functions, that the sum of 300 locked modes around 1064 nm results in a Fourier-transform limited pulse duration of 30 ps. In practice, however, it turns out that more than 300 modes have to be phase-locked to achieve this pulse duration.

Figure 3.1 shows the result obtained after summing up phase-locked sine functions, representing different modes. For clarity, each curve has been normalized by $1/N^2$.

The intensities of the curves plotted in fig. 3.1 are calculated using the following relation (Demtröder, 1993):

$$I(t) \propto \frac{\sin^2\left(\frac{1}{2}N\Delta\nu\times t\right)}{\sin^2\left(\frac{1}{2}\Delta\nu\times t\right)} \tag{3.1}$$

There are two main approaches to establish mode locking, namely active and passive mode locking.

In active mode locking either a frequency modulator or an amplitude modulator, which is used in PL 2143C, is positioned inside the laser cavity.

The amplitude modulators, for example a Pockels cell situated in-between two polarizers, are driven by a signal having a frequency, ν_r, that exactly matches the roundtrip frequency, $\Delta\nu$, of the cavity. It may be intuitive to understand the principle of operation in the time domain. Light propagating back and forth in the cavity will experience a net loss due to the passage through the amplitude modulator, which suppresses the light.
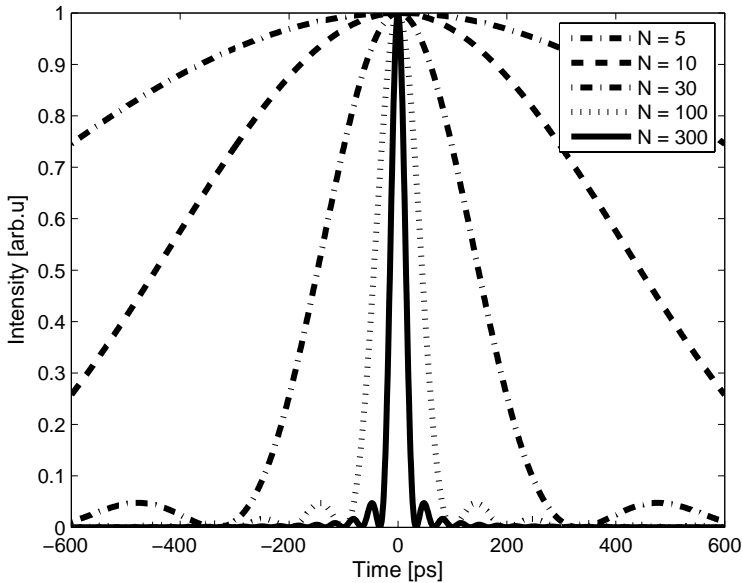

Figure 3.1 *The resulting laser pulses when summing up N adjacent cavity modes, separated by 100 MHz, and being in phase at t = 0. The curves have been normalized by 1/N².*

For a short period of time, the transmission through the amplitude modulator is increased. The light passing the modulator in this time window will after a cavity roundtrip, amplified by stimulated emission, come back to the modulator exactly when the transmission through the modulator is increased again. Only the light passing through the modulator when the transmission is increased will experience a net gain over a cavity roundtrip, thus the result is a short pulse propagating back and forth in the cavity, experiencing net gain each roundtrip.

The operation can also be understood in the frequency domain by the introduction of sidebands at the modulation frequency, around the central frequency of the gain medium, v_g, at $v_g \pm v_r$, which exactly corresponds to the frequency of the adjacent cavity modes. The adjacent modes will thus be in phase with the central mode, and then, with the same reasoning, the adjacent modes will be in phase with their adjacent modes, and so forth, until all modes are phase locked.

Passive mode locking may be accomplished by inserting a saturable absorber in the laser cavity. The absorber will be saturated when the light intensity exceeds a certain threshold. By carefully designing the system, the duration of a laser pulse passing the absorber will shorten with each roundtrip, until steady state is reached, since only the central temporal part of the laser pulse has high enough intensity to experience a net gain.

In the laser used in this work, mode locking is accomplished by a combination of passive mode locking, based on a solid-state absorber, and active mode locking utilizing an amplitude modulator. The laser is pumped by flash lamps, with a pulse being coupled out by the optical pulse picker each flash, and is hence operating at the repetition frequency of the lamps, i.e. 10 Hz.

3.2 Optical parametric- generation/amplification (OPG/OPA)

An optical parametric generation / optical parametric amplification (OPG/OPA) system is tunable over a broad range of wavelengths. The lasers used in this work (Ekspla, PG401-P80-SH) are tunable from 210 to 2300 nm, with laser pulses having a spectral width of <4 cm^{-1} and a duration of ~80 ps.

The theory of optical parametric generation is based on the concept of induced non-linear polarization in combination with phase matching in a birefringent crystal. The basic ideas, briefly described here, are further discussed

and illustrated in the textbooks by Svanberg (2001), Demtröder (1993), Svelto (1989), and Boyd (1992), among which Boyd is providing in-depth description of the physical process.

The polarization of a medium can be expressed as a function of the susceptibility tensor, $\widetilde{\chi}$:

$$\overline{P} = \varepsilon_0 \left(\widetilde{\chi}^{(1)} \overline{E} + \widetilde{\chi}^{(2)} \overline{E}^2 + \widetilde{\chi}^{(3)} \overline{E}^3 + ... \right) \tag{3.2}$$

The term responsible for often utilized non-linear optical effects, such as frequency doubling (referred to as second harmonic generation, SHG), sum frequency generation (SFG), and difference frequency generation (DFG), is the quadratic term. The OPG- and OPA effects are sometimes referred to as special cases of DFG. Large amplitude of the electric field is needed for this term to be on the order of the linear term.

An electromagnetic wave containing two components with different frequencies, ω_1 and ω_2, can be expressed as:

$$\overline{E} = \frac{1}{2} \left\{ \overline{A}_1 \left(e^{i(\omega_1 t - k_1 z)} + e^{-i(\omega_1 t - k_1 z)} \right) + \overline{A}_2 \left(e^{i(\omega_2 t - k_2 z)} + e^{-i(\omega_2 t - k_2 z)} \right) \right\} \tag{3.3}$$

Inserting this electromagnetic field into the quadratic term of eq. 3.2 at a fixed position, $z=0$, yields

$$\overline{P} = \varepsilon_0 \widetilde{\chi}^{(2)} \frac{1}{2} \left\{ \begin{array}{l} \left(\overline{A}_1^2 + \overline{A}_2^2 \right) + \overbrace{\frac{1}{2} \overline{A}_1^2 \left(e^{i(2\omega_1 t)} + e^{-i(2\omega_1 t)} \right)}^{SHG_1} + \\[2mm] \overbrace{\frac{1}{2} \overline{A}_2^2 \left(e^{i(2\omega_2 t)} + e^{-i(2\omega_2 t)} \right)}^{SHG_2} + \\[2mm] \overbrace{\overline{A}_1 \overline{A}_2 \left(e^{i((\omega_1 + \omega_2)t)} + e^{-i((\omega_1 + \omega_2)t)} \right)}^{SFG} + \\[2mm] \overbrace{\overline{A}_1 \overline{A}_2 \left(e^{i((\omega_1 - \omega_2)t)} + e^{-i((\omega_1 - \omega_2)t)} \right)}^{DFG(OPG\&OPA-effects)} \end{array} \right\} \tag{3.4}$$

Note that the direction of $\overline{P}$ and the incoming electromagnetic wave, $\overline{E} = \overline{E}_1 + \overline{E}_2$, does not need to be the same, since $\widetilde{\chi}^{(2)}$ governs the relation of the directions.

Generally, in a crystal, the electromagnetic field components, corresponding to the different terms in eq. 3.4, and the polarizing field, $\overline{E}$ have different phase velocities, v_p, and momentum, $p = \hbar k$, due to the relationships $v_p = c/n(\omega)$ and $k = \omega/v_p$, where n is the refractive index and k is the wave number.

Using the fact that $\overline{E}$ and the polarization term of interest, $\overline{P}_x$, have different polarizations together with the effect of having different refractive indices along the orthogonal axes in a birefringent crystal, it is possible, by tilting the crystal into an optimal angle, to achieve constructive interference between the electromagnetic waves, $\overline{E}_{ind}$, induced by $\overline{P}_x$ .at all positions. If $\overline{E}$ and $\overline{E}_{ind}$ propagate through the crystal in phase, i.e. with equal v_p, $\overline{E}_{ind}$ will build up and experience gain at each position, as the induced polarization, $\overline{P}_x$, will be in phase with $\overline{E}_{ind}$.

Optical parametric generation in a crystal may be thought of as a two parallel DFG processes, satisfying $\omega_1 = \omega_2 + \omega_3$ to fulfill energy conservation of the total process. Photons from a pump beam of frequency, ω_1, create two photons at the signal and idler frequencies, ω_2 and ω_3, respectively, which definition states that $\omega_2 > \omega_3$. The generated frequencies ω_2 and ω_3 are determined by the phase matching conditions, which may be obtained by considering the conservation of momentum for the photons involved in the three-wave mixing process.

$$k_3 = k_1 - k_2 \quad \text{alternatively} \quad k_2 = k_1 - k_3 \qquad (3.5)$$

From these conditions it is again seen that v_p of the three waves must be equal, which is fulfilled by arranging the crystal so that $n(\omega)$ is equal for all three waves.

To initiate the parametric process, i.e. before signal and idler waves are present, quantum noise supplies the process with an initial photon fulfilling the phase matching requirement.

In the OPG/OPA system used in the present work all non-linear crystals are made of Beta-barium borate (BBO), a negative uniaxial birefringent material transparent in the range 190-3500 nm. The lasers are pumped by 355-nm radiation from the amplified Nd:YAG laser (APL 70) and an initial double pass optical parametric generator (defined as optical parametric oscillator by the manufacturer) delivers a signal wave (the idler is suppressed), which is purified, by letting the wave, dispersed by a grating, pass through a pinhole.

The signal is then amplified twice in optical parametric amplifiers, OPA1 and OPA2, where the pump beam and the signal beam overlap in time and space at the crystals. The idler wave is separated from the signal after OPA2 for use as idler

output from the laser, and the residual signal wave is used as it is or frequency doubled to reach the desired ultraviolet wavelengths.

3.3   Streak camera

The streak camera (Optronis, Optoscope), provides a time resolved image of a slit in front of its objective. Thus, it gives the user the possibility to obtain a highly time resolved image of whatever is imaged onto that slit (Bradley et al., 1971; Schelev et al., 1971).

A typical application of the camera is to record a time resolved image of an event, e.g. fluorescence, taking place along a line in the measurement volume, which can be time resolved for lifetime studies (Bergano et al., 1983; Ehn et al., 2012a). Another application is to separate events that have different temporal characteristics, for example fluorescence and scattering as demonstrated in Paper VI. The streak camera may also be used to temporally resolve the signal from backscattered light induced by a laser pulse travelling away from the camera, which is how it is used in ps-lidar measurements.

A streak camera is schematically illustrated in fig. 3.2. The principle of its operation is that the slit in front of the objective is imaged onto a photocathode, converting the optical signal to electrons. The electrons are further accelerated towards the anode by an electric field and while they propagate towards a micro-channel plate (MCP) in front of the anode, the electrons are perpendicularly deflected by a very rapid voltage ramp applied between two deflection plates. After being perpendicularly deflected a distance proportional to the prevailing voltage of the high voltage ramp, the electrons are multiplied in the MCP, after which a phosphor screen converts them into photons. The phosphor screen is coupled to a CCD chip, which then acts as the final detector of the signal.

The streak camera used in this work has a 19.5×14.4 mm CCD chip with 1392×1024 pixels. Streak rates from 10 ps/mm (fastest streak) to 1 ns/mm (slowest streak), governed by the speed of the voltage ramp, are available along the axis with 1392 pixels (time-axis). The fastest and slowest streak corresponds to a total time span of 195 and 19.5 ns, respectively. Each point in a time span, from the start to the end of the voltage ramp, corresponds to a certain position along the time-axis. In a resulting streak camera CCD image, the horizontal axis corresponds to the time-axis and the vertical axis corresponds to the slit height, whatever is imaged onto it.
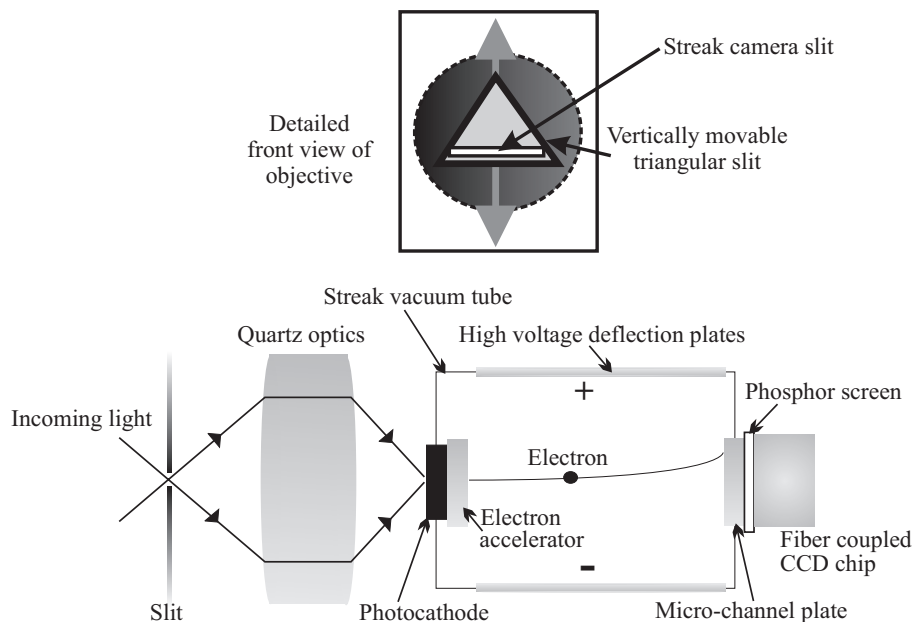
Figure 3.2 *A schematic image of a streak camera. At the top, the streak camera slit, situated in front of the objective, is depicted. At the bottom the operation of the camera is illustrated. The incoming light passes through the lens system onto the photocathode, where electrons are emitted and accelerated towards the micro-channel plate. After being multiplied in the MCP, the electrons impinge on a phosphor screen where they are converted to photons that are detected by a CCD.*

The streak camera is capable of providing a temporal resolution of 2 ps, which is obtained at the highest streak rate (10 ps/mm). It should be pointed out that in order to reach this resolution the slit width needs to be small, typically 50 microns or less.

The streak camera slit placed horizontally at the entrance of the objective, is equipped with a micrometer screw enabling adjustment of the slit width from 0-5000 μm, and a vertically adjustable triangular opening, referred to as fish-tail slit, that enables a coarse continuous slit height reduction from 1.1 to 0 cm when moved vertically (see detailed front view of objective in fig. 3.2). The streak camera can be triggered externally by the laser for use in laser experiments.

Chapter 4

Light-matter interaction

Light and matter interacts in different ways depending on the properties of the light and the matter. Basically, the wavelength, polarization, and intensity of the light, together with the structure and density of matter decide what kind of interaction to expect. Two common light-matter interaction processes are scattering and absorption.

The result of a scattering process is normally divided into two categories: elastic and inelastic scattering, depending on if the scattered light has the same wavelength as the incoming light (elastic) or not (inelastic), i.e. if any energy has been transferred between light and matter. Elastic scattering is further divided into Rayleigh and Mie scattering depending on the relationship between the size of the scattering particles and the wavelength of the light. Molecules with diameter smaller than the wavelength belong to the Rayleigh category, while scattering off larger particles is described by Mie theory.

Absorption of light, which may occur when the energy of a photon interacting with a molecule matches the difference between two energy levels in the molecule (see fig. 4.1 for molecular energy levels), can be followed by many different energy transfer processes, internal and external, in a molecule. Some of the absorption effects being externally measurable are the decrease in the transmitted laser pulse energy when passing through the absorbing media, and one of the subsequent processes, namely fluorescence, which typically is a broadband emission of light, often shifted towards longer wavelengths relative to the excitation light.

To aid the reading of the following sections, an overview of a typical molecular energy structure is provided in fig. 4.1, where electronic, vibrational and rotational energy levels are schematically shown
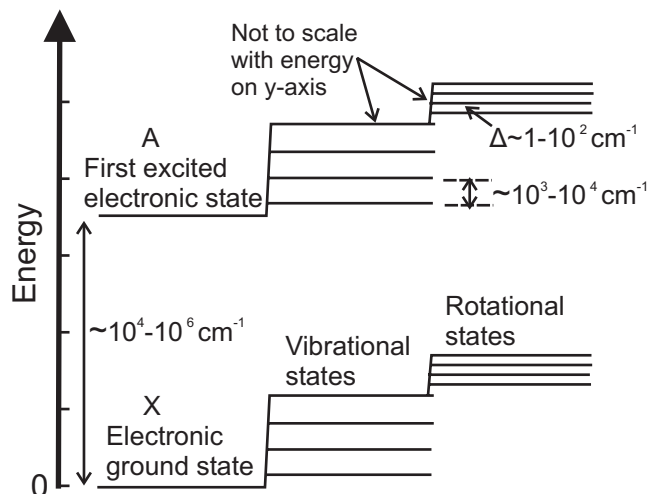

Figure 4.1 *A schematic molecular energy structure. Energy states for different electron orbitals, as well as vibrational- and rotational motion are depicted together with typical values on the energy difference between two adjacent states.*

4.1 Elastic scattering

The classical picture of the origin of scattered light, in the Rayleigh regime (diameter of scatterer < wavelength), is described through electromagnetic dipole radiation. For a thorough description, partly followed here, see (Miles et al., 2001), and for an even more elaborate analysis of the fundamental equations of Rayleigh scattering, the work published by Eberhard (2010) and references therein are recommended.

The electromagnetic field induced by an oscillating dipole (only strictly valid for spherically symmetrically scatterers) is given by:

$$E_{ind}(\phi,r,t) = \frac{\omega^2 p \cdot \sin\phi}{4\pi r \varepsilon_0 c^2} e^{i(\omega t - kr)} = \frac{p\pi \cdot \sin\phi}{\lambda^2 r \varepsilon_0} e^{i(\omega t - kr)} \qquad (4.1)$$

where ω is the angular frequency of the electromagnetic wave, ϕ is the angle between the direction of the oscillating dipole moment, $\bar{p}$ with magnitude p, and the direction in which the induced wave is observed, k is the wavenumber, r is the distance from the dipole, ε_0 is the vacuum permittivity, and c is the speed of light. See figure 4.2 for illustration of ϕ, r, and $\bar{p}$

The factor ω^2 is caused by the radiation being proportional to the acceleration of charges, which follows the acceleration of the electric field, i.e. the second derivative of the harmonic oscillation at frequency ω. The $\sin(\phi)$ factor is the projection of the oscillating dipole from the viewing angle, leading to $E = 0$ when observed from above or beneath the dipole ($\phi = 0$ or $180°$).
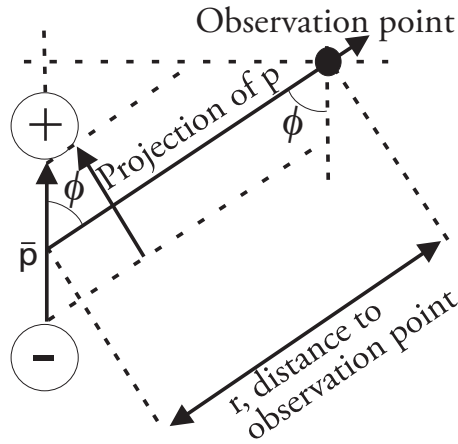
Figure 4.2 *Illustration of the geometric relationship between polarization axis, ϕ, observation point, and the projection of the polarization **p** onto the plane facing the observation point.*

The intensity observed from an oscillating dipole is, by using the definition $I = c\varepsilon_0|E|^2/2$, on eq. 4.1 given by

$$I_{ind}(\phi, r) = \frac{c}{2} \frac{p^2 \pi^2 \cdot \sin^2 \phi}{\lambda^4 r^2 \varepsilon_0} \qquad (4.2)$$

The oscillating dipole moment is induced by the incident electric field E_{in}, with intensity I_{in}, and the molecular polarizability tensor, $\tilde{\alpha}$,as:

$$\bar{p}(t) = \tilde{\alpha}\bar{E}_{in}(t), \qquad (4.3)$$

which, put into eq. 4.2, assuming only diagonal, and equal, elements in the polarizability tensor, i.e. isotropic polarizability α, yields:

$$I_{ind}(\phi, r) = \frac{\pi^2 \alpha^2 \cdot \sin^2 \phi}{\lambda^4 r^2 \varepsilon_0^2} I_{in} \qquad (4.4)$$

By introducing a relation between the polarizability and the index of refraction, referred to as the Lorentz-Lorenz equation (Born and Wolf, 1980, p. 98, see Miles et al. 2001, p. R36), which in descriptions of dense media is known as the Clausius-Mossotti relation (Feynman, 1965), the scattered intensity as a function of the observers position in space, from one dipole is, given by:

$$I_{ind}(\phi, r) = \left(\frac{n^2 - 1}{n^2 + 2} \right)^2 \frac{\pi^2 9 \cdot \sin^2 \phi}{N^2 \lambda^4 r^2} I_{in}, \qquad (4.5)$$

where n is the refractive index and N is the total number density of the gas. Utilizing the fact that $n^2 \approx 2n\text{-}1$ and that $9/(n^2+2) \approx 3$ for n very close to 1 and setting the angle, ϕ, to 90° as it will always be when collecting backscattered light (The propagation axis of backscattered light is always perpendicular to the polarization axis. When collecting perpendicularly scattered light, the collection angle relative to the polarization axis is free of choice 0-180°), eq. 4.5 ends up in a common expression for the intensity of Rayleigh scattered light (Eckbreth, 1996):

$$I_{ind}(\pi/2, r) = \left(\frac{n - 1}{N} \right)^2 \frac{4\pi^2}{\lambda^4} \cdot \frac{I_{in}}{r^2} \qquad (4.6)$$

The movement of the scattering molecules induces density fluctuations in the medium, causing the phase of the induced scattering to lose its coherence. The intensity contributions from the scatterers are therefore incoherent and the intensities of the individual scatterers are added up, instead of summing the electric fields as with coherent waves, which is the reason for scattered intensity being proportional to number density of scatterers.

The spectral features of Rayleigh scattering are not accessible using picosecond pulses due to the spectral width of the laser light. However, polarization is a property that is measureable with picosecond laser pulses, and hence it could be of interest to shortly mention the composition of what should be referred to as Rayleigh scattering (Young, 1981).

For Raman active molecules (see Section 4.2 for Raman) the scattered light, detected without any spectral filter, consists of pure elastic scattering, without any internal energy transfer in the molecules, the Stokes and anti-Stokes rotational Raman lines, and the vibrational Raman lines.

The term Rayleigh scattering should be used for the elastic- and the rotational Raman scattering. The pure elastic scattering, called the Cabannes line, comprises both the highly polarized component emitted without any change of state in the molecule, called the Placzek trace scattering, and the Raman rotational Q-branch which is weaker and in most cases depolarized since a molecular reorientation, including a change of state but no energy transfer, has occurred. The Cabannes line has spectral features, appearing as sidebands reflecting the speed of sound, called Brillouin-Mandel'shtam scattering. The intensity of the Brillouin-Mandel'shtam scattering is dependent on density fluctuations in the medium and increases with pressure/temperature ratio. The residual central peak between the acoustic sidebands is called the Landau-Placzek line.

Typical spectral magnitudes are percents of cm^{-1} for the Cabannes line, including broadening due to molecular motion, tens of cm^{-1} for the rotational Raman line separation and thousands of cm^{-1} for vibrational Raman line separation.

4.2   Inelastic scattering (Raman)

If the molecular polarizability tensor, given in eq. 4.3, changes periodically with time due to vibration and/or rotation of the molecule, the equation can be rewritten as:

$$\overline{p}(t) = \left(\widetilde{\alpha}_0 + \frac{1}{2} \Delta\alpha \sin(\omega_{Raman} t) \right) \overline{E}_{in}(t), \qquad (4.7)$$

where $\Delta\alpha$ is the amplitude and ω_{Raman} is the angular frequency of the change in polarizability induced by molecular vibration or rotation. The angular frequency, ω_{Raman}, corresponds to the energy difference between two molecular states, see fig. 4.1, involved in an allowed molecular transition. Note, that it is the frequency of the energy difference and not the frequency corresponding to the energy of the vibrational or rotational state itself that governs the time dependence of the polarizability.

The resulting polarization components are:

$$\overline{p}(t) = \vec{\alpha}_0 \overline{A}_{in} \sin(\omega_{in} t)$$
$$+ \frac{1}{2} \Delta\alpha \cdot \overline{A}_{in} \left(\cos\left[(\omega_{in} - \omega_{Raman})t\right] + \cos\left[(\omega_{in} + \omega_{Raman})t\right] \right), \qquad (4.8)$$

with $\overline{A}_{in}$ being the amplitude of $\overline{E}_{in}(t)$. By inserting this polarization in eq. 4.2, the observed intensity is obtained, which thus is a multiplication of $\overline{p}^2(t)$ with a time independent function, $J(\phi,r)$, depending on the position of the observer. The characteristic $1/\lambda^4$ dependence of the Raman signal is also contained in $J(\phi,r)$. Accordingly all time dependent parts are unchanged in the observed electric field, where the terms with frequency shifted $\pm\omega_{Raman}$, called Raman scattering (Raman and Krishnan, 1928), enable really powerful spectroscopy as the vibrational and rotational structure is revealed in the scattered light, irrespective of the wavelength of the incident laser light.

The intensities of the Raman lines at $\omega_{in}\pm\omega_{Raman}$, dependent on $\Delta\alpha$, cannot be predicted by classical electromagnetic wave theory, but requires a quantum mechanical treatment, although some predictions about the line strengths, and existence of the lines, can be made from the classical approach.

It is observed in eq. 4.8 that it is an absolute necessity that $\Delta\alpha$ must not be equal to zero for the Raman scattering to appear. The line strength, proportional to $\Delta\alpha$, of a vibrational Raman transition depends on the derivative $d\alpha/dx$ in the equilibrium position, with x being the variable that changes during the molecular motion. The line strength of a rotational Raman line depends on the anisotropic polarizability, γ, describing the difference in polarizability along the molecular axes. Thus it is easy to realize that, for example, symmetrical molecules do not exhibit rotational Raman structure, since it lacks anisotropic polarizability, and that symmetric stretch vibrational Raman modes give rise to intense Raman lines.

As already mentioned, quantum mechanical calculations are needed in order to determine Raman cross sections, which is also the case for deriving the selection rules for allowed transitions.

In summary, some basic characteristics of Raman scattering are (Demtröder, 1993): The intensity is proportional to the population density in the initial energy state, the intensity of the incident laser light, and the Raman scattering cross section. Furthermore, the cross section is proportional to $1/\lambda^4$, and increases dramatically when λ, the laser light wavelength, approaches the wavelength

corresponding to a resonant transition of the molecule, so-called resonance Raman scattering (RRS).

4.3 Absorption

Molecules absorb light at wavelengths matching the energy, $E = hc/\lambda$, of an allowed transition between two molecular energy levels. The energy levels are treated in many fundamental textbooks on molecular spectroscopy (Svanberg, 2001; Banwell and McCash, 1994; Bransden and Joachain, 2003). The absorption processes utilized in the current ps-lidar work are due to transitions between different electronic states of the molecules, which are often available in the ultraviolet regime. The electronic energy states are designated X, A, B, C… from lower to higher internal energy in the molecule, see fig. 4.1 (if a state has different spin multiplicity with respect to the preceding state it is written with a lowercase letter). A transition to a higher electronic state simplistically corresponds to a redistribution of the electrons to more energetic orbitals.

In addition, each electronic absorption band has vibrational and rotational structure, more or less resolved due to molecular complexity and the spectroscopic equipment used. In fig. 4.3 an absorption spectrum of ammonia, NH_3, is shown, which is of interest as it was used in DIAL measurements further described in Section 6.2.2.
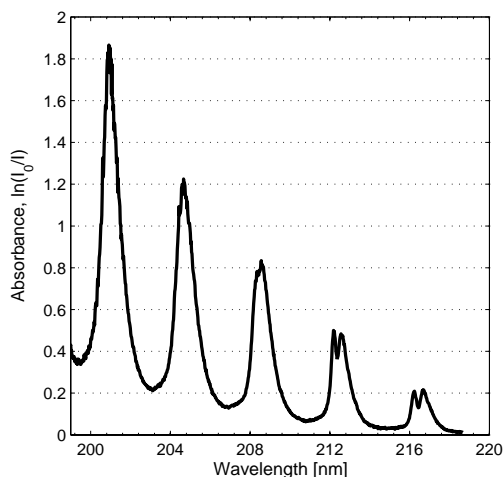

Figure 4.3 *Spectrum of the NH_3 transition $A \leftarrow X(\, v_2 = 0)$ for v_2 = 0-4 in the A-state.*

The spectrum contains part of the absorption structure corresponding to the transition A←X(v_2=0), i.e. a v_2 progression, meaning that the vibrational level of v_2, is fixed in the ground state, X, while changing in the upper state (v_2 = 0-4 from right to left in this spectrum) (Duncan, 1935; Cheng et al., 2006; Rosmus et.al., 1987). The normal vibration mode v_2 corresponds to a symmetric bend of the N-H bonds, which can be seen as an almost rigid, triangular plane formed by the H atoms moving up and down along the symmetry axis through the NH_3 molecule. The broad underlying structure is due to the predissociative nature of the excited electronic state.

As light, with a certain spectral distribution Ω of initial intensity I_0, is passing through an absorbing medium, a distance dL, the fraction of the light being absorbed is proportional to the number of absorbing molecules, dn. The intensity changes as:

$$\frac{\mathrm{d}I}{I} = -k\,\mathrm{d}n = -kC\theta\,\mathrm{d}L = -\sigma_{abs}C\,\mathrm{d}L \qquad (4.9)$$

where, σ_{abs}, is the cross section (cm^2), C is number density (cm^{-3}), and θ, only used as an intermediate variable, is the area of the interaction region. Integrating eq. 4.9, assuming a passage from 0 to L and intensity decreasing from I_0 to I_L, yields

$$\int_{I_0}^{I_L}\frac{1}{I}\mathrm{d}I = -\sigma_{abs}C\int_0^L \mathrm{d}l \Leftrightarrow \ln\frac{I_0}{I_L} = \sigma_{abs}CL = A \qquad (4.10)$$

This equation is referred to as the Beer-Lambert law, stating that the absorbance, A, is proportional to the number density, C, and the path length through the absorbing medium, L. For this linearity to be true it is a prerequisite that the product CL (often referred to as column density) is not too high since it will set down the effective absorbance. This can be thought of as the molecules obscuring each other when the light passes.

To assure linearity of the absorbance, it can be measured while increasing C, and if the linearity holds, the resulting function will be a straight line. Equation 4.10 can be rewritten as a function describing the expected transmitted intensity after the passage through an absorbing medium:

$$I_L = I_0 e^{-\sigma_{abs}CL} \qquad (4.11)$$

The effective absorption cross section depends on the spectral distribution, Ω, of the passing light. Theoretically, the effective absorption cross section can be calculated as the integral of the product of the spectral distribution, and the pure molecular absorption cross section, at the current conditions.

In practice this might be difficult to do, for example if no data at the current conditions are available or if the reference data were not recorded with high enough spectral resolution. Then, if possible, it is suitable to make a measurement of the absorption cross section with exactly the same equipment that will be used in the study. Figure 4.4 shows the result of such a measurement on NH_3, scanning across the transition $A(v_2=1)\leftarrow X(v_2=0)$. The laser used was the OPG/OPA described in Section 3.2 having a spectral width specified to <4 cm^{-1} corresponding to <0.02 nm at 213 nm.
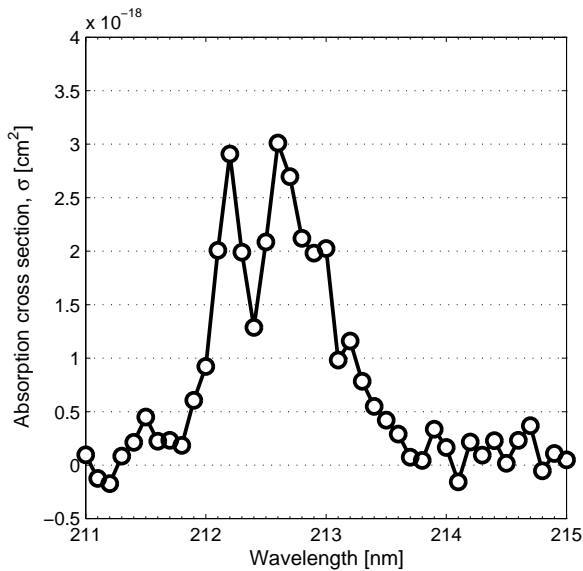

Figure 4.4 *Absorption spectrum, with evaluated absorption cross sections of the NH_3 transition $A(v_2=1)\leftarrow X(v_2=0)$.*

4.4 Laser-induced fluorescence (LIF)

Over the course of this thesis work, laser-induced fluorescence has been used briefly to demonstrate the ability to make qualitative fluorescence-based species detection using ps-lidar, and in time-gated perpendicular fluorescence imaging to demonstrate discrimination against elastic scattering, utilizing the time domain, in Paper VI.

Fluorescence may have a strong potential for qualitative species mapping employing ps-lidar, avoiding the experimentally more cumbersome DIAL setup. Therefore, fluorescence will be shortly described in order to aid the understanding of some of the basic principles responsible for the spectral and temporal behavior of a fluorescence signal, following the outline in Eckbreth (1996). Laser-induced fluorescence and planar laser induced fluorescence, for two dimensional measurements, are further described and reviewed in (Kohse-Höinghaus, 1994; Aldén et al, 2011)
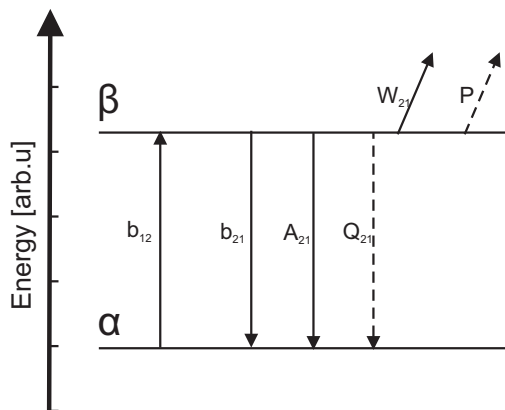

Figure 4.5 *A simple model of a molecular energy structure containing only two levels, α and β. Processes responsible for changing the molecule's energy are depicted indicated with their rate constants.*

The emission of fluorescence is one out of many possible processes following upon absorption (described in section 4.3). Instead of considering the complete molecular energy structure, as schematically shown in fig. 4.1, a simplified LIF model may be described using only a two-level system, as depicted in fig 4.5.

In fig. 4.5 rate constants, which multiplied with a population density give the rate of population change, are defined for different processes:

b_{12}	-	Absorption rate
b_{21}	-	Stimulated emission rate
A_{21}	-	Spontaneous emission rate (fluorescence)
Q_{21}	-	Quenching rate
W_{21}	-	Photoionization rate
P	-	Predissociation rate

The b constants are defined as

$$b = \frac{B}{c} \int_{\omega} I(\omega)g(\omega)\mathrm{d}\omega, \qquad (4.12)$$

With B designating the Einstein coefficient for stimulated emission or absorption, $g(\omega)$ describing the lineshape of the transition, and $I(\omega)$ being the spectral intensity distribution (in units of $W/(cm^2 \times s)$) of the laser. The relation of cross sections, σ, rate constants, and Einstein coefficients was carefully sorted out by Hilborn (1982), who showed the useful relation:

$$B = \frac{c}{\hbar\omega}\sigma_0 \qquad (4.13)$$

Two coupled rate equations describe the time-dependent population transport into and out from the two levels α and β, with N being the population of the levels.

$$\frac{\mathrm{d}N_\alpha}{\mathrm{d}t} = -N_\alpha b_{12} + N_\beta\left(b_{21} + A_{21} + Q_{21}\right) \qquad (4.13)$$

$$\frac{\mathrm{d}N_\beta}{\mathrm{d}t} = -N_\beta\left(b_{21} + A_{21} + Q_{21} + W_{21} + P\right) + N_\alpha b_{12} \qquad (4.14)$$

If clever assumptions concerning initial populations of the states and the timescales of different processes are made, sometimes combined with experimental approaches like saturated LIF (Daily, 1977) or predissociative LIF (Andresen et al., 1988), the investigation of excited states is vastly simplified, and the system of equations can be analytically solved for different scenarios to make quantitative calculations of number density of the fluorescing molecule possible.

The challenging quenching term in eqs 4.13 and 4.14 can also be accounted for with the highly cumbersome approach of doing separate Raman measurements

in connection to the LIF measurements to calculate the quenching rate (Barlow et al., 1989).

In single-ended spatially resolved mapping of molecules using ps pulses, the lifetime of the fluorescence will decrease the spatial resolution, see eq. 5.7, due to the lifetime of the upper state, τ_β, being much longer than the laser pulse duration. If the lifetime is known though, the spatial resolution may in some cases be restored, see Section 8.1. Thus it is of significant interest to know the lifetimes of the fluorescing states. When the laser pulse has passed the volume of molecules and excited a fraction of them into the β-state, neglecting potential predissociation and photoionization effects, eq. 4.14 reduces to

$$\frac{\mathrm{d}N_\beta}{\mathrm{d}t} = -N_\beta \left(A_{21} + Q_{21} \right) \tag{4.15}$$

which is readily solved

$$N_\beta = N_{\beta 0} \mathrm{e}^{-(A_{21}+Q_{21})t} \tag{4.16}$$

The intensity of the fluorescence is proportional to N_β. Hence, the LIF signal will have the same time dependence as the population in state β, which is characterized by the decay constant, τ.

$$\tau = \frac{1}{\left(A_{21} + Q_{21} \right)}. \tag{4.17}$$

The spontaneous emission rate constant, A_{21}, is an intrinsic property of the molecule. The quenching rate constant, Q_{21}, on the other hand is dependent on temperature, pressure, and concentration of other molecules in the probe volume. The quenching rate constant can be theoretically calculated as (Crosley, 1989a; 1989b):

$$Q_{21} = \sum_i \sigma_{Q_i} C_i \sqrt{\frac{8\mathrm{k}T\left(m_1 + m_2 \right)}{\pi m_1 m_2}} , \tag{4.18}$$

where σ_{Qi} is the quenching cross section, C_i is the number density, and m_2 is the mass, respectively, of the i:th colliding species. The constant k is the Boltzmann constant, T is the temperature, and m_1 is the mass of the fluorescing molecule

Considering a more realistic molecular energy structure, schematically shown in fig. 4.1, both radiationless vibrational- and rotational energy transfers (VET, RET) will take place upon excitation to the upper electronic state. One consequence of that is a fluorescence emission spectrum that will contain many different wavelengths and often will be shifted towards longer wavelengths.

Then, the modeling of the fluorescence signal, in terms of both number density and decay constants, becomes significantly more complicated. The decays are often multiexponential due to different rate constants of the upper state manifold. This complex modeling is needed when it comes to calculating both number density and decay constants from time resolved- (Lucht et al., 1980; Ehn et al., 2012b) or time integrated fluorescence spectra.

Chapter 5

Picosecond light detection and ranging (ps-lidar)

5.1 Lidar and the lidar equation

Lidar (light detection and ranging) is a well-established and mature method for remote detection, characterization, and ranging of objects and gaseous plumes consisting of molecules, particles, and aerosols. Lidar has been used extensively in atmospheric research, for example cloud research, for a variety of purposes, such as species detection, wind speed measurements, and temperature measurements.

In addition to regular atmospheric lidar more exciting applications of lidar, such as submarine lidar for seafloor inspection (Harsdorf et al., 1999) and lidar with high range resolution, ~15 cm, for investigation of particulate matter in automotive exhaust gases across roads (Mazzoleni et al., 2010) have been reported. A novel lidar modification termed 3D flash lidar, where the backscattering from hard targets is imaged onto a CCD with independently time counting pixels, enabling a three-dimensional image of the scattering objects, has been demonstrated by Stettner et al. (n.d). Gai et al. (1996) reported a range resolution of 2.8 mm when applying picosecond lidar for simulation of clouds by suspending microspheres in a water solution. A lidar instrument for species specific measurement inside power plants, with a range resolution of 40 cm, was described but not demonstrated by Cavalcabo et al. (1993). Heiser and Sedlacek (2006)

developed a lidar system for monitoring of perfluorcarbon tracers to ensure intact protection covers at waste sites

The fundamental principles of remote sensing have been thoroughly described in several textbooks, e.g. (Measures, 1984; Weitkamp, 2005; Fujii and Fukuchi, 2005; Kovalev and Eichinger, 2004), while a comprehensive survey of lidar research, including numerous examples of applications, is given in a review article by Argall and Sica (Argall and Sica, 2002). Lidar techniques used for atmospheric studies are often categorized into groups according to the kind of interaction between the laser light and the atmosphere. Weitkamp (2005) for example uses five groups:

- Elastic-backscatter lidar   • Differential-absorption lidar (DIAL)
- Raman lidar   • (Resonance) fluorescence lidar   • Doppler lidar

Since the advent of lasers, lidar has in principle been based on pulsed lasers. The basic principle of modern lidar is that a laser pulse is emitted towards the remote volume of interest. The backscattered laser light is collected and detected temporally resolved, typically using a telescope arrangement and a PMT. Figure 5.1 depicts the basic lidar principle showing both point detection (one dimensional result) and line detection (two dimensional result).
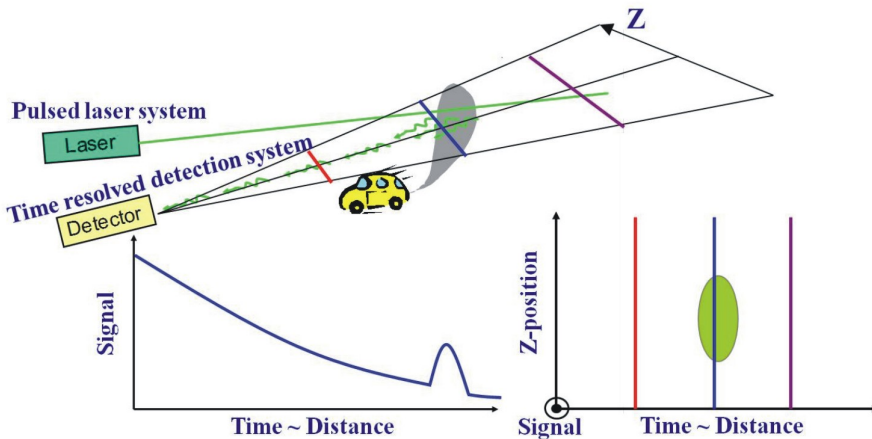

Figure 5.1 *The principle of lidar. Light is directed towards the region of interest. The backscattered light is detected. A time resolved signal is shown to the left, where a peak is seen, which corresponds to the scattering from the exhaust gases from the car. To the right, the result of time resolved imaging of a line is shown, with Z-axis indicated both in the diagram and real world illustration. The exhaust gases distribution is clearly illustrated by the green area.*

The laser light pulse has experienced interaction with matter along its way through the medium, and to understand how the amount of collected light behave as a function of time, all interaction with the laser pulse, finally leading to a fraction of the energy initially contained in the laser pulse being detected, must be understood and described.

The mathematical description of the power detected as a function of distance from the receiver is referred to as the lidar equation. The nomenclature of the lidar equation is different depending on the literature consulted, but the content is the same.

At a given time, t, the detected light is scattered from a distance $R = tc/2$. During the passage back and forth across the distance R, the light intensity has decreased due to interaction with particles and molecules along the path of the laser beam. The decreased transmission, $T_{ext}(R)$, due to extinction, is calculated by an integrated version of the Beer-Lambert law:

$$T_{ext}(R) = e^{-\int_0^R \alpha(\lambda_0, \chi)\mathrm{d}\chi} \; e^{-\int_0^R \alpha(\lambda, \chi)\mathrm{d}\chi} \, , \tag{5.1}$$

where α is the extinction coefficient, λ_0 is the laser wavelength, and λ is the wavelength of the scattered light. The integration is conducted over the laser light path back and forth to distance R.

The extinction coefficient is defined as the sum of the product of the number density, C, and extinction cross section, σ_{ext}, for each kind of interacting matter in the volume:

$$\alpha(\lambda, R) = \sum_i C_i(R)\sigma_{ext,i}(\lambda) \tag{5.2}$$

The probability of scattering per length unit from the distance R, $P_{sca}(\lambda, R)$, is given by the product of the full, i.e. 4π, solid angle, scattering cross section, σ_{sca}, and the number density of scatterers, C.

$$P_{sca}(\lambda, R) = \sum_i C_i(R)\sigma_{sca,i}(\lambda) \tag{5.3}$$

As only the backscattered fraction of photons is of interest, eq. 5.3 is divided with the full solid angle, i.e. 4π, assuming isotropic scattering, giving an expression for the probability of scattering per steradian:

$$P_{sca}^{\Omega}(\lambda, R) = \frac{\sum_i C_i(R)\sigma_{sca,i}(\lambda)}{4\pi} \qquad (5.4)$$

It should be noted that the cross section sometimes is given as a differential scattering cross section, which is already given per steradian, then, of course, eq. 5.3 is used instead.

Knowing, the probability of backscattered photons per steradian, the solid angle in steradians, Ω_c, of the light collecting optics is needed to complete the lidar equation. The definition of solid angle gives:

$$\Omega_c \approx \frac{A_c}{4\pi R^2} \cdot 4\pi = \frac{A_c}{R^2}, \qquad (5.5)$$

where A_c is the area of the collecting optics. Using eqs 5.1, 5.4, and 5.5, given a number of photons sent out from the lidar, N_s, the number of photons, $N_c(R)$, reaching non-obscured collection optics per scattering length unit (cm^{-1}) from distance R may be expressed:

$$N_c(R) = N_s e^{-\int_0^R \alpha(\lambda_0, \chi)d\chi} e^{-\int_0^R \alpha(\lambda, \chi)d\chi} \frac{A_c \sum_i C_i(R)\sigma_{sca,i}(\lambda)}{4\pi R^2} \qquad (5.6)$$

Prediction of the number of photons actually reaching the detector surface, N_d, knowing the number of photons leaving the laser, N_L, requires a system factor, $\eta(\lambda)$, accounting for losses in mirrors and filters used in the lidar setup. If the scattering is an inelastic process, i.e. $\lambda \neq \lambda_0$, η will be the product of two parts, i.e. $\eta(\lambda) \times \eta(\lambda_0)$.

In addition to η, a function, $O(R)$, describing how large fraction of the light scattered from distance R that indeed hits the surface of the detector (Harms, 1979; Halldórsson and Langerholc, 1978), is needed. The factor $O(R)$ is commonly referred to as the geometrical overlap function. It accounts for the effects of obscuration, field of view, and depth of field of the collecting optics. A

more elaborate description of $O(R)$ and its implications in extreme near field lidar ($R < 10$ m) is given in Section 5.2, covering details about picosecond lidar.

To conclude the review of the lidar equation, the collected signal's dependence of the scattering coefficient, given per length unit, must be taken care of. The temporal laser pulse length, τ_L, must be included. It is obvious that light scattered from all parts of a range interval, ΔR, called the effective pulse length, will reach the detector at exactly the same time if the pulse has a finite length, τ_L.

Imagine a photon at the leading edge of the laser pulse scattering backwards at distance $R + \Delta R/2$. The photon will travel a distance, ΔR, corresponding to half the spatial pulse length, $c\tau_L/2$, before it meets a photon from the trailing edge of the pulse.

$$\Delta R = \frac{c\tau_L}{2} \tag{5.7}$$

From this spatial extent, ΔR, centered at R, there will be backscattered photons traveling together reaching the detector at the same time. This fact also implies that eq. 5.7 sets a lower limit for the spatial resolution achievable with a lidar system.

To find the total number of detected photons as a function of temporal laser pulse length, eq. 5.6, given in units (cm^{-1}), needs to be multiplied with the effective pulse length, ΔR. Further Multiplication with the system factor, η, and the overlap function, $O(R)$, as well leads to an expression for the total number of photons, N_T, collected at a time corresponding to scattering from a distance R, as shown in eq. 5.8. For simplicity the assumption of purely elastic scattering has been made, i.e. $\lambda = \lambda_0$.

$$N_T(R,\lambda,\tau_L) = N_L \frac{\eta(\lambda)O(R)A_c \cdot \Delta R}{4\pi R^2} \cdot e^{-2\int_0^R \alpha(\lambda,\chi)\mathrm{d}\chi} \sum_i C_i(R)\sigma_{i,sca}(\lambda) \tag{5.8}$$

5.2   picosecond lidar: general setup and features

A picosecond lidar system for applications in large scale combustion environments features a couple of characteristics that distinguishes it from regular atmospheric lidar systems utilizing nanosecond lasers. The perhaps most notable difference is that the maximum range resolution due to different laser pulse durations, see eq.

5.7, will differ with around three orders of magnitude. Our system enables a maximum range resolution on the mm scale while a nanosecond system generally provides a resolution of around 10 m. Another striking difference is that the overlap function, $O(R)$, will vary significantly with range, due to blurring effects arising from the short depth of field at the short collection distances typically used (a couple of meters).

A general setup of a ps-lidar system can be seen in fig. 5.2. The basic elements are a pulsed laser that provides pulses of picosecond duration, an outcoupling mirror, M1, which directs the laser pulses towards the volume of interest, a light collecting optical element, M2, represented here by a mirror, and a detector providing time resolved signals. The general lidar equation was described in the previous section leaving us in this section to investigate the overlap function in the near field case of lidar.
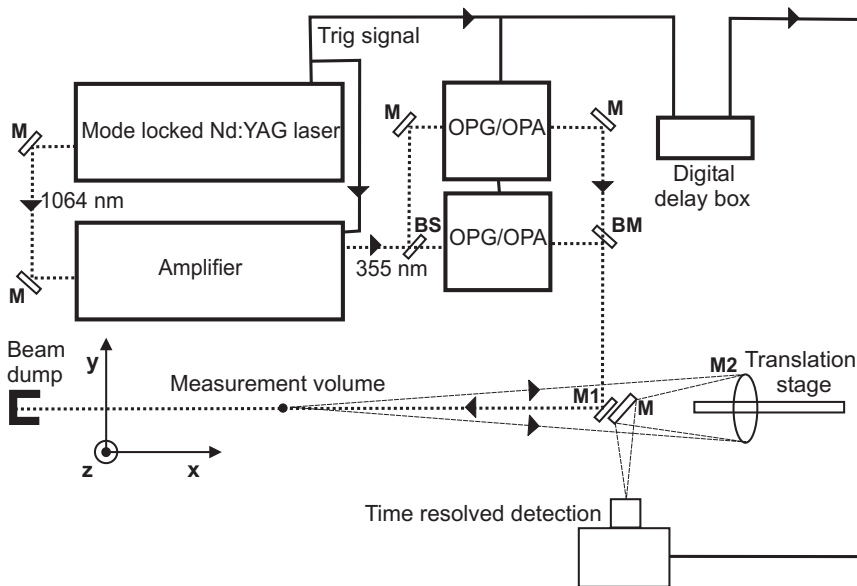

Figure 5.2 *A schematic setup of a ps-lidar system. BS indicates beamsplitter, BM indicates beam merging, M are planar mirrors, M1 is the outcoupling mirror directing laser light out from the telescope along its optical axis, and M2 is a concave mirror for collection of the scattered light from the measurement volume.*

A streak camera provides time resolved imaging of what is imaged onto the slit of the camera, enabling two dimensional imaging of a part of the x-y plane (see fig. 5.2) extending from the detector through the measurement volume. Imagine a

laser pulse being reflected by the outcoupling mirror to interact sequentially with four equally large volumes of highly scattering media, which can be considered as four lines, I-IV, in the measurement volume, see fig. 5.3a.

For simplicity, assume for the moment that the scattered light from each of the volumes is sharply imaged onto the slit of the detector. Schematically, the resulting time resolved image of the slit will look as in fig. 5.3b. The lines situated further away from the detector will appear shorter in the image due to basic geometrical optics effects.

If the depth-of-field effects are added, letting line IV be in the imaging focus, the resulting image will look as in fig. 5.3c, since lines I-III will be blurred. If the fact that the outcoupling mirror acts as an obscuration disc in front of the light collecting optical element, is added, the result will schematically appear as in fig. 5.3d.
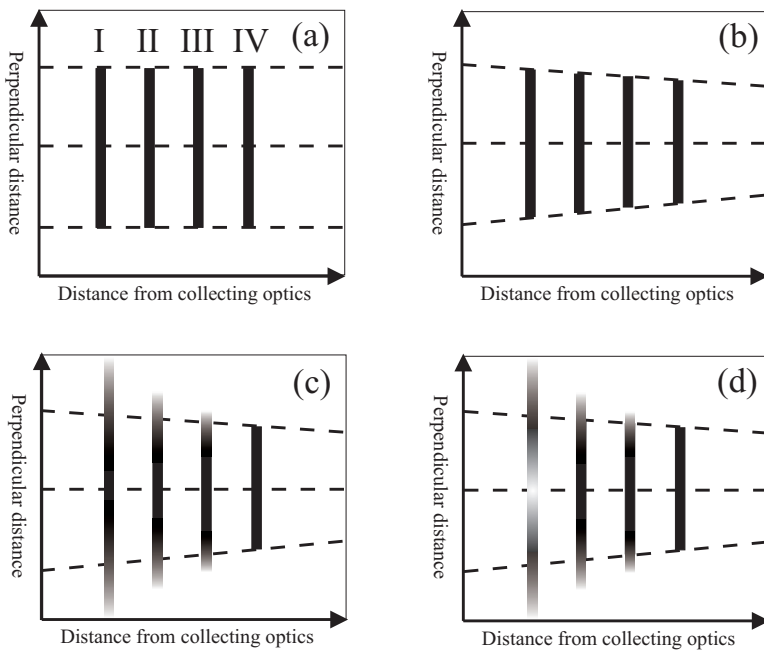

Figure 5.3 *Illustration of two-dimensional lidar detection of four lines, I-IV, in the measurement volume. In (a) the real objects are shown. Panel (b) shows geometric imaging effects, (c) shows depth of field effects, and (d) shows effect of obscurations in the solid angle of the light collecting optics.*

The images of the lines closest to the mirror will have shadowing effects, manifested as blocked central parts of line I, which is schematically visualized in fig. 5.4 as well. In a real experimental image of such scattering lines, the spatial profile of the laser beam, manifested along the vertical axis of the images, will also be reflected in the images.

In fig. 5.4 it is readily seen that when the detector slit is out of imaging focus (the focus position is indicated with *image*) the shadow of the obstructing object will be imaged onto the slit. Ultimately the shadow will become larger than the slit and no light will pass through it.
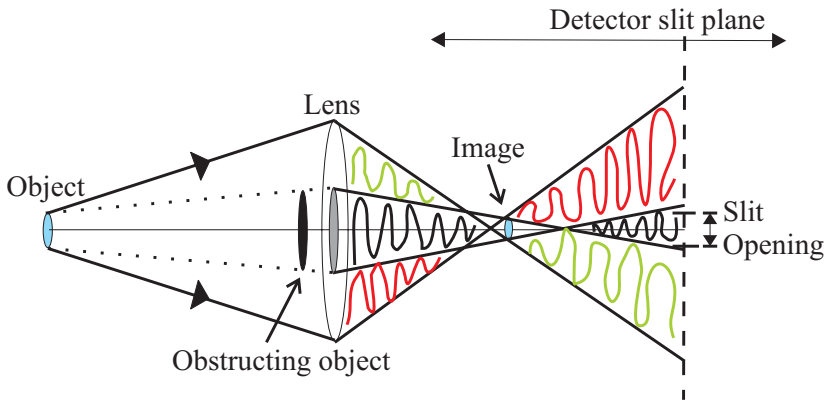

Figure 5.4 *Illustration of how an obstructing object in front of the light collecting optics will produce a shadow image when the detector-slit plane is out of focus, i.e. not coinciding with the image plane.*

Similar processes as visualized in fig. 5.3 are also taking place in the direction of the slit width, i.e. perpendicular to the slit height, see fig. 3.2, which result in an intensity function, $f(R)$ along the horizontal axis in the images. This function will have at its maximum value in focus and decrease in both directions as less of the scattered light is collected through the streak camera slit. A short depth of field will enhance the influence of this function.

The total obtained horizontal intensity function from a volume containing a homogeneously scattering medium will be $f(R)$ multiplied with the $1/R^2$ from the lidar equation (eq. 5.8) and contribution from a potential misalignment of the optical axis and the laser beam. A typical streak camera image of backscattered laser light in pure air featuring a combination of all the aforementioned effects is shown in fig. 5.5.

Misalignments in the direction of the slit width (in the x-z plane) will image different parts of the laser profile (z-direction) onto the slit at different distances, giving one of the discussed range dependent effects on intensity, which are hard to differentiate from each other.
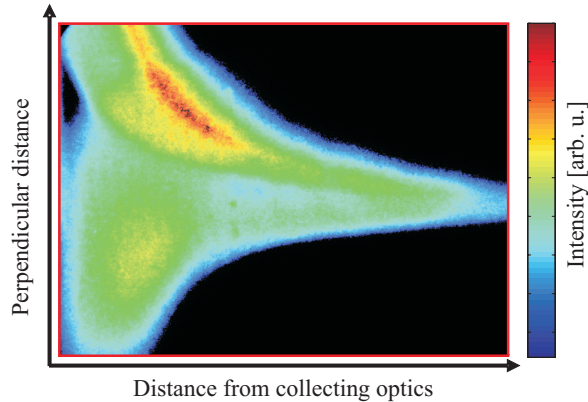

Figure 5.5 *A streak camera image of backscattered laser light in pure air. The image contains the typical near-field lidar features illustrated in figs 5.3 and 5.4.*

Since the slit height is about two orders of magnitude bigger than the slit width, the system is much easier to align in that direction (corresponding to a direction perpendicular to laser light propagation in the real world for the experimental setups used in this work). The simple explanation for this is that misalignments in the direction of the slit height, in a system with centrally overlapping optical axes of the collection system and the laser, are often easily seen in the resulting streak camera image and can thus without difficulty be corrected for. The centerline of the image of the backscattered light will be tilted from a horizontal orientation when the optical axes are misaligned in the x-y plane (see fig. 3.2).

For the same reason, the system is also much more sensitive to alignments in the direction of the slit width, giving maximum intensity when the central maximum part of the laser beam profile is imaged onto the slit and rapidly decaying intensity for minor angular deviations in the outcopling of the laser light.

The streak camera may be replaced by a point detector, for example a PMT connected to an oscilloscope, providing one dimensional measurements, i.e. intensity as a function of time, which is the same type of data that will be achieved

if two-dimensional images, such as those shown in figs 5.3d and 5.5, are integrated along the vertical axis at each time position.

The imaging performance of the ps-lidar system is, as discussed previously, limited by the fact that the depth of field is relatively short at the measurement distances of interest.

It can be shown, using the geometrical optics definition of circles of confusion (Pedrotti and Pedrotti, 1996), that the depth of field, R_d, may be expressed:

$$R_d = \frac{2A_r d_b s(s-f)f^2}{f^4 - A_r^2 d_b^2 (s-f)^2} \ , \qquad (5.9)$$

where A_r is the relative aperture (also called f-number), f is the focal length of the collecting lens or mirror, s is the object distance, and d_b is the maximum allowed diameter of the circles of confusion. The physical meaning of d_b is that it describes how wide the diameter of an image of a point is allowed to be when the point is out-of-focus.

The f-number is defined as f / d_c, where d_c is the effective diameter of the collecting optics. The effective diameter of the input optics on a regular camera is usually controlled with a diaphragm, i.e. an adjustable aperture. It is for photographers well known that a smaller aperture results in less light onto the camera but a larger depth of field, which usually has to be compensated for by increasing the exposure time.

The depth of field versus object distance is plotted for four different values of d_b in fig. 5.6., with the f-number set to 4.5 and the focal length set to 0.45 m (given by our system). The d_b value 0.014 mm, corresponds to the pixel size of the CCD on the streak camera, the next value, 0.025 mm, is a standard value used for 16 mm motion picture, and the last two values are chosen just for comparison.

It can be seen in fig 5.6 that for short object distances, $s < 5$ m, and reasonable d_b values for imaging, i.e. between 0.025 and 0.1 mm, which of course depends on the purpose of the imaging, the depth of field varies between a couple of millimeters and a decimeter ($d_b = 0.1$ mm will give 144 effective image points along the vertical axis of the streak camera, since the CCD chip is 14.4 mm). Of course, this fact limits the possibility to make two-dimensional lidar measurements over long ranges at these distances.

At 5 m the demagnification will be around 10, which makes an imaging resolution of 1 mm over a 1-dm range, or an imaging resolution of 1 cm over a 1-m range, possible. Considering a four times greater distance, i.e. 20 m, it is

possible to achieve 1-mm image resolution over a 4-dm range, but then on the other hand the long distance reduces the collected light by a factor 1/16 in
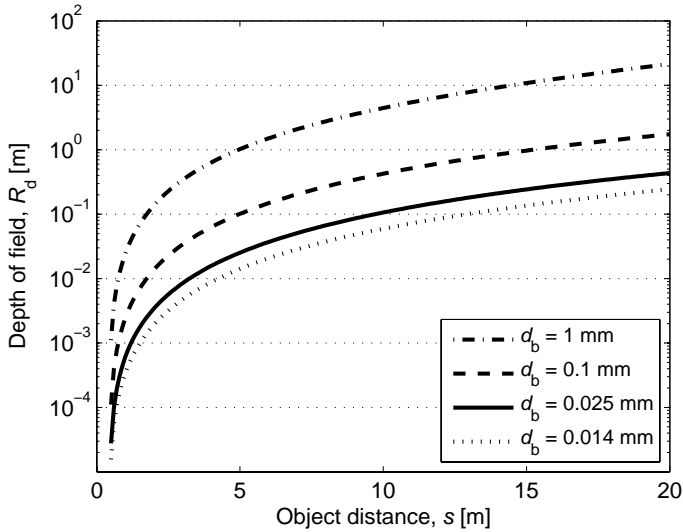

Figure 5.6 *Depth of field versus distance to the object where the focus is set. The results of four different sizes for the allowed diameter of the circle of confusions, indicated in the legend, are illustrated for comparison purposes.*

comparison with the light collected at 5-m distance (due to the $1/R^2$ dependence of the lidar equation, i.e. eq. 5.8).

Hence, it is a trade-off between collected light and depth of field, which will also be the case if the effective diameter, d_c, is decreased to increase the depth of field, since the exposure time in a lidar experiment is intrinsically set by the laser pulse duration.

However, there are two ways to compensate for the light loss obtained when increasing the depth of field: Increase laser pulse energy and/or average over more laser shots. It is also interesting to note that the diffraction limit, i.e. $d_d = s \times \Delta\theta = s \times 1.22\lambda / d_c$, set by a 1-dm mirror at the wavelength 532 nm, is 0.03 and 0.13 mm, at 5.0 and 20.0 m, respectively. In practice, the resolution is limited by aberration effects, e.g. spherical aberrations and coma.

The fully open slit height of the streak camera is ~1.5 cm. Hence the full vertical height of a streak camera image, see fig. 5.5, corresponds to ~8, 13, and 28 cm, at the distances 3, 5, and 10 m from the collecting optics, respectively. It is possible to increase the field of view by choosing collecting optics with shorter

focal distance, but geometric optics indicates that increasing the field of view a factor k decreases the collected light with a factor $\sim 1/k$.

5.3 Experimental design considerations

The choice of mirror or lens for collection of scattered light is in many cases, particularly in preliminary tests, limited to what is momentarily available in the laboratory. For initial tests, lenses might be a bit more intuitive regarding light collecting geometries, and are usually available in a laser laboratory as well. Geometrical optics sketches of the expected outcome, or the result obtained, of a lidar experiment may also be less complex using a lens.

The $1/R^2$ dependence of the collected lidar signal makes it very important from a signal point of view to have a large-diameter collection optic, although a large diameter decreases the depth of field as discussed in the previous section. A mirror is probably the most common choice of large-diameter optic, since lenses with diameters larger than 10 cm are rare as they become expensive and heavy. If the project budget is ample, it could be beneficial though to select a lens based system, since lens combinations, such as achromatic doublets, can be designed to give a minimum of spherical aberrations while reducing the chromatic aberrations as well.

In fact, a 10-cm diameter plano-convex quartz lens with a focal length of 15 cm was used in the first lidar experiments performed within the present project. In order to maximize the amount of collected light, a telescope matching the relative aperture of the 10-cm diameter lens (f/1.5) and the streak camera (f/4) or spectrometer (f/5) was used. The small relative aperture of the 10-cm diameter lens induces spherical aberrations, which, obviously, are not desirable in imaging studies. The spherical aberrations also limit the signal strength when the lens is used together with a streak camera, due to the blurry light collection onto the narrow streak camera slit.

A drawback with single lenses, not possessed by mirrors, is chromatic aberrations, which have a negative impact on experiments based on polychromatic signals, e.g. laser-induced fluorescence, or scattering at two different wavelengths.

Another type of lens, with impaired imaging ability, which might be of interest due to its excellent light collection efficiency, is the Fresnel lens. Relatively inexpensive plastic Fresnel lenses are available with large diameters. Unfortunately, they do not transmit radiation in the ultraviolet region and, for larger diameters,

time dispersion may also be an issue in studies requiring very high temporal resolution. A 1-m diameter Fresnel lens with focal length 1 m has a time dispersion corresponding to 7 cm range resolution in a lidar measurement. In, for example, experiments based on 532-nm laser radiation and a PMT as detector, a Fresnel lens would probably work perfectly well, yielding a range resolution set by the difference in distance travelled for light passing the center and the outer part of the lens, or by the corresponding range resolution, ~15 cm, set by a state-of-the-art PMT.

A spherical mirror may be regarded as part of a larger spherical mirror, see fig. 5.7. In measurement situations with extremely low collected signals, this fact can be used to improve the signal collection efficiency. In position A, the entire mirror area is used when light is collected from the sources X, O, and I, while in position B, only fractions of the mirror area is used, due to the obscuration by the outcoupling mirror. Using the mirror in position A corresponds to off-axis imaging, which introduces optical errors, e.g. coma and astigmatism, in the images.

The streak camera image schematically shown in fig. 5.7 demonstrates the effect of combining objects getting out of focus and off-axis imaging. The objects X, O, and I, indicated in blue, red, and black, respectively, are imaged at positions indicated in the figure.
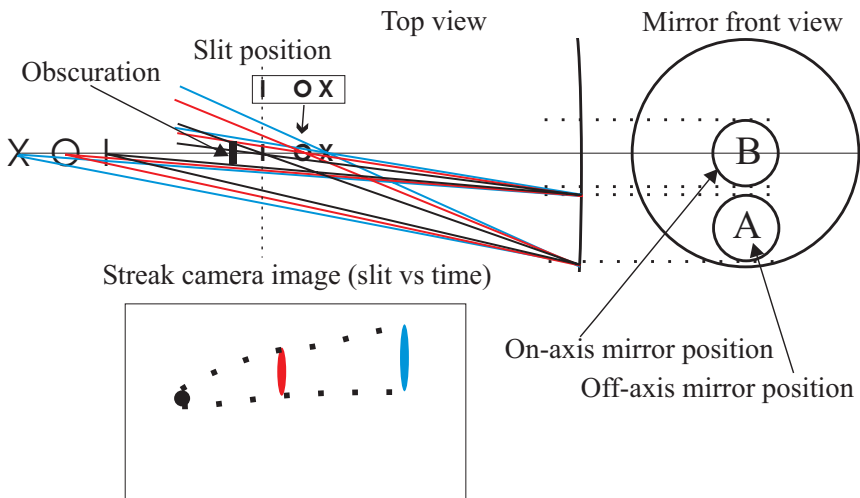

Figure 5.7 *Illustration of two light collecting mirrors at positions A and B can be considered as parts of a larger mirror and the effects of using the off-axis position, B, on a resulting streak camera image.*

It may be useful to compare with fig. 5.4, where on-axis imaging is visualized. Since imaging using a mirror in position A is regarded as imaging with a minor portion of a much larger mirror, as indicated in fig. 5.7, the depth of field in the horizontal direction will be short, corresponding to half the size of the large mirror.

Due to the difference in vertical- and horizontal distance to the optical axis, it is reasonable to believe that the depth of field in the vertical direction will be unaltered compared with mirror position B (the vertical direction is the direction of the narrow slit width). Hence, mirror position A may in many measurement situations be a proper solution for improved signal intensity in one-dimensional measurements.

For the choice whether to use a streak camera or a PMT, three parameters are of importance:

- The desired range resolution
- One- or two-dimensional imaging
- The amount of scattered light

The range resolution achievable with a streak camera is sub-cm, while a PMT in combination with a fast oscilloscope provide a range resolution of >10 cm. A streak camera enables two-dimensional imaging, allowing both radar-like two dimensional images and spectrally resolved images of a line, while a PMT is restricted to one-dimensional imaging. If a streak camera is used together with a spectrograph the temporal dispersion of the spectrograph, depending on the order of the grating, wavelength, and number of grooves illuminated, should be considered (Visco et al., 2008).

The major profit using a PMT is its higher sensitivity in combination with the larger area of the aperture (mm size) in comparison with the streak camera slit (100 µm) which of course is a very attractive feature, for instance in experiments with low-energy laser pulses (~<100 µJ) or for detection at longer distances, where the $1/R^2$ dependence of the received signal intensity is a significant issue. A PMT-based system is also to some extent less sensitive to misalignments, since the PMT aperture is much larger than the streak camera slit.

5.4   Range resolution of the ps-lidar system

To verify that the range resolution of the lidar system is linearly dependent on the streak rate of the streak camera and ultimately limited by the laser pulse duration, an experiment with two metall wires (~1-mm diameter) was carried out. The two thin metal wires were positioned along the laser beam, one of them translatable along the beam. The scattered light was collected with a 10-cm lens at a distance of 4.5 m from the wires. For each streak rate the wires were moved closer in steps of 0.5 mm, with three single- shot images recorded at each distances.

Figure 5.8a shows a streak camera image from a measurement using a streak rate of 25 ps/mm with the wires positioned 7.5 mm apart. A curve obtained by vertically integrating in the image is also shown in the figure (red curve).
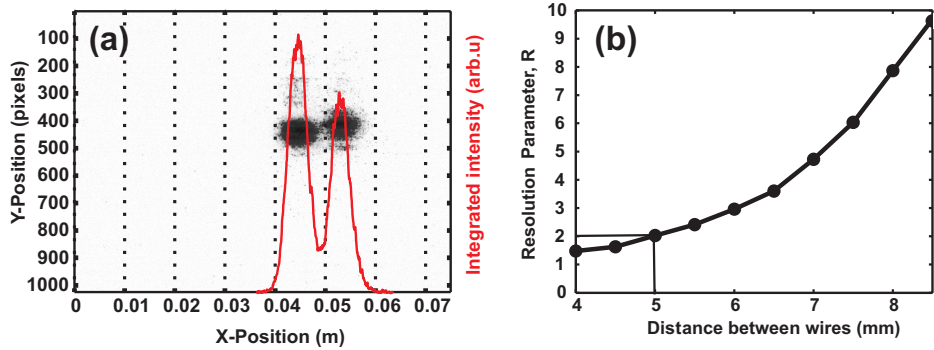

Figure 5.8 *Results of range resolution measurements. Panel (a) shows a streak camera image of two metall wires positioned 4.5 m away from the light-collecting optics. Vertically integrated signal is overlaid in red. In (b), the obtained resolution parameter, R, for different distances between the wires is shown.*

A resolution parameter, *R*, was defined as the average peak value of the signals from the two wires divided with the minimum intensity between them. The limit of a resolved object was defined to be $R \geq 2$, which can be considered as a fairly strict resolution limit compared with other resolution criterions. For example, the Rayleigh criterion is defined as the distance between two point sources when the first diffraction minimum of one point coincides with the maximum of the other point, which corresponds to a dip between the peaks of ~20% (Pedrotti and Pedrotti, 1996).

In fig 5.8b, R is plotted versus distance between the wires for a streak rate of 25 ps/mm. It is indicated where the two peaks are considered to be resolved, i.e. the resolution parameter ≥ 2, which is 5 mm for this streak rate. The resolution limit measured for each streak rate is shown in fig. 5.9.

Note that the fastest streak rate is the lowest number, 10 ps/mm, on the x-scale. The streak rate is defined as the time it takes during the streak to move the resulting signal 1 mm on the CCD. Hence a higher number corresponds to a slower streak and, consequently, a worse lidar range resolution.

It is seen that the range resolution is linearly dependent on the streak rate. Except for the two fastest streak rates, where the range resolution is observed to be almost constant, which is explained by the fact that the laser pulse duration, Δt, here limits the ultimate range resolution to ~$c\Delta t/2$ = 0.45 cm. The highest achieved range resolution in the measurements, using the streak rate 10 ps/mm, was 0.46 cm, which is in excellent agreement with the expected limit.
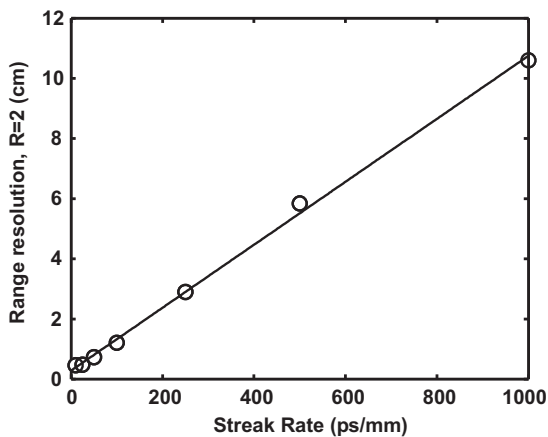

Figure 5.9 *The range resolution, employing 30 ps laser pulses, for all available streak rates of the streak camera.*

To give an idea about the spatial resolution along the vertical axis in the image, which is highly dependent on the collection optics, it can be mentioned that the total vertical axis in fig 5.8a is ~10 cm and the wire diameter, as mentioned previously, is ~1 mm in diameter. The dots in the image rather corresponds to ~0.5-1 cm (vertically), which indicates that the collection optics used in this experiment, consisting of the 10-cm mirror and telescope mentioned in Section 5.3, have a low imaging resolution.

5.4.1 Utilizing the measured range resolution

With the range resolution of the system determined, the question is: what is the correct interpretation of this resolution? As discussed in the previous section, the resolution criterion used in this work differs from the more commonly applied Rayleigh criterion, but, on the other hand, whether or not objects can be considered resolved strongly depends on the volume surrounding the objects. For example, if scattering off two identical objects are considered, the two objects can, in most cases, easily be resolved even if the signal recorded between the peaks only drops 10%, but if the signal is generally very low, or the objects are yielding signals differing much in intensity, it may be very difficult to discern the objects even if the resolution criterion stated in the previous section is used.

Generally speaking, objects separated with at least the range resolution defined in the previous section will be easily discerned. However, that does not say anything about how a value measured for a certain point is expected to be diluted by the values in the surrounding points. Such estimations are achieved by convolving a measured temporal response function (TRF) of the detection system with the real undiluted signal. If the TRF is not available it can be estimated using a plausible shape of the function, for example Gaussian, having the boundary condition of being at 25% of its maximum value at the width equal to the resolution measured in this work.

For example, employing a streak rate of 500 ps/mm gives a range resolution of 6 cm according to fig. 5.9. The TRF at this streak rate can then be estimated by a Gaussian function being 6 cm wide at 25% of its maximum value. Alternatively, to simplify the subsequent convolution, the TRF can be approximated with a triangular function having the two sides decreasing to 25% of the peak value in 3 cm on each side. The important facts are that when the centers of the TRFs are 6 cm apart, the dip between them will have a value that is 50% of the individual peak values and that the area of the TRF is normalized to unity.

In figure 5.10 it is illustrated how such a TRF may be used to estimate the outcome of a lidar experiment. A non-normalized triangular TRF is shown to the left and a signal from a hat shaped "real" scattering object is shown to the right having the TRF overlaid. Since both the object and the TRF are symmetric it is sufficient to treat the left part of the object in this demonstration. If the aim is to find out how diluted the center point of the object will be in the resulting signal, the solution is in this case to do a manual convolution of the TRF and the object shape. One way of doing the manual convolution is to first position the TRF with its peak at the same position where the step in scattering is situated, as illustrated

in the right part of the figure. It is seen that this particular position will contribute with roughly half of its value to the center point of the resulting object signal, S_{meas}. The convolution can at this stage be divided in two parts: triangle moving left from this position and triangle moving right from this position (for symmetry reasons only the right half of the triangle is considered). When the triangle is moved to the left all TRF values from half to zero multiplied with the actual scattering S/2 will contribute to S_{meas} and when the triangle is moved to the right all TRF values from half to one multiplied with scattering S will contribute to S_{meas}.

After normalizing the area of the TRF by defining the length of the triangle base to 4 in the calculations (since only half of the triangle is used, half of the area should be equal to unity), the result is $S_{meas} = 0.25 \times S/2 + 0.75 \times S = 7/8\ S$. This information is very useful; if the signal for example would correspond to species concentration, it should be expected that the maximum concentration obtained in the center of the object would only correspond to 7/8 of the real concentration.

Note the following pitfall. The fact that the extent of the high signal part of the object is ~4 cm and the resolution is 6 cm, should not be used in the simpler but erroneous conclusion that the expected result consists of 2 cm / 6 cm = 33% contribution from "outside" the high signal part and 4 cm / 6 cm = 67% contribution from "inside" the high signal part, i.e. $S_{meas} = 1/3 \times S/2 + 2/3 \times S = 5/6\ S$.
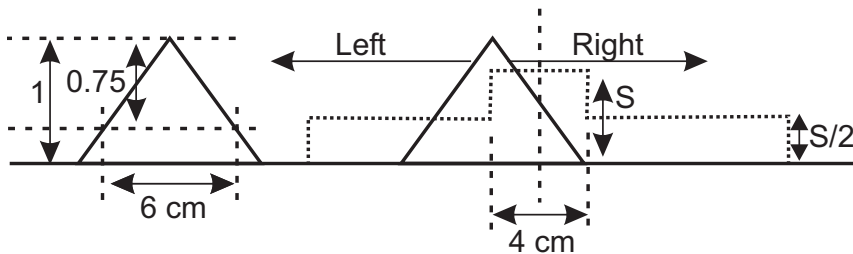

Figure 5.10 *An illustration of how the measured range resolution can be utilized when estimating its impact on measurement results.*

Chapter 6

Picosecond differential absorption lidar (ps-DIAL)

6.1 DIAL

Differential absorption lidar is a measurement concept capable of delivering quantitative species concentrations. The real strength of the method is based on the fact that several unknown parameters in the lidar equation, i.e. eq. 5.8, cancel out. By recording two lidar curves, $N_{T,\lambda\text{on}}$ and $N_{T,\lambda\text{off}}$, using two different wavelengths, referred to as λ_{on} (strong absorption) and λ_{off} (weak absorption), possessing different absorption cross section for the molecule of interest, and forming a ratio, several wavelength-independent system constants cancel out.

$$\frac{N_T(R,\lambda_{on},\tau_L)}{N_T(R,\lambda_{off},\tau_L)} = \frac{N_{L,\lambda_{on}}\eta(\lambda_{on})O(R,\lambda_{on})}{N_{L,\lambda_{off}}\eta(\lambda_{off})O(R,\lambda_{off})}$$

$$\times \frac{e^{-2\int_0^R \alpha(\lambda_{on},\chi)\mathrm{d}\chi}}{e^{-2\int_0^R \alpha(\lambda_{off},\chi)\mathrm{d}\chi}} \frac{\sum_i C_i(R)\sigma_{i,sca}(\lambda_{on})}{\sum_i C_i(R)\sigma_{i,sca}(\lambda_{off})} \qquad (6.1)$$

At this moment, approaching a simplification of eq. 6.1, there is one particular matter to be careful about, which is not always obvious in the lidar

literature. If the ratio of the geometrical overlap functions, $O(R,\lambda)$, of the two wavelengths is constant as a function of range, R, it will cancel out. In picosecond lidar, however, it has been found that it is very difficult to achieve the same $O(R,\lambda)$ if two different lasers are used or if any kind of realignment of optical components must be made when changing wavelength.

Particularly, in streak camera setups, where backscattered light is collected onto a narrow slit, the system becomes very sensitive to parameters such as beam-direction, divergence, and profile, which indeed makes alignment delicate. If the ratio $O(R,\lambda_{on})/O(R,\lambda_{off})$ is range dependent, a calibration measurement with known number density, preferably zero, of the absorbing molecule, is needed to determine this ratio.

For now let us assume that the ratio $O(R,\lambda_{on})/O(R,\lambda_{off})$ is constant and lump it together with $N_{L,\lambda} \times \eta(\lambda)$, forming the constant K_λ. The extinction coefficient, $\alpha(\lambda,R)$, is divided into two parts; $\alpha_r(\lambda,R) + \sigma(\lambda)N_D(R)$, where $\sigma(\lambda)$ and $N_D(R)$ is the cross section and number density, respectively, of the molecule of interest and $\alpha_r(\lambda,R)$ is the extinction coefficient representing any other extinction. Designating the sum of scattering coefficients β, the expression given in eq. 6.1 may now be simplified into:

$$\frac{N_T\left(R,\lambda_{on},\tau_L\right)}{N_T\left(R,\lambda_{off},\tau_L\right)} = \frac{K_{\lambda_{on}}}{K_{\lambda_{off}}} \cdot \frac{e^{-2\int_0^R \left(\alpha_r(\lambda_{on},\chi)-\alpha_r\left(\lambda_{off},\chi\right)\right)d\chi}}{e^{-2\int_0^R \left(\sigma\left(\lambda_{off}\right)N_D(R)-\sigma(\lambda_{on})N_D(R)\right)d\chi}} \frac{\beta_{\lambda_{on}}(R)}{\beta_{\lambda_{off}}(R)} \qquad (6.2)$$

From this equation it is pretty straight forward to extract an expression for N_D. In a first step, using $\Delta\sigma = \sigma_{\lambda on}-\sigma_{\lambda off}$, the following rearrangement is done:

$$\frac{1}{2\Delta\sigma}\left(\frac{d}{dR}\ln\left(\frac{N_T\left(R,\lambda_{on},\tau_L\right)}{N_T\left(R,\lambda_{off},\tau_L\right)}\right)+\overbrace{\frac{d}{dR}\ln\left(\frac{K_{\lambda_{off}}}{K_{\lambda_{on}}}\right)}^{0}+\frac{d}{dR}\ln\left(\frac{\beta_{\lambda_{off}}(R)}{\beta_{\lambda_{on}}(R)}\right)\right)$$

$$= \frac{\alpha_r\left(\lambda_{off},\chi\right)-\alpha_r\left(\lambda_{on},\chi\right)}{\Delta\sigma} - N_D(R) \qquad (6.3)$$

and then further rearrangement of the terms leads to

$$N_D(R) = \frac{1}{2\Delta\sigma} \left(\overbrace{\frac{\mathrm{d}}{\mathrm{d}R} \ln\left(\frac{N_T(R,\lambda_{off},\tau_L)}{N_T(R,\lambda_{on},\tau_L)} \right)}^{I} - \overbrace{\frac{\mathrm{d}}{\mathrm{d}R} \ln\left(\frac{\beta_{\lambda_{off}}(R)}{\beta_{\lambda_{on}}(R)} \right)}^{II} \right)$$

$$- \frac{\overbrace{(\alpha_r(\lambda_{off},R) - \alpha_r(\lambda_{on},R))}^{III}}{\Delta\sigma},$$

(6.4)

which is normally referred to as the DIAL equation. As previously mentioned; if the ratio $O(R,\lambda_{on})/O(R,\lambda_{off})$ has a range dependence, which has not been accounted for, a factor $O(R,\lambda_{off})/O(R,\lambda_{on})$ must be multiplied with the backscattering coefficients, β, inside the brackets enclosing the logarithmic factor in term II.

If the ratio of the scattering coefficients can be assumed to have no R dependence, term II can be removed. Normally, an R dependence in this term may be introduced if the concentration of Mie scattering particles varies with R, since Rayleigh scattering and Mie scattering have different wavelength dependencies. This may occur often in combustion situation and is therefore a major source of concern.

Term III can often be neglected if no molecules have interfering absorption lines at the applied wavelengths, which can be exemplified by estimating the impact of term III for NH_3 DIAL.

The contribution of term III can be calculated using the difference in extinction, based on differential scattering cross section. Employing scattering cross section for air at the wavelengths 210 and 220 nm, taken from Miles et al. (2001), yields $\Delta\sigma_{ext} = 5.67 \times 10^{-26}$ cm^2. The concentration, $C = 2.5 \times 10^{19}$ cm^{-3}, is given by room temperature and atmospheric pressure, and the differential absorption cross section of NH_3, $\Delta\alpha_r = 3.0 \times 10^{-18}$ cm^2 is taken from Paper III, where the wavelengths 212.2 and 214.5 nm were used. The resulting impact on evaluated number density becomes 5×10^{11} cm^{-3}, which corresponds to 0.02 ppm.

6.2   Picosecond DIAL applications

In principle DIAL can be used to measure any species that possesses large enough difference in absorption cross section for two wavelengths not too far separated. As long as the differences in the prevailing conditions are small enough for the two wavelengths, as discussed in Section 6.1, it is possible to use eq. 6.4 with only term *I*. In such cases, the only information needed to extract number density is the difference in absorption cross section.

For ps-DIAL, having resolution on the centimeter scale, it is apparent that the absorption measured on that scale will be significantly smaller than the absorption measured with traditional ns-DIAL, having much lower range resolution, i.e. longer absorption path length. Comparing ps-DIAL with atmospheric DIAL, where the resolution may be 100-1000 m, the difference in terms of fractional absorption measured is striking.

The difference is most clearly illuminated by a numerical example using typical atmospheric DIAL parameter values:

- Differential absorption cross section, $\sigma = 10^{-18}$ cm^2
- Range resolution, $\Delta l = 50$ m
- Detection limit, $N_{lim} = 1$ ppm $= 2.5 \times 10^{13}$ cm^{-3}
  (at normal temperature and pressure)

This set of parameters give a single-pass Beer-Lambertian transmission, $e^{-N\sigma l}$, of 0.882, i.e. 11.8% absorption. Changing the range resolution to a value typical for ps-DIAL, i.e. 5 cm, results in a corresponding transmission of 0.99998, i.e. an absorption of merely 2×10^{-5}, which seems unreasonable to be detectable with the signal to noise ratio normally achieved. To achieve the same absorption as in the atmospheric DIAL example the detection limit must be increased to 1000 ppm in the ps-DIAL case, since a decrease of range resolution a factor of 1000 must be compensated by increasing the detection limit or cross section a factor of 1000.

However, a fair comparison between atmospheric DIAL and ps-DIAL requires a discussion about the signal to noise ratio, since that is the parameter, apart from the differential absorption, that determines the detection limit.

Studying eq. 5.8 it is seen that the parameters influencing the signal strength and differ in the two DIAL cases, assuming that the same wavelengths are used, are:

- Number of photons leaving the laser each pulse, N_L, which is proportional to the laser pulse energy, E_L
- Telescope area, A_c
- Distance as $1/R^2$
- Range resolution, ΔR, which affects the effective backscattering volume at each point in time.

Typical values of these parameters for atmospheric DIAL and ps-DIAL in the present work using an OPG/OPA system are:

<u>Atmospheric DIAL</u>: E_L = 400 mJ A_c = 40 cm R = 1000 m ΔR = 1.5 m.
<u>Picosecond DIAL</u>: E_L = 300 µJ A_c = 10 cm R = 4 m ΔR = 1.5 cm

The ratio of the expected signals for the two systems then becomes S_{ps}/S_{atm} = 0.12. In addition, the lidar signals in atmospheric DIAL are often averaged over 100 m or more, which enhances the signal, S_{atm}, even more. Furthermore, in ps-DIAL setups utilizing a streak camera for optimum range resolution, the slit in front of the objective is very narrow, on the order of 100 µm, which blocks a great part of the collected light and reduces the signal, as discussed in Section 5.2. By using an MCP-PMT the signal reduction due to a slit is minimized, but on the other hand the range resolution decreases to approximately 15 cm, limited by the time resolution of the detector.

In practice, it might be a challenging task to establish well-defined measurement objects, which can be used to validate the measurement technique. It is in many cases difficult to create volumes with known number density of the sample species without using any type of cell. Unfortunately standard cells of normal sizes are difficult to use due to the intense scattering from the windows, which even might damage the detector.

However, a fairly long cell, >0.5 m, with windows mounted in Brewster angle to minimize backscattering, might be quite useful, since the window scattering from such a cell may be temporally discriminated from. Another prerequisite, depending on the distance to the cell, is that the entrance window must be large enough not to prevent too much of the scattered light from reaching the collection optics. The measurements presented in this chapter have all been conducted in cells that were open in both ends, or in free flows issued from various nozzles.

Another practical issue may in many cases be how to reach the desired wavelengths with the lasers available. Within the atmospheric lidar community there are many examples of elegant ways to reach a large variety of wavelengths

starting from fixed-wavelength lasers. Using nanosecond lidar, dye lasers, which are tunable, may be attractive to apply. The counterpart in ps-lidar would be distributed feedback dye lasers (DFDL) or any type of source based on optical parametric generation, such as the OPG/OPA system used in some experiments presented in this thesis.

Before a tunable laser source was available for the current work, DIAL was initially tested on a molecule exhibiting a broad absorption structure, namely acetone. This molecule has absorption features allowing a substantial differential absorption cross section using two fixed wavelengths of an Nd:YAG laser, i.e. λ_{on} = 266 nm and λ_{off} = 532 nm. With a tunable laser at hand, experiments have been made on NH_3, KCl, and OH, aiming at determining concentrations quantitatively.

6.2.1 Acetone, $(CH_3)_2CO$

The acetone study (Paper I) was, to the best of our knowledge, the first demonstration of a DIAL experiment providing range resolution on the centimeter scale. One of the objectives was to investigate the potential for mapping fuel distributions based on quantitative measurements of acetone concentrations. Two fixed wavelengths of the Nd:YAG system, 266 and 532 nm, were used as λ_{on} and λ_{off}, respectively, with a differential absorption cross section of 4.36×10^{-20} cm^2 (Thurber, 1999).

Two acetone jets, with 20 mm diameters, created by bubbling air through liquid acetone contained in two flasks, were placed at 340 and 384 cm, respectively. The backscattered signal was collected with an achromatic lens to avoid chromatic aberrations due to the large wavelength difference. A spectrometer was positioned in front of the streak camera in order to spectrally suppress the acetone fluorescence generated upon excitation at λ_{on}, i.e. 266 nm.
In fig. 6.1a the raw lidar curves, based on 200 accumulated single shots, are shown. Due to the dominating effect of the geometrical overlap function in the near field, the shapes of the curves do not follow the characteristic $1/R^2$ behavior. Figure 6.1b shows the ratio between the two curves, where all common features are canceled out, and in fig. 6.1c the number density of acetone, which is proportional to the derivative of the natural logarithm of the ratio, evaluated using only term I of eq. 6.4 is plotted.

The vapor pressure of acetone at the prevailing conditions (Ohe, n.d) corresponds to a number density of 6.6×10^{18} cm^{-3}, assuming a saturated flow of

air through the bubbler flasks. The measurement resolution was estimated to 10 cm using the resolution parameter criterion $R=2$, see Section 5.4.
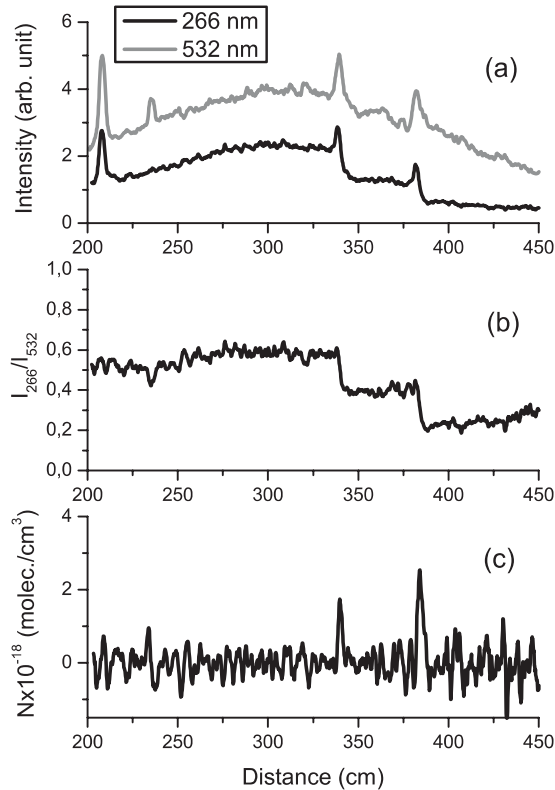

Figure 6.1 *Acetone DIAL results. Panel (a) shows lidar curves for λ_{on}(266 nm) and λ_{off}(532 nm), respectively. Two acetone sources are positioned at 340 and 384 cm, respectively. Panel (b) shows the ratio of the two curves and in (c) the evaluated number density is shown.*

The measured number density in the central part of a jet, probably a bit over 2 cm wide, could by a rough estimate based on the definition of the resolution criterion be expected to be underestimated with a factor 3 (Note that the estimation cannot be made only using the ratio between the resolution and the measurement range, which would imply an underestimate of a factor 5, cf. Section 5.4.1). With this in mind the result agrees well with the expected number density, but in retrospect, it would have been interesting to see the result achieved with a better range resolution.

The large wavelength difference may appear problematic, but for term *II* in eq. 6.4 it actually does not matter as long as the ratio of the scattering coefficients is independent of range. Unfortunately the ratio of the scattering cross sections exhibits different wavelength dependence for different molecules (Sutton and Driscoll, 2004), which may be difficult to account for. Let us presume that pure air is replaced by a 10% ammonia mixture over a distance of 1 cm when the laser pulse is passing in to one of the jets. Further, as a coarse simplification it is assumed that the cross sections of CH_4 and ammonia have the same wavelength dependence. Then it is found that term *II* in the DIAL equation contributes with a false ammonia number density of 1.4×10^{17} cm^{-3}, which is about 20% of the noise level in the evaluated data, and can therefore be neglected.

Moreover, term *III,* i.e. the difference in scattering cross sections, contributing to the differential extinction for the two wavelengths, will also cause a false contribution to the evaluated number density. The differential scattering cross section for air between 266 and 532 nm is 1.0×10^{-25} cm^2 (Miles et al., 2001), and the number density of air (90% concentration) is 1.9×10^{19} cm^{-3}, yielding a contribution to number density from term *III* of 4.4×10^{13} cm^{-3}, corresponding to 2 ppm, which is negligible in this context.

The noise floor seen in fig. 6.1c indicates that the detection limit with this particular experimental setup is around 1×10^{18} cm^{-3}. Decisive factors that limit the signal-to-noise ratio in these experiments are: a rather small collection lens (5-cm diameter) together with an obstructing outcoupling prism, and the combination of two perpendicularly oriented narrow slits (streak camera and spectrometer), which merely transmits a tiny share of the collected light.

Replacing the spectrometer with a suitable filter could probably increase the signal at least a factor of 10. Replacing the 5-cm lens with a 10-cm mirror, which in fact also was done for most of the other lidar experiments presented in this thesis, would increase the signal at least a factor of 4. Finally, if the streak camera is replaced with an MCP-PMT, the signal would probably increase at least another factor of 10, but at the expense of a decrease in range resolution to around 15 cm.

6.2.2 Ammonia, NH₃

The ammonia experiment (Paper III) was the first demonstration of decimeter-resolved ps-DIAL using two tunable laser sources, tuned on and off an absorption peak. Radiation at two wavelengths, 212.2 and 214.5 nm, were produced by the two OPG/OPA systems and used as λ_{on} and λ_{off}, respectively. An MCP-PMT was used as detector, which limited the range resolution to approximately 15 cm.

An absorption spectrum was recorded, yielding the wavelength dependent absorption cross section function valid for the present system. In a detailed study, the differential cross section, $\Delta\sigma_{abs}$, was determined to 3.0 x 10^{-18} cm^2. Moreover, a measurement series based on 1500 accumulated shots, aiming at determining the detection limit, was conducted in a 77-cm long tube into which a well-controlled flow of a CH_4/NH_3 mixture was issued. The detection limit was found to be 40 ppm, with the previously mentioned spatial resolution of 15 cm.

Figure 6.2 shows a photograph of the test tube, with the gas inlet in the center next to the lens holder, used to fixate the tube. In the upper right corner of the picture, parts of the detection and outcoupling optics can be seen.
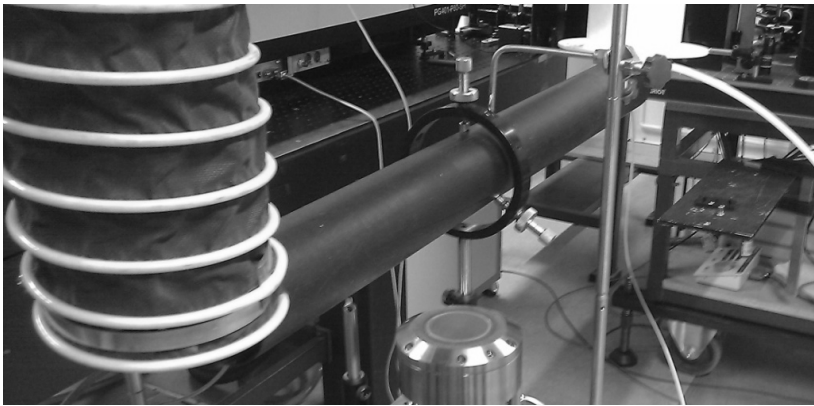

Figure 6.2 *The tube used for NH$_3$ measurements. The gas inlet is in the top center of the tube. The laser beam passes from right to left through the tube.*

Resulting one dimensional DIAL curves, showing number density versus distance, are shown in fig. 6.3. The legend indicates the NH$_3$ number density in the inlet flow. The results were verified by a regular single-pass absorption measurement through the tube at the highest concentration.

The major error sources at modest concentrations ($\sim 5 \times 10^{15}$ cm^{-3}) are probably a systematic error induced by the uncertainty in the differential cross section and the difference in geometric overlap functions for the two laser wavelengths. At low concentrations, close to the detection limit, obviously, the major uncertainty is due to the fact that the absorption is of the same magnitude as the noise on the signal. At high concentrations, a breakdown of the linear absorbance stated in the Beer-Lambert law and a very low signal to noise ratio due to the strong absorption are the major challenges, which in many cases can be

taken care of by choosing a wavelength pair with a lower absorption cross section at λ_{on}.
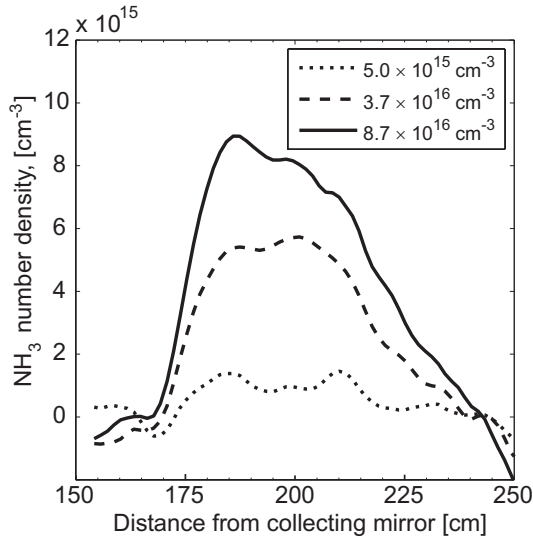
Figure 6.3 *Ammonia number density curves measured through the tube shown in fig. 6.2. The tube openings are situated around 160 and 240 cm, respectively. The NH₃ concentration of the inlet gas flow is indicated in the legend.*
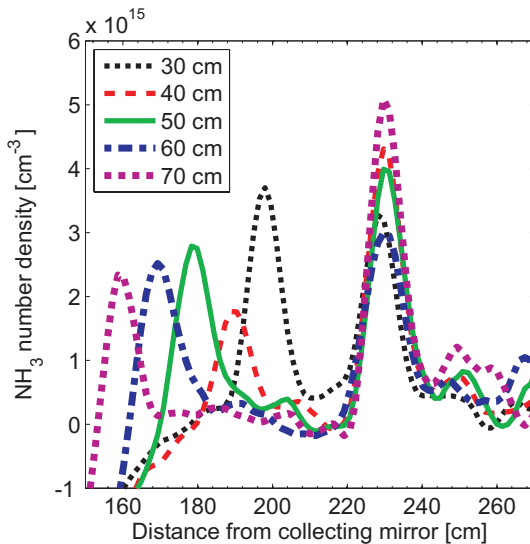
Figure 6.4 *NH₃ concentration curves from measurements with two NH₃ sources positioned with center-to-center distances indicated in the legend.*

To demonstrate the capacity to map NH_3 concentrations from multiple sources, two porous plug burners, having 6-cm diameters and with a gas flow of a 0.5% NH_3 mixture, were used. They were sequentially placed along the laser beam propagation path at 5 different center-to-center distances and the corresponding DIAL curves, based on 1500 accumulations, were recorded. The result is shown in fig. 6.4, where the legend indicates the center-to-center distances. The peaks are equidistantly positioned, 10 cm apart, demonstrating high spatial accuracy as well as the spatial resolution of the ps-DIAL system. No compensation for differences in the geometric overlap function, $O(R)$, was carried out, which is seen as the variation in the concentration baseline.

6.2.3 Vaporized KCl

Measuring vaporized KCl has shown to be challenging due to difficulties with the arrangement of a stable measurement object. The melting point of KCl is 1049 K, and three different methods have been applied in order to reach this temperature. A metal container was constructed to heat KCl using a flame beneath the container, see fig. 6.5a. Unfortunately, due to heat losses in the metal body, the temperature of the salt did not reach more than ~900 K, which is not sufficient for vaporization.
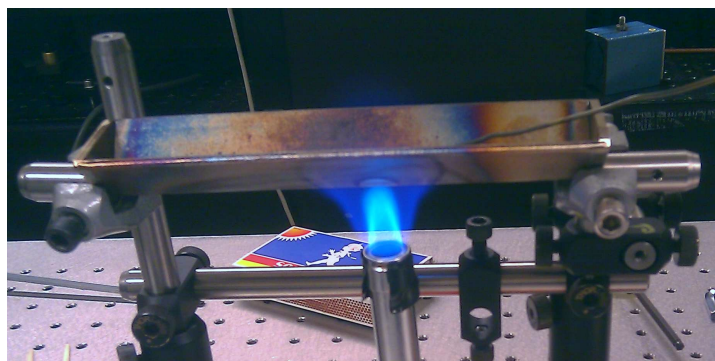

Figure 6.5   *The metal "boat" constructed for vaporizing KCl.*

To improve the heating efficiency, the container was positioned inside a tube furnace, which is shown in fig. 7.6. The tube of the furnace is T-shaped, i.e. there is a smaller perpendicular tube connecting to the part of the tube seen passing through the furnace in fig. 7.6. The container was placed in the smaller perpendicular part of the tube and the temperature achieved was >1050 K, which was high enough to melt and vaporize KCl. It has been reported by

Forsberg et al. (2009) that KCl vapor condensate below ~925 K. Since the temperature in the furnace tube decreases towards the openings (cf. fig 7.8), KCl condensates and a major increase in backscattered light at both ends of the tube is observed due to increased scattering cross section. This enhanced scattering intensity is not an issue in itself in DIAL experiments, but its stochastic nature is troublesome when averaging over many shots.

The signal fluctuations due to random contributions from condensed KCl may to some extent be circumvented by recording every other image from the two DIAL wavelengths, respectively, or by letting two laser pulses propagate quasi-simultaneously, separated by a proper delay, to be able to acquire signals at both wavelengths in one recording.

Figure 6.6a shows resulting number density curves for two test measurement series with KCl in the furnace. The opening of the furnace is positioned between 0.15 and 0.2 m. The wavelengths used as λ_{on} and λ_{off} were 247 and 235 nm, respectively, corresponding to a differential absorption cross section of 1.2×10^{-17} cm^2. A number density of ~5×10^{15} cm^{-3}, which corresponds to 700 ppm at 1050 K, is observed in the DIAL curves. This result lies in the vicinity of the saturated vapor concentration, which was estimated to 550 ppm using the work by Forsberg et al. (2009). In fig. 6.6b, condensed KCl is seen as the faint veils of smoke inside the furnace tube.
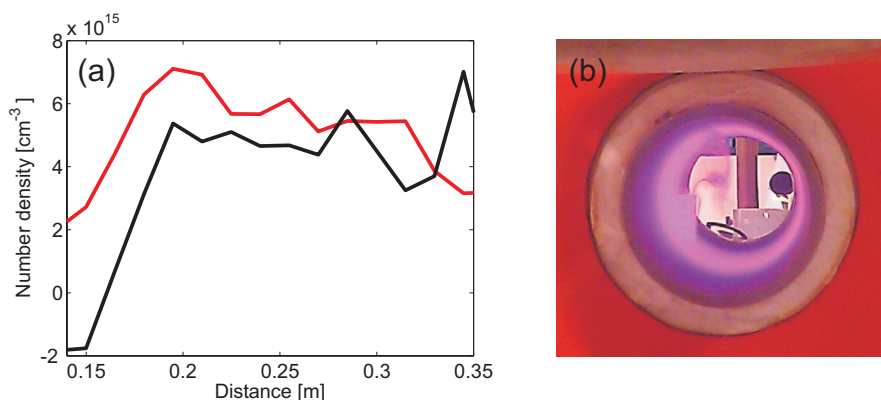

Figure 6.6 *In panel (a) the result of two KCl DIAL measurements are shown. Panel (b) shows the "smoke" inside the furnace tube observed when the saturated KCl vapor cools down.*

A new measurement object was constructed to compare the DIAL measurements with sequential measurements using an "in situ alkali chloride monitor" (IACM). The IACM apparatus, which operating principle is described

by Forsberg et al. (2009), uses a broadband light source (xenon lamp) for line-of-sight absorption measurements, employing differential optical absorption spectroscopy (DOAS). A ceramic tube was constructed to heat single grains of KCl. The tube was coiled with heating wires (Kanthal) and isolated, see fig. 6.7.
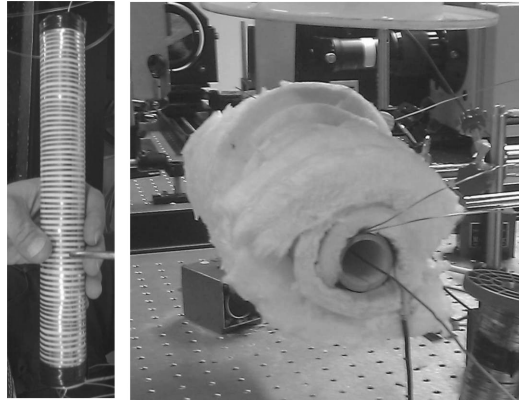

Figure 6.7   *A ceramic tube coiled with heating wires (left) and isolated (right).*

Since the experiments were conducted with a much smaller amount of KCl, in comparison with the furnace experiments, it was expected that the amount of condensed KCl would decrease and facilitate the lidar measurements. It turned out that the efforts to keep the amount of KCl at a minimum did not have any noticeable impact on the condensation. Nevertheless, a set of test measurements was conducted in order to compare the result of ps-DIAL and IACM.

In figure 6.8a, a lidar image recorded with the streak camera, employing the wavelength λ_{on}, is shown, clearly illustrating the intense scattering towards the opening of the tube. The collection mirror was placed off-axis, which leads to the diagonal imaging effect (cf. fig. 5.7). The image is an average over 500 shots. Note that the colorscale is non-linear. The black box indicates the region which has been vertically integrated to yield one-dimensional lidar intensity curves. The intense vertical structure that appears close to horizontal pixel number 200 is due to scattering from a reference object, used to correct for time jitter between laser pulse and laser trigger signal when averaging over several shots.

Figure 6.8b shows the ratio between the lidar curve recorded at λ_{on} and the curve recorded at λ_{off}. For λ_{off}, the measurement was averaged over 250 shots. It is readily observed that the regions containing significant amounts of condensed KCl yield a non valid result. Therefore only signals from the unaffected region between
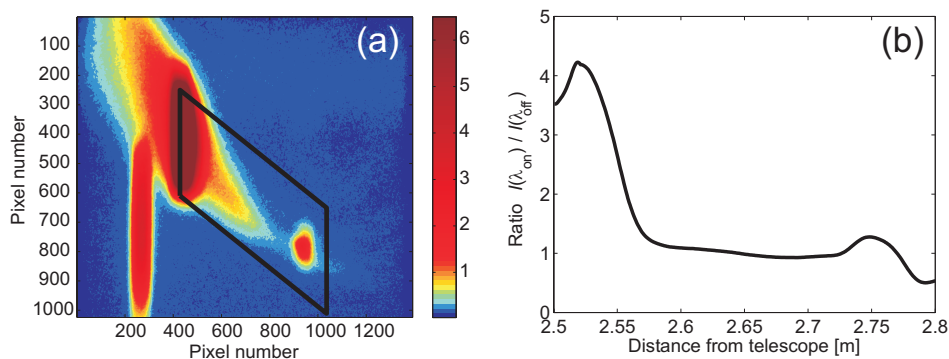
Figure 6.8 *Panel (a) shows a streak camera image recorded with the laser tuned to λ_{on}. The black box indicates the region that vertically integrated yields the lidar curves. In panel (b) the resulting ratio between two such integrated curves is shown.*

2.60 and 2.68 m were used for DIAL evaluation. The resulting concentration curve is shown in fig. 6.9. The concentration curve shows that the number density varies around $\sim 7 \times 10^{14}$ cm^{-3}, which corresponds to 100 ppm at 1050 K. The results obtained by IACM indicate that the expected line-of-sight averaged KCl concentration in the tube was 75-115 ppm.
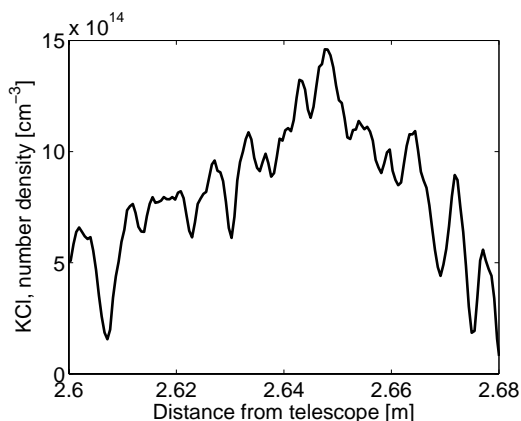

Figure 6.9 *The evaluated KCl number density profile inside the ceramic tube.*

6.2.4 OH in a flame

An experiment with the purpose to investigate the possibility to detect intermediate trace species in a flame using ps-DIAL was carried out in a slot burner (Perkin-Elmer), with $\lambda_{on} = 283$ nm and $\lambda_{off} = 279$ nm. A 281-nm

interference filter (Acton) was positioned in front of the MCP-PMT. The same experimental setup was also used for fluorescence lidar studies, see Section 8.1.1.

The absorption cross section, 2.5×10^{-15} cm^2, for the $Q_1(6)$ OH line near 283 nm, was taken from Versluis et al. (1997). Given the vastly different laser linewidths, i.e. 4 cm^{-1} in the present study versus 0.1 cm^{-1} in the work by Versluis et al. (1997), this cross section is of course a very coarse approximation. Several other transitions, namely $Q_2(1)$, $Q_2(3)$, $Q_{12}(1)$, $Q_{12}(3)$, and $Q_{21}(6)$,will contribute to the effective cross section as well.

Furthermore, since the unfocused laser beam passes along the thin flame, only a small overlap between the laser beam and the zone containing OH is expected, which certainly by itself may decrease the effective cross section one order of magnitude. However, the main object with this experiment was merely to demonstrate whether or not any OH could be observed in the flame using ps-DIAL. Figure 6.5a shows the lidar curves for both wavelengths between 3.2 and 3.4 m. Figure 6.5b shows number density versus distance, measured by accumulating 500 shots for λ_{off} and λ_{on}, respectively.
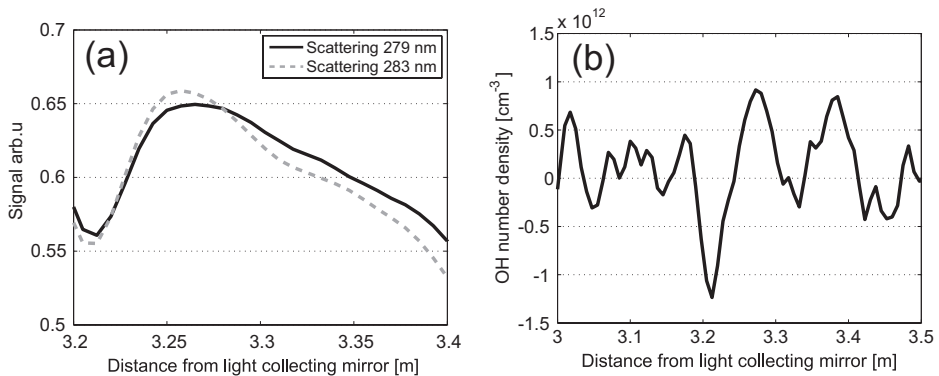

Figure 6.10   *Measurement of OH with a slot burner positioned at ~3.2 m. Panel (a) shows the lidar signals from the on- and off resonance wavelengths, 283 and 279 nm, respectively. In (b) the evaluated concentration profiles are shown. The most prominent feature, the negative peak, is probably due to resonance fluorescence giving a positive signal contribution to the lidar curve at the on resonance wavelength 283 nm, which is seen as the overshoot at 3.25 m in (a).*

The number density curve makes it likely, but not without doubt, that OH is present close to 3.3 m. This position is shifted 10 cm compared with the position for the OH fluorescence at 310 nm seen in Section 8.1.1. The most prominent feature in fig. 6.5b is the negative peak close to 3.2 m, which is in very good agreement with the position of the 310 nm fluorescence peak. The origin of the

negative number density peak is most likely due to weak resonance fluorescence, $A(v=1) \rightarrow X(v=0)$, which can be seen as an overshoot of the collected 283 nm signal, relative to the 279 nm signal, in fig. 6.5a (note that the y-scale is zoomed in). Moreover, it is observed in figure 6.5a that the fluorescence contribution to the 283 nm signal is about the same size as the absorbed fraction of the scattered signal. Consequently, the relatively weak resonance-fluorescence is strong enough to dominate the number density evaluation as observed in fig 6.5b. Hence it seems more promising, using this particular experimental setup, to use the stronger fluorescence at longer wavelength, i.e. the $A(v=0) \rightarrow X(v=0)$ band located around 310 nm, for OH detection, which is further addressed in Section 8.1.1.

Chapter 7

Picosecond lidar Rayleigh scattering thermometry

The most straightforward way of measuring temperatures using laser light is probably Rayleigh scattering thermometry (RST), which in its simplest form does not require any spectral knowledge about, or treatment of, the detected signal. It is a method that can be realized with a relatively simple experimental setup. The biggest weakness of the technique is that it is prone to interfering signal contributions due to particle induced scattering, which limits its applications to relatively clean environments.

A comprehensive review of laser Rayleigh scattering, including RST, for combustion studies is given by Zhao and Hiroyasu (1993). Within the combustion research community RST has been utilized for several decades, initially experimentally limited to one-dimensional measurements (Dibble and Hollenbach, 1981) and later in more complex measurement geometries, such as two-plane, two-dimensional (Mansour, 1993).

However, common to all previous applications is that they are all based on configurations in which the signal is collected more or less perpendicularly relative to the propagation direction of the laser beam, while RST employing ps-lidar utilizes the backscattered signal.

7.1 Rayleigh scattering thermometry (RST)

Rayleigh scattering was discussed in Section 4.1, where eqs 4.5-4.6 describe the expected scattering from one scatterer, from which the following effective Rayleigh scattering cross section, σ_R, for a mixed gas is defined:

$$\sigma_R = \sum_i X_i \sigma_{R,i} = \frac{\pi^2 9 \cdot \sin^2 \phi}{N^2 \lambda^4} \times \sum_i \left[X_i \left(\frac{n^2 - 1}{n^2 + 2} \right)^2 \right] \tag{7.1}$$

where X_i, and $\sigma_{R,i}$ are the mole fraction and Rayleigh scattering cross section of molecule i, respectively.

As mentioned in Section 4.1, the scattering from multiple scatterers is the sum of the scattering from all individual scatterers, hence the Rayleigh scattered light within a certain solid angle, Ω, is given by:

$$I_s(\Omega) = I_0 N l \sigma_R(\Omega), \tag{7.2}$$

where I_0 is the incident light intensity, N is the total number density of the gas, and l is the length of the volume containing the contributing molecules. Combining eq. 2.4, the ideal gas law, and eq. 7.2 leads to the expression:

$$I_s(\Omega) = \frac{I_0 l \sigma_R(\Omega) p A_0}{RT} = \frac{k I_0 \sigma_R(\Omega) p}{T}, \tag{7.3}$$

Where $k = lA_0/R$ is a constant. To extract the temperature, T, a measurement in a volume with known temperature, T_i, is used as reference. Then, the ratio between the signal intensity measured from the volume of unknown temperature and the intensity measured in the reference volume is given by

$$\frac{I_s(\Omega)}{I_i(\Omega)} = \frac{I_0 \sigma_R(\Omega) p T_i}{I_{0,i} \sigma_{R,i}(\Omega) p_i T} \tag{7.4}$$

yielding an expression for the temperature:

$$T = \frac{I_i(\Omega) I_0 \sigma_R(\Omega) p}{I_s(\Omega) I_{0,i} \sigma_{R,i}(\Omega) p_i} \times T_i \tag{7.5}$$

It is readily seen that any variation in laser power and/or pressure between the two measurements will influence the evaluated temperature. If these potential error sources are considered insignificant, the only parameter left influencing the result, apart from the measured intensities, is the ratio between the Rayleigh cross sections, σ_R.

In combustion studies, the compositions of the volume of interest and the reference volume are usually different, i.e. $\sigma_R \neq \sigma_{R,i}$, which implies that the composition of the volume of interest must be known, or at least estimated, in order to obtain a reliable temperature. Since the reference volume can be chosen freely, its composition is of course well known. If the measurement is disturbed by particulate scatterers, σ_R will change in an unpredictable way (in fact it will be Mie scattering from the particles), making quantitative temperature measurements virtually impossible.

The variation in effective Rayleigh cross section from reactant, through intermediate, to product zone in different premixed flames has been carefully investigated by Namer and Schefer (1985). Barat et al. (1991) demonstrated that it is possible to measure bimodal temperature distributions in situations with high levels of interfering scattering. They measured and compensated for laser pulse energy fluctuations and utilized the polarization properties of the scattered light to suppress interfering scattering from the inside of a combustion chamber. Further on they applied an intelligent routine (iterative constrained reconstruction algorithm) to indirectly deconvolve the shot-noise smearing of the evaluated temperature probability functions (PDFs).

The temperature PDF of the evaluated temperatures will depend on the distributions of the two measured intensities, I_i and I_s. A lower signal-to-noise ratio (SNR) in I_s will lead to a higher expected value, i.e. higher average temperature, in the evaluated temperature PDF. This is due to the fact that the expected value of the ratio of two normally distributed variables, X_1 and X_2, is not the same as the ratio of the mean values, μ_1 and μ_2, of the two variables. Specifically, increasing the standard deviation in the normal distribution of the denominator, σ_2, leads to higher expected value of the ratio of the variables.

Simulated PDFs, from Paper II, corresponding to some realistic ps-lidar SNRs are shown in fig. 7.1. The SNRs of the measured signal intensities, I_s, are shown in the legend and they correspond to the following SNRs of the reference intensities, I_i:

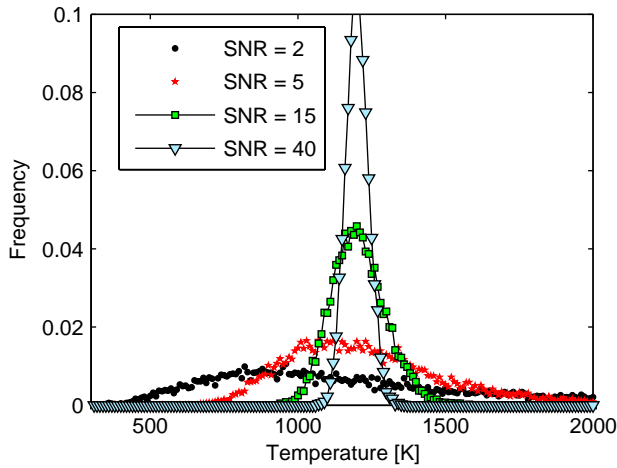| I_s:	2	5	15	40
I_i:	5.8	11	29	50

Figure 7.1 *Simulation of evaluated temperature distribution for Rayleigh scattering thermometry at 1200 K with different SNR in the reference (300 K) and measurement (1200 K) signals. In the legend the measurement SNRs are shown.*

The PDFs are skewed to the right, with peaks shifted towards lower temperature and center of gravity shifted towards higher temperature as SNR increases. The mean values of the temperature distributions corresponding to SNR 5, 15, and 40, as indicated in the legend, are 1252 K, 1205 K, and 1201 K, respectively.

7.2   Applications of ps-lidar RST

For RST in ps-lidar configuration, i.e. collection of backscattered light, interferences from particle scattering are generally different than for perpendicular collection geometries due to the scattering phase functions (SPFs). When discussing SPFs, the absolute size of the scatterers is normally not used as parameter. Instead, the following dimensionless parameter, x, relating the particle size (diameter when spherical), d, and the wavelength of the incident light, λ, is often used.

$$x = \frac{\pi d}{\lambda} \tag{7.6}$$

Steinacker et al. (2003, figs 3 and 4) illustrated how the SPF changes towards forward scattering when x increases from $x<<1$, i.e. particles in the Rayleigh regime, to $x=16$. The fraction of backscattered light decreases more than the perpendicularly scattered light with increasing x, which might be a reason for scattering interference to appear less disturbing for lidar RST compared to conventional RST employing perpendicular detection geometry.

The interesting backscattered part of the light is presented in a detailed study of the SPF between 170-180° with x varying from 16 to 212 (Sugimoto, 1999). In this study it can be seen that by avoiding light collection between the scattering angles 179° and 181°, the most intense particulate backscattering can be quenched. In the ps-lidar setup the outcoupling mirror (fig 5.2, mirror M1) acts as a central obscuration disc, which from a collection distance of 2 m blocks the central solid angle ~1.2°. Real scatterers are in many cases not spherical and the issues with non-spherical scatterers have been addressed in a model by Sharma and Roy (2000).

7.2.1 Flame measurements

Measurements on a Bunsen burner and a porous-plug burner, of McKenna type, were carried out to investigate the potential for spatially resolved temperature measurements in flames at different burning conditions (Paper I).

Single shot results were acquired from measurements in a premixed Bunsen burner flame. Figure 7.2a shows a streak camera image where the scattered laser light is observed as a horizontal dark band. At the distance ~252 cm, a peak in the signal is seen (dark circle) surrounded by a circular structure of lower intensity (lighter). The low-intensity circular structure is due to the lower density of scatterers within and outside the cone-shaped reaction zone.

Integration of 20 centrally located pixels along the y-axis in each column results in the curve shown in fig. 7.2b. The one-dimensional temperature curve presented in 7.2c was obtained by using eq. 7.5. Differences in Rayleigh cross section at different locations in the flame were neglected and the reference signal was assumed to be the linear interpolation, i.e. a straight line, over the double valley structure shown in fig. 7.2b. Accounting for the difference in cross sections between the product gas of the flame and the ambient air (reference) of a stoichiometric flame typically contributes with a factor 1.3 to the temperature peaks. Nevertheless, the temperature is still expected to be underestimated, due to the limited spatial resolution, i.e. 1.2 cm, in these measurements.
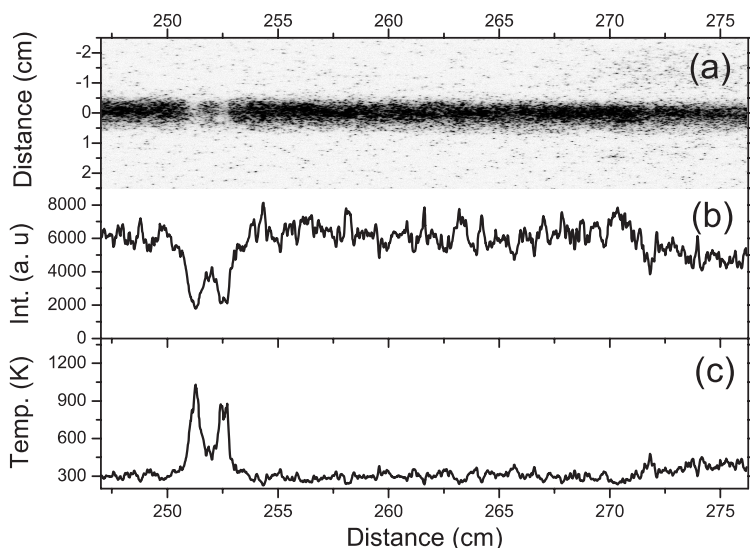
Figure 7.2 *Single shot lidar measurements with a Bunsen flame located 2.52 m from the light collecting lens. Panel (a) shows a two-dimensional Rayleigh scattering image. In (b) the vertically integrated profile is shown. Panel (c) shows the temperature profile extracted from the curve shown in b.*
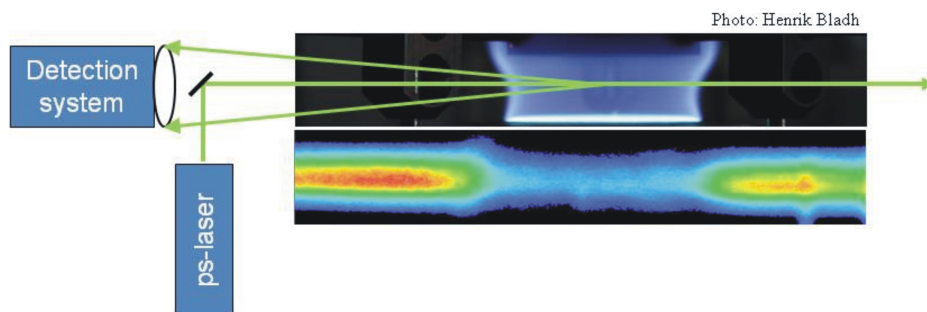

Figure 7.3 *Schematic image of the experimental setup for two-dimensional RST on a premixed ethylene flame a porous plug burner. A two-dimensional lidar image (100 accumulations) of a stoichiometric flame is shown beneath the photograph.*

To explore the technique in a well characterized experiment, a McKenna burner provided a flat ethylene flame, which has been studied previously using coherent anti-Stokes Raman scattering (CARS) for pointwise temperature measurements in the product gases (Vestin et al., 2005). Figure 7.3 shows a simple illustration of the experiment together with a measurement result, which

corresponds to the detected scattered light as if seen from above in the upper image (photograph) of the flame.

The corresponding two-dimensional temperature map obtained with ps-lidar, accumulating 100 laser shots in a stoichiometric flame, is shown in fig. 7.4. The Rayleigh cross sections of the product gases were accounted for using mole fractions reported for the CARS experiment by Vestin et al (2005).

The porous plug is 6 cm in diameter, which is also revealed in the temperature image. The outer part of the image along the y-axis, outside ±0.6 cm, corresponds to an area located in the wings of the laser beam profile, hence resulting in noisier temperature data. The temperatures are in good agreement with the point measurement by CARS, i.e. 1700 K.
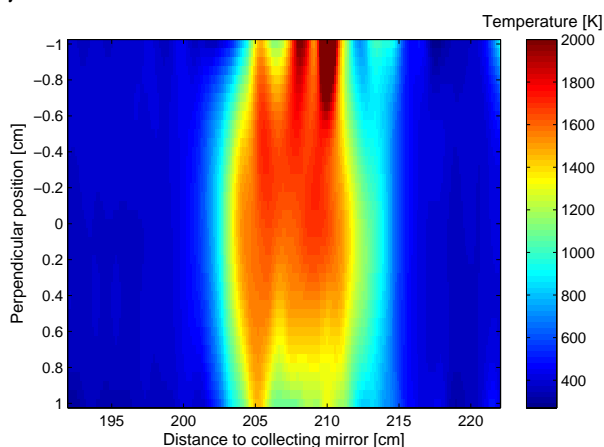

Figure 7.4   *A two-dimensional RST image of the stoichiometric flame illustrated in fig. 7.3.*

To study the influence of interfering particle scattering on the evaluated temperature, the equivalence ratio was varied from 0.5 to 2.0. Temperatures measured in a region above the center of the burner was compared with the corresponding temperatures measured with CARS. The comparison is shown in fig. 7.5, where ps-lidar temperatures are indicated with circles, whereas CARS temperatures are marked with stars. The agreement between ps-lidar and CARS temperatures is very good up to an equivalence ratio of 1.3. At higher equivalence ratios, scattering from PAH and soot interfere with the molecular Rayleigh scattering as expected, which results in underpredicted temperatures.
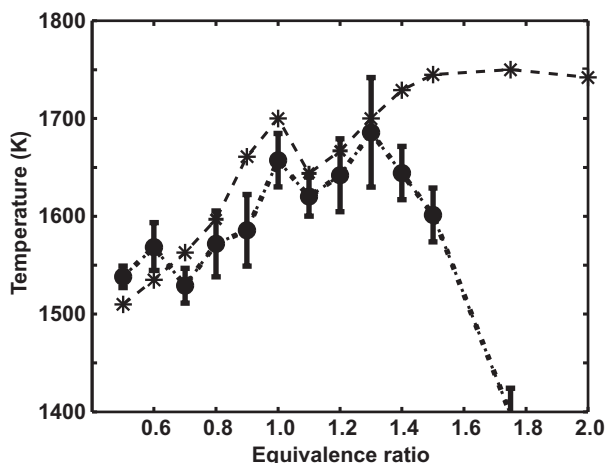
Figure 7.5   *Temperatures measured using RST in a premixed ethylene flame on a porous plug burner (circles) and temperatures measured with CARS (stars) (Vestin et al., 2005) in the same burner.*

7.2.2 Furnace measurements

To demonstrate the ability of measuring temperature with ps-lidar through a highly scattering medium, measurements were made with a sooty porous plug burner diffusion flame blocking the optical access of a tube furnace (Paper II), see fig. 7.6. The laser beam path is indicated with a line through the flame.
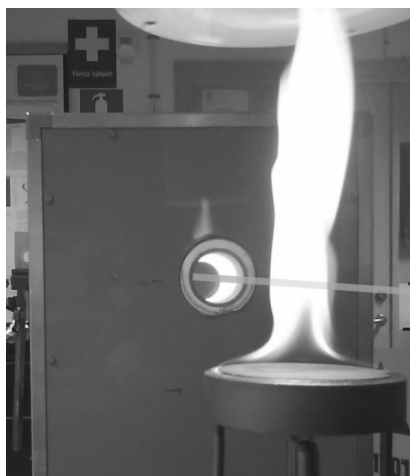

Figure 7.6   *Photograph of the measurement objects: Sooty flame on porous plug burner in front of a tube furnace.*

It was demonstrated that it was possible to map particle scattering in the volume surrounding the flame and simultaneously perform RST in the gas volume inside the furnace. The laser pulse energy was ~3 mJ and the laser wavelength was 532 nm.

Two-dimensional results of two such measurements are seen in fig. 7.7. The images shown in fig. 7.7 are divided into two parts by a vertical dashed line. The left parts show scattering signal, in arbitrary unit, giving a qualitative map of the particle density, and the right parts show evaluated temperatures.
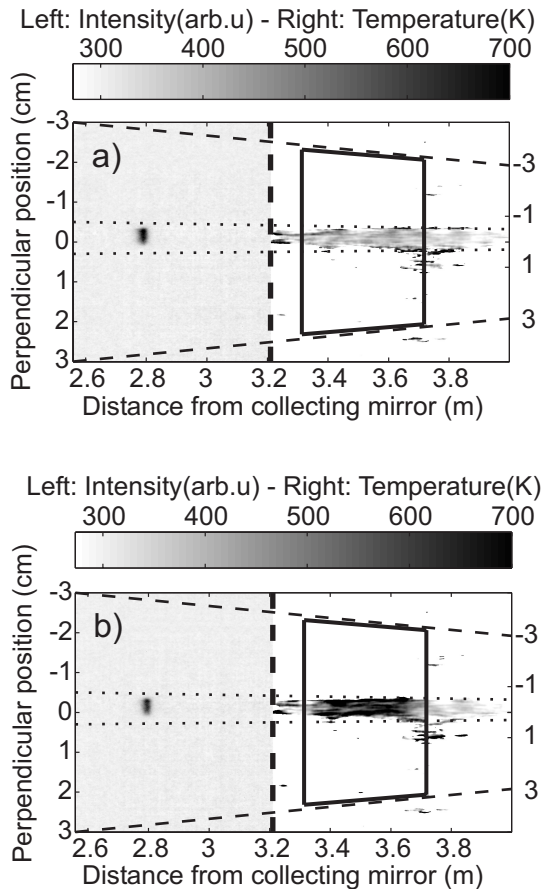
Figure 7.7 *The left parts of the images show Rayleigh scattering and the right parts show evaluated Rayleigh thermometry temperatures. The solid box indicates the position of the furnace tube and the inner pair of horizontal dotted lines indicates the outer limits of the laser beam propagation. Thermocouple readings in furnace at 3.5 m are in (a) 363 K and (b) 578 K.*

The dynamic range of the signal covering both parts is normally very high. In order to obtain a reasonable SNR in the right part of the image, optical suppression of the particle induced signal was carried out. The area inside the inner pair of dotted horizontal lines corresponds to the laser beam path. The outer pair of dashed horizontal line is representing ±3 cm in the coordinate system. The solid line trapezoid indicates the position of the furnace tube. The thermocouple readings in the center of the furnace tube were 363 and 578 K, for the data presented in fig. 7.7a and 7.7b, respectively.

To be able to interpret the results and to validate the measurement concept, i.e. ps-lidar Rayleigh thermometry, two measurement series using a thermocouple sequentially placed at different positions inside the furnace tube were undertaken. The resulting one-dimensional thermocouple temperature profiles and the corresponding lidar data, measured without the obstructing flame in front of the furnace, are shown in fig. 7.8. The legend indicates the thermocouple readings in the center of the tube, at the distance 3.5 m. The result shows that the Rayleigh temperatures agree very well with the thermocouple readings.
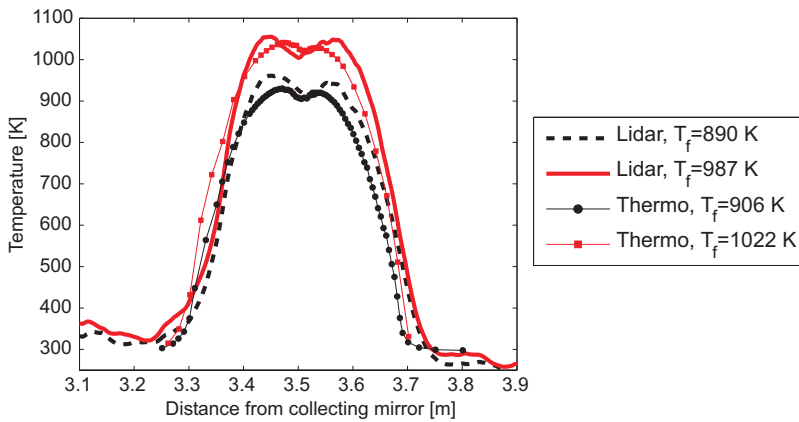
Figure 7.8 *Temperature measurements in the tube furnace. Lines indicate lidar temperatures and markers indicate the thermocouple readings for the furnace temperatures indicated in the legend.*

Knowing the spatial temperature profile inside the furnace, a series of measurements with different furnace temperatures was conducted with the obstructing flame in front of the furnace. The resulting one-dimensional temperature profiles are shown in fig 7.9a. Point temperatures evaluated at 3.5 m for these temperature profiles are shown if fig. 7.9b together with the thermocouple reading at the same position.

Even though the signal intensities are substantially reduced, due to the strongly reduced light collection needed to permit simultaneous mapping of particle scattering, the one-dimensional temperature profiles agree with the expected profiles.

At higher temperatures, the measured temperatures are overpredicted, which also causes the peak structure to be exaggerated. The overprediction is most likely due to the low signal-to-noise ratio, strongly impacting the evaluated temperature as it goes into the denominator of eq. 7.5, which was discussed in conjunction with fig. 7.1.

The point temperatures agree well with the thermocouple readings, which, with respect to the previously discussed overprediction, suggests that the integrated signal in the region around 3.5 m has an adequate signal-to-noise ratio.
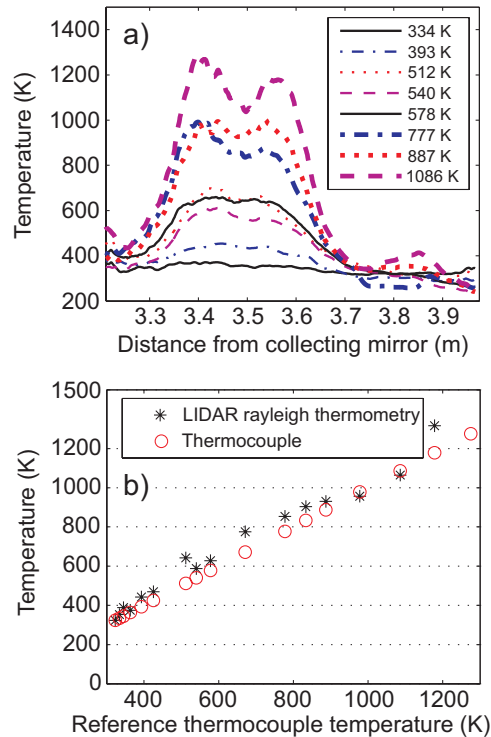
Figure 7.9 *Lidar Rayleigh scattering thermometry in a furnace at different furnace settings with thermocouple giving reference temperatures. A sooty porous-plug burner flame is positioned at 2.8 m a) One-dimensional RST at eight furnace settings. Thermocouple readings are indicated in the legend. b) Point RST in a point corresponding to 3.5 m in fig 6a. Rayleigh scattering thermometry temperatures shown as stars and thermocouple reading shown as circles.*

7.2.3 Room-fire measurements

The first use of ps-lidar in a large scale application, was for Rayleigh thermometry in a fire research experiment (Paper IV) using a small room (½-scale ISO 9705), with dimensions $117 \times 188 \times 120$ cm (width × length × height), respectively. The door opening was 50×107 cm and centered on one of the 117 cm walls.

Figure 7.10 shows photographs of parts of the experimental setup. The left picture shows a methane flame burning inside the room. A laser pulse reflection is visible on the inner wall of the room. In the door opening, the positions of thermocouples used for temperature reference are indicated with red solid circles. To the right, the laser beam path is exaggerated with green lines for clarity and the thermocouples are again indicated with red solid circles.
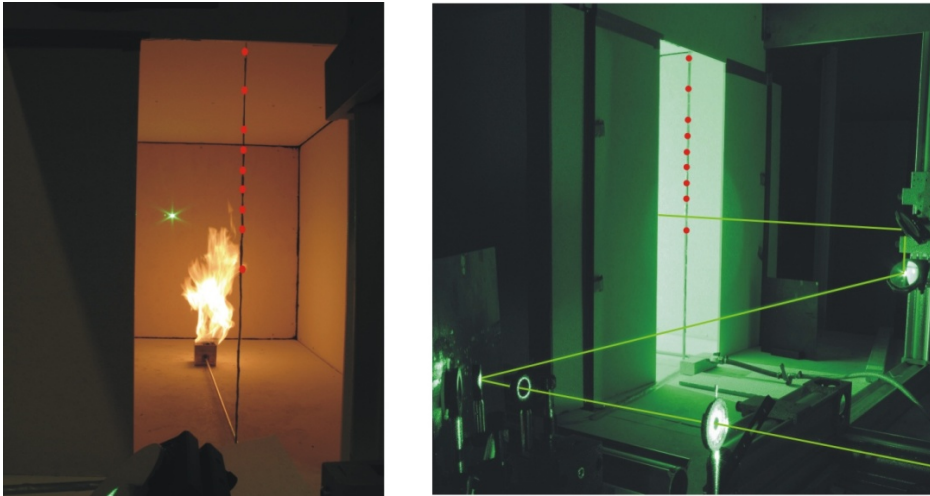
Figure 7.10   *To the left a photograph of a methane flame burning inside the room. The positions of the thermocouples are indicated with red dots. To the right is a photograph of parts of the experimental setup. The laser beam path is exaggerated and is seen being directed by the outcoupling mirror in the left part of the photograph. A periscope arrangement can be seen to the right directing the laser beam into the room. The thermocouples are again indicated with red dots.*

In fire research, the use of computational fluid dynamics (CFD), allowing multidimensional temperature information, is widely used. In order to validate CFD calculations, non-intrusive measurement techniques, yielding large scale

two-dimensional temperature images, are highly needed. Laser based measurements conducted previously have been limited to point measurements using CARS, e.g. demonstrated by Aldén and Wallin (1985), and line-of-sight absorption measurements, for example by Sappey et al. (2004).

Using a methane flame on a gas burner filled with granule and sand, as shown in fig. 7.10, resulted in scattering strongly dominated by particulate matters, hence inhibiting Rayleigh thermometry. However, changing to a methanol pool fire allowed ps-lidar measurements to be conducted.

A resulting two-dimensional temperature image of a vertical plane (y-z plane) 6 cm outside the door is shown in fig. 7.11a, where the door posts are indicated with the dashed vertical lines. In fig. 7.11b, the corresponding temperature result of a CFD simulation of a vertical plane positioned in the door opening, i.e. 6 cm from the plane in fig. 7.11a, is shown.

In Paper IV, a simulated temperature image of a plane located at the same position as in fig. 7.11a is illustrated. The result of the CFD simulations of the whole room shows that the steepest temperature gradients, except for very close to the flame, are found a few centimeters outside the door opening. Hence, fairly large errors could be expected when comparing ps-lidar and simulated temperatures in a thin vertical plane outside the door opening.
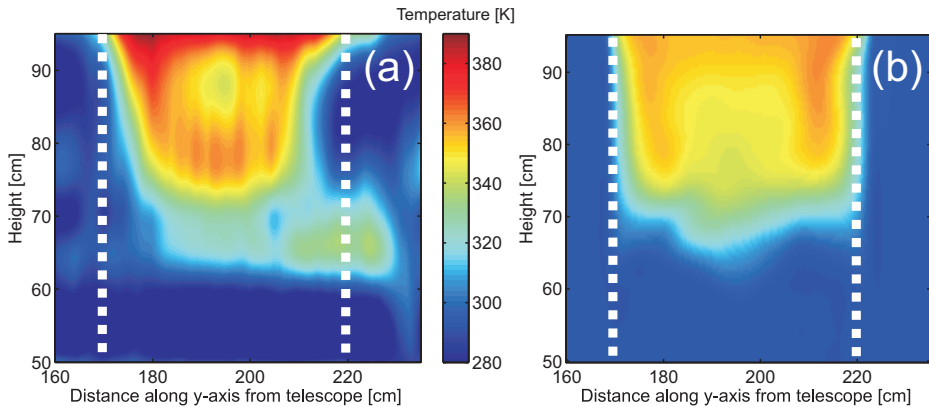

Figure 7.11 *Temperature images of the y-z plane 6 cm outside the door measured with lidar is shown in (a), while (b) shows a simulated temperatures of a plane in the door way, i.e. 6 cm from the lidar plane.*

Another illustration of the temperatures is given in fig. 7.12, where point temperatures from simulations and measurements in the plane 6 cm outside the

door opening at the heights and distances of the thermocouples are compared with the thermocouple readings.
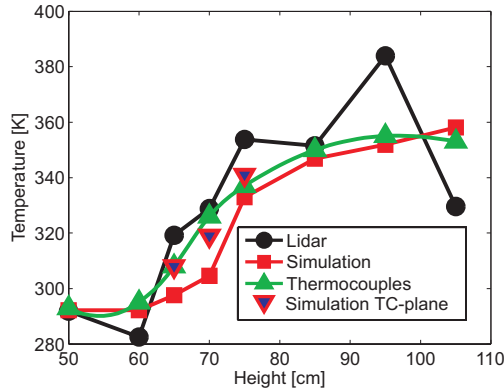
Figure 7.12   *The lines indicate thermocouple readings, the resulting temperatures from lidar measurements, and CFD simulations at the heights and y-position of the thermocouples in a plane 6 cm outside the door opening. The downwards pointing triangles indicate simulated temperatures in the y-z plane of the thermocouples.*

The downwards pointing triangles indicate the simulated temperatures in the plane of the thermocouples, i.e. the door opening. Two-dimensional temperature images of horizontal planes, at a height of 75 cm inside the room, are shown in fig. 7.13, where panel (a) shows lidar data and (b) simulated results.

Figure 7.13   *Temperature images of a plane at height 75 cm. The color scale is common for the two images. Panel (a) shows lidar results and panel (b), shows results from CFD simulations.*

As can be seen in fig. 7.13, the simulated temperature distributions are very uniform in the plane. The lidar image is created using cubic spline functions between temperature curves at the following distances across the door opening: 5, 13, 21, 29, 3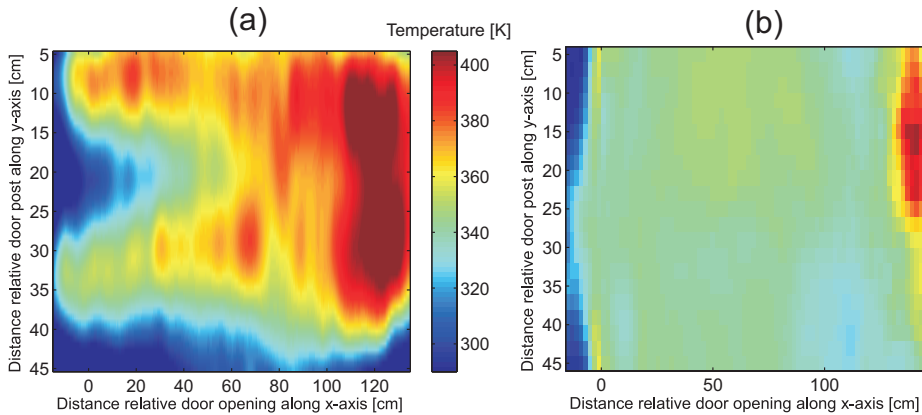7, and 45 cm. Fluctuations in laser pulse energy between measurement series, having a relative standard deviation of around 10%, are not corrected for.

These fluctuations are probably the main reason for the large-scale vertical temperature structures observed in fig. 7.13a. However the horizontal structures, for example the increase in temperature at the vertical position 20-25 cm, are more likely to be due to actual temperature dynamics inside the room. There is also a possibility that the effect of a temperature decrease towards the door opening might be due to enhanced particle scattering in that area of the room.

The lidar data shown in fig. 7.13a is an example of a result that would be very difficult to achieve using other non-intrusive measurement techniques, while results such as the one presented in fig. 7.11a is in principle possible to obtain using other experimental setups, as for example shown by Seyfried et al. (2005).
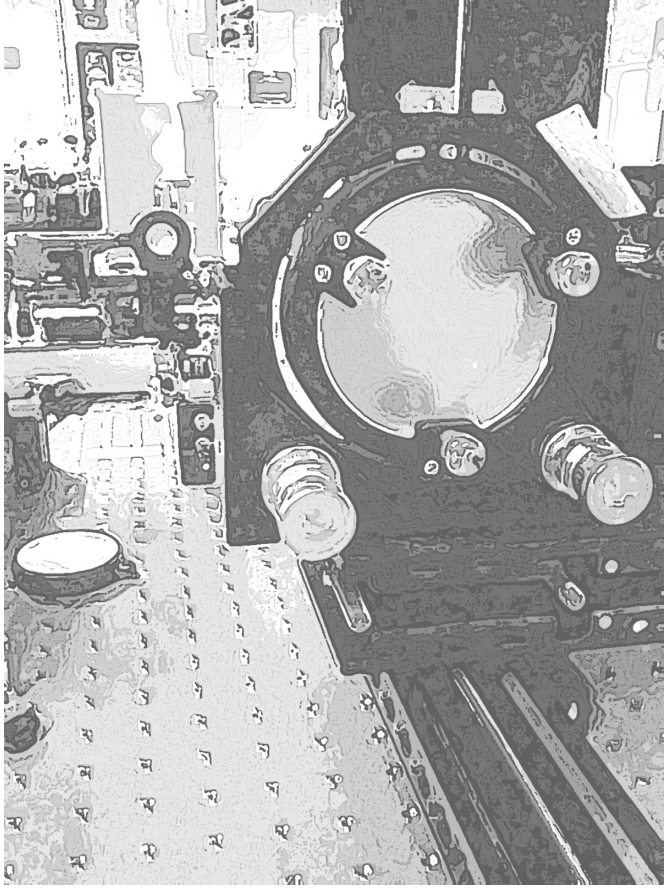
Chapter **8**

Picosecond lidar – utilizing frequency shifted signals

The measurements yielding the results presented in Chapters 6 and 7 utilize elastically scattered light, i.e. light with the same frequency as the laser light. In this chapter, signals that are shifted in frequency will be discussed. The detection of such signals are often more challenging, since the signals are either weaker, making them difficult to detect, or long-lived, which may impair the achievable range resolution in ps-lidar. With adapted experimental setups and assumptions about the acquired signals, though, it is possible to use laser-induced fluorescence, laser-induced spontaneous Raman scattering, and laser-induced incandescence, in combination with ps-lidar.

8.1   Laser-induced fluorescence

Laser-induced fluorescence generally exhibits a relatively strong signal, with species-specific features both regarding excitation wavelength and emission spectrum. These characteristics make it very attractive to combine LIF with ps-lidar. The major challenges for such a combination are the need of a tunable laser source, spectral separation of scattered light and fluorescence, and treatment of the fluorescence lifetime, which is also quenching dependent. The fact that

fluorescence, unlike scattering, exhibits a temporal decay, characterized through its decay constant, i.e. the lifetime, is of course a major challenge as it opposes the range-resolving capacity of ps-lidar.

As discussed in Section 2.2, the distribution of molecules in different energy levels is dependent on temperature. Probing different molecular energy levels using excitation wavelengths corresponding to the energies of molecular transitions from the probed states to a common upper state will result in LIF signals being proportional to the population in the different initial states. The temperature may then be determined from the relative strengths of these LIF signals. The use of fluorescent tracers for temperature and fuel concentration measurements in practical combustion applications has been reviewed by Schulz and Sick (2005).

Experiments based on two excitation wavelengths, probing the population in two different energy states for temperature measurements, has been performed by Einecke et al. (2000) using 3-pentanone as tracer, and by Fujikawa et al. (2006) using toluene. A novel variant of LIF for temperature measurements using only one excitation wavelength, but detecting the LIF signal in two wavelength bands, has been demonstrated by Luong et al. (2008).

However, in the present work, range resolved fluorescence ps-lidar measurements of hydroxyl radicals (OH) were performed using a tunable laser source. Being the first tentative tests of the measurements concept, no attempts to extract quantitative OH concentrations or temperatures were made.

8.1.1 OH measurements in a flame

Employing a slot burner (Perkin-Elmer), positioned at 3.2 m from the collection optics, OH radicals in the flame were excited via the $A(v=1) \leftarrow X(v=0)$ transition using 283-nm laser pulses from the OPG/OPA system.

In the DIAL study, described in Section 6.2.4, a 281-nm interference filter (Acton) was used to discriminate against the strong fluorescence of the $A(v=0) \rightarrow X(v=0)$ transition, around 310 nm. Still, weak resonance fluorescence was observed superposed onto the scattering signal. In the study presented here, the strong fluorescence present at around 310 nm was the signal of interest, and therefore a 310-nm interference filter (Acton) was used to reject elastically scattered light.

Laser-induced fluorescence, particularly applied for OH detection, is a very well-established laser diagnostic technique, which has been widely used in

combustion research for several decades (Bechtel and Teets, 1979; Aldén et al., 1982; Kychakoff et al., 1982).

Figure 8.1 shows scattering from 283 nm (red dashed line) as well as the non absorbed scattering at 279 nm (solid black line). Fluorescence emitted around 310 nm is shown as the blue solid line in the same figure. The region where the scattered signal falls off, due to the hot gas above the burner, is zoomed in to illustrate detailed fluorescence and absorption features. As can be seen in the zoomed part, the scattering at 283 nm (red dashed line) drops below the 279-nm scattering (black solid line) after a small overshoot at ~4.1 m. The initial overshoot is probably caused by resonance fluorescence, i.e. the A(v=1)→X(v=0) transition at ~283 nm, and the subsequent signal reduction is most likely due to absorption of the 283-nm light. The fluorescence from A(v=0)→X(v=0) is amplified 20 times to be plotted in the same diagram.
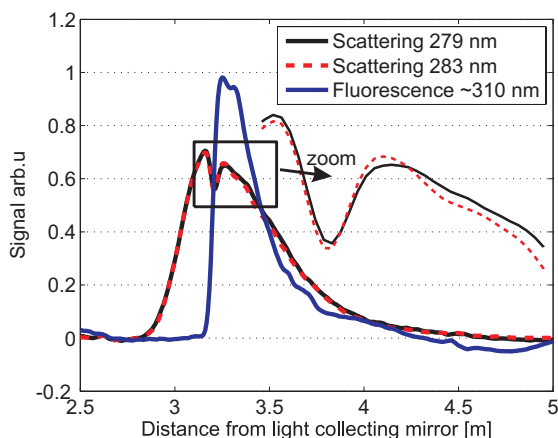
Figure 8.1 *Lidar signals recorded using the laser wavelengths 279 and 283 nm, respectively. Light at 279 nm (black line) is not absorbed by OH, whereas light at 283 nm (red dashed line) is absorbed by OH present in the slot-burner flame. Fluorescence from around 310 nm (blue line), collected using a 310-nm band pass filter, is also shown. The content inside the black box is magnified and shown to the right of the box.*

The laser pulse passes above the burner as indicated in fig. 8.2. Since the flame has the shape of a thin sheet (1 mm thickness), the overlap between the flame and the unfocused laser beam (~10 mm diameter) is small, which results in weak OH absorption. This is the major reason why the OH fluorescence (blue solid curve) is about 20 times weaker than the scattering signal. Nevertheless, the fluorescence

signal, $S(t)$, is very clearly observed since it is collected with essentially zero background.

Results obtained after further treatment of this signal is shown in fig. 8.3a, where the natural logarithm of the signal is plotted versus distance together with a linear fit to its decay. The fluorescence lifetime was determined to be 1.3 ns, which deviates somewhat compared with OH lifetimes reported in the literature, e.g. 1.8 ns by Bergano et al. (1983) and 2.0 ns by Schwarzwald et al. (1987).
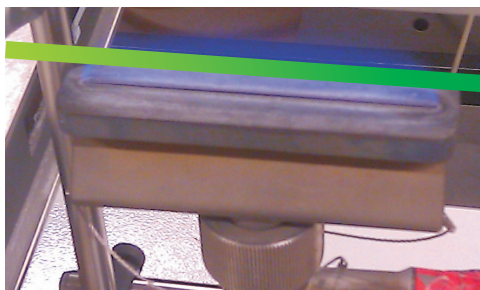
Figure 8.2 *A slot burner was used as measurement object, providing a thin reaction zone positioned along the slit seen in the burner top surface. The propagation of the laser pulse is indicated above the burner.*
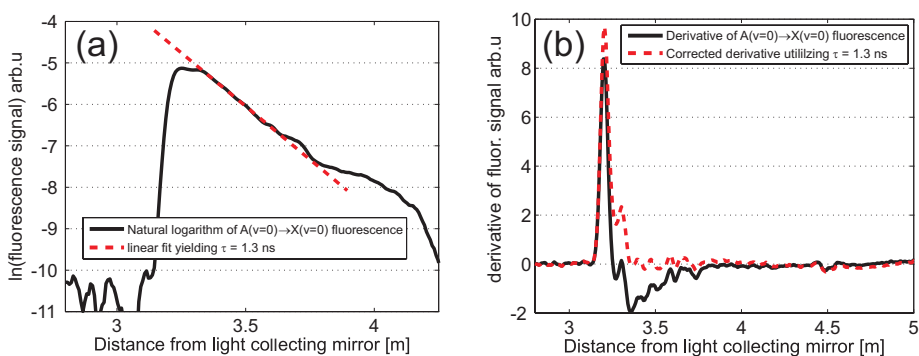
Figure 8.3 *Panel (a) shows the logarithm of the OH fluorescence signal, originating from above the slot burner, and a linear fit to the decaying part of the signal. The x-axis is converted into distance since it is a lidar result (time would normally be used in studies of fluorescence decays). In (b) the derivative and corrected derivate, corresponding to a qualitative mapping of the OH distribution, are shown.*

It is assumed that the fluorescence decay is well described by a single-exponential function, same throughout the entire measurement volume. Further it is assumed that the lifetime of the detected signal, after the laser pulse has passed a spatially extended fluorescence source, e.g. the 10-cm long flame containing OH, is the same as all the individual lifetimes of each signal source within the fluorescing volume, following the argument in Paper V.

The derivative of the fluorescence signal, $D(t)$, is shown by the black solid curve in fig. 8.3b. This curve might be used as an indicator for where contributions to the LIF signals, i.e OH radicals, are located. If the negative derivative of the fluorescence decay curve, $E(t)$, is removed, the remaining signal, $G(t)$, directly reflects where the increase in LIF signal is situated.

In order to calculate $G(t)$, the decay constant, α, corresponding to the lifetime, τ, 1.3 ns here, is utilized to remove the derivative caused by $E(t)$, i.e.

$$G(t) = D(t) + \alpha S(t) \qquad (8.1)$$

Since the rise time of the detected LIF signal is on the order of the laser pulse duration, ~80 ps, and the time resolution is around 1 ns, the last term of the equation is a good approximation of $E(t)$. The red dashed line in fig. 8.3b represents the calculated $G(t)$.

The following assumptions are made. 1) The positive derivative is proportional to the peak fluorescence value of a fluorescence curve originating from one specific distance. 2) The peak fluorescence signal is proportional to the number density of the fluorescing molecule.

Assumption 1 was shown to be a good approximation in the work presented in Paper V. Assumption 2 is true if fluorescence quantum yield is constant, i.e. ignoring potential spatial variations in quenching. The curve is thus a one-dimensional map of the OH number density distribution. If the signal intensity is calibrated in a point with known concentration (not zero), the curve would represent the OH distribution quantitatively. An interesting method for separating fluorescing volumes blurred together temporally was introduced and demonstrated by Ossler et al. (1998). However the method is unfortunately not applicable in the lidar case, since it requires knowledge of the position and total fluorescence from each volume beforehand.

8.2 Raman scattering

Raman ps-lidar utilizes the weak Raman scattered light from Raman active molecules. In Section 4.3, theory of Raman scattering was discussed. In atmospheric lidar, Raman signals have been detected by integrating the signal for extensive time periods over long distances, as first reported by Leonard (1967) and later utilized for applied studies by for example Ansmann et al. (1992). Raman scattering has also been demonstrated for stand-off detection of chemical substances on surfaces (Ray et al., 2000), although not range/temporally resolved.

Since the weak Raman scattering of gas phase molecules has not yet been detected with the ps-lidar system, the results presented in this section is from experiments with liquid samples. Stronger Raman signals can be obtained using the resonant Raman effect, which utilizes the non-linear increase in Raman cross section achieved as the excitation wavelength approaches an electronic transition in the molecule.

8.2.1 Range-resolved detection of multiple species

During these measurements, the streak camera was used with a spectrograph positioned in front of it. The collected light is thus dispersed along the slit of the streak camera, providing an image containing temporally resolved spectral signatures. Since the detected signal is a lidar signal, the time resolution is converted into spatial resolution along the optical axis.
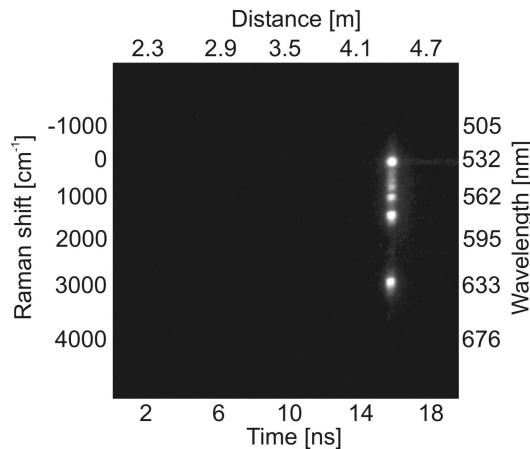

Figure 8.4 *A streak camera image from a lidar experiment on a liquid sample containing nitromethane, positioned at 4.34 m (courtesy of Martin Levenius).*

Figure 8.4 shows a streak camera image acquired in a Raman experiment on a liquid sample containing nitromethane positioned 4.34 m from the collection mirror. The excitation wavelength in this experiment was 532 nm. The image shown in fig. 8.4 was further analyzed by integrating horizontal pixels around 4.3 m, resulting in the curve shown in fig. 8.5.
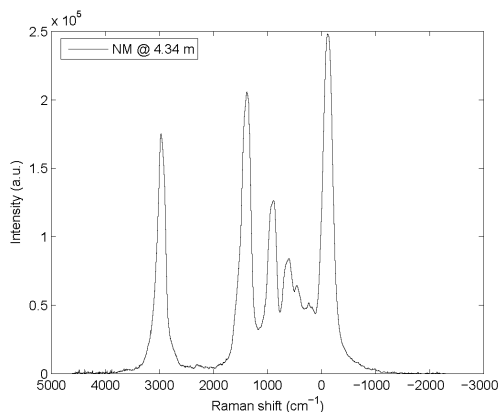
Figure 8.5 *Spectrum of nitromethane obtained by horizontal integration of the data shown in fig. 8.4 (courtesy of Martin Levenius).*

A comparison with spectral line positions available in the literature (Johansson et al., 2010) identifies the spectrum easily as nitromethane. A similar result as the one presented in fig. 8.5 may also be achieved using a spectrometer with a CCD-camera (Ehn et al., 2012c).

To demonstrate one of the real strengths of the Raman ps-lidar technique, experiments were performed having multiple samples, containing different solutions, placed along the optical axis. Figure 8.6 is the result of such a measurement, averaging over 3000 shots, with nitromethane samples positioned at 3.32 and 4.35 m, respectively, and a hydrogen peroxide sample at 3.82 m. The strength of Raman ps-lidar is readily seen in fig. 8.6, clearly demonstrating the ability to make simultaneous range-resolved and species-specific measurements.

Remote detection of explosives using spontaneous Raman scattering, however not range resolved, has been demonstrated by Pettersson et al. (2009) with the target located at a distance of 55 m. The major challenge, in terms of making the technique more versatile and useful in combustion research, is to be able to conduct Raman measurements on gas phase molecules, present at much lower densities than in liquid phase, which has so far not been demonstrated with the ps-lidar system.
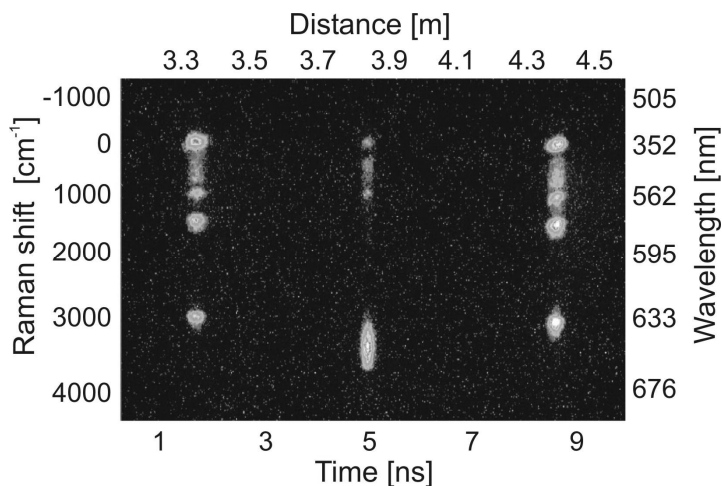
Figure 8.6 *A streak camera image from a lidar measurement performed on three liquid samples containing nitromethane, hydrogen peroxide, and nitromethane, respectively (courtesy of Martin Levenius).*

8.2.2 Near resonant Raman

When the excitation wavelength approaches the wavelength of an electronic molecular transition, the Raman cross section has been found to increase more than five orders of magnitude, and standoff detection at 13-m distance of gaseous samples has been demonstrated using a nanosecond laser (Ehlerding et al., 2011).

An experiment was carried out with the ps-lidar system to verify and investigate the resonance enhancement effect using picosecond pulses. An acetonitrile solution containing ~1 g/l of dinitrotoluen (DNT) was excited using 532 and 266 nm, respectively.

The resulting spectra are shown in fig. 8.7. According to Ehlerding et al. (2011), the resonance effect sets in just below 270 nm to reach a maximum below 260 nm. The two peaks at 1347 and 1611 cm^{-1}, respectively, are identified as Raman lines from DNT. The peak at 2249 cm^{-1} is an acetonitrile peak suitable to use as reference. The expected resonance effect is clearly visible in these data.

Assuming that the residual structure around 1347 cm^{-1} on the red curve is originating from DNT and that acetonitrile is not experiencing any resonance effect, allows a quantitative estimation of the resonance effect by forming the ratio between the intensity of the acetonitrile peak at 1611 cm^{-1} and the intensity of the DNT peak at 1347 cm^{-1}. The resulting enhancement in Raman cross section is then found to be a factor of 22.

The tunable ps laser system was not available at the time of these experiments, so it was unfortunately not possible to tune the laser wavelength further down towards, most likely, even larger resonance effects.
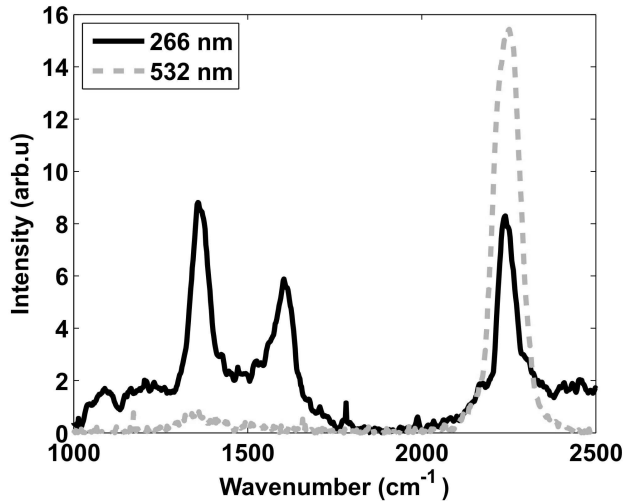
Figure 8.7 *Raman spectra of a solution of DNT in acetonitrile. Two different excitation wavelengths, 266 and 532 nm, respectively, have been used. It is observed that the DNT peaks (1347 and 1611 cm⁻¹) are substantially enhanced when 266 nm is used, indicating the presence of resonance effects.*

8.3 Laser-induced incandescence

Laser-induced incandescence (LII) is a technique mainly for soot diagnostics (Schultz et al., 2006; Santoro and Shaddix, 2002). Soot particles are heated by absorbed laser light and the subsequent heat radiation (Planck radiation), with lifetimes on the order of hundreds of nanoseconds, is detected, from which both soot volume fraction and primary particle size may be determined.

A parameter used in soot diagnostics is, hence, soot volume fraction, f_v, which is defined as the number density, N, of soot particles multiplied with the volume of each soot particle with diameter d, i.e.

$$f_v = \frac{N \pi d^3}{6} .$$

(8.2)

Several decades, during which substantial progress in model development has been made, have passed since the pioneering modeling work by Melton (1984), who presented a nearly linear relationship between LII-signal strength, S_{LII}, and soot volume fraction, f_v:

$$S_{LII} \propto Nd^{3+\frac{0.154\times10^{-6}}{\lambda}}, \qquad (8.3)$$

where λ designates detection wavelength. The equation was derived assuming high laser fluence, ~0.4 J/cm², which implies a high degree of sublimation, necessarily accompanied by bothersome modeling work.

In a thorough study of the relation between S_{LII} and f_v, including time dependence, Bladh et al. (2008) discussed the optimal choice of experimental parameters for achieving linearity. Detecting the prompt (initial) LII signal with shortest possible time gate, applying a long detection wavelength, and using low laser fluence (<0.1 J/cm²) were reported as the best choice of experimental conditions. A disclaimer about the LII signal being dependent of laser fluence at such low laser fluence was given though, since the effect of laser extinction may influence the LII signal. Consequently, without correction for laser extinction, the soot volume fraction evaluation will be affected.
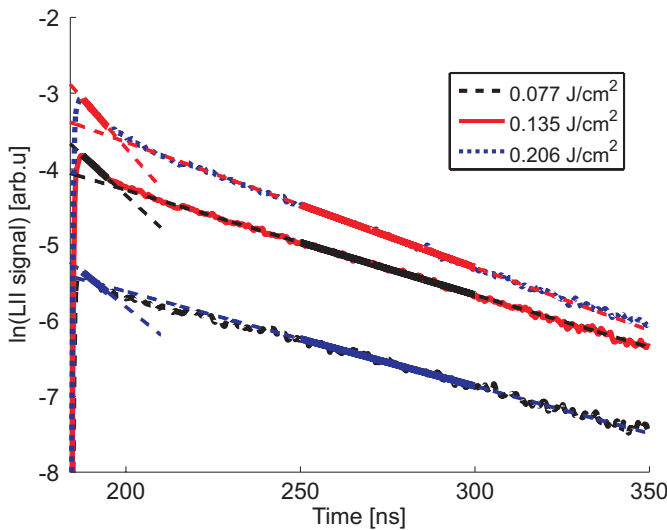

Figure 8.8 *The natural logarithm of time resolved LII signals for three laser fluences, which are presented in the legend. Each experimental curve also has linear fits to the faster initial decay and to the dominating slower decay of the signal.*

Experimental details for the picosecond LII lidar measurements are presented in Paper V. Figure 8.8 shows time resolved picosecond LII signals, for three different laser fluences, recorded in an ethylene/air flame on a porous plug burner with $\phi = 2.1$. The curves consist of a steep rising edge followed by a decaying part. The decay curves appear bi-exponential, and two lifetimes, τ_{short} and τ_{long}, were evaluated accordingly. The physical origin of the fast initial decay, characterized by τ_{short}, is probably due to initial sublimation and evaporation processes, while the remaining decay, characterized by τ_{long}, is caused by a slower heat conduction process.

A set of LII measurements were undertaken, while varying laser fluence and equivalence ratio, evaluating the two lifetimes for each setting. The lifetimes, together with the ratio between them, are presented in fig. 8.9.

Figure 8.9a shows the lifetime dependence on laser fluence for $\phi = 2.1$, while figs 8.9b-c show the lifetime dependence on equivalence ratio for laser fluences 0.1 and 0.2 J/cm^2, respectively. It is observed that the lifetimes decrease with increasing laser fluence, due to increased sublimation resulting in reduced particle size. Furthermore, it can be seen that decreasing the laser fluence lowers the signal to noise ratio, which is particularly evident in the lifetime ratios.

The long lifetimes, τ_{long}, increase with ϕ, since the primary particle size increases with ϕ (Hadef et al., 2010), yielding a lower heat conduction rate. The ratio τ_{short}/τ_{long} decreases with increasing ϕ for $\phi < 2.3$, which might be an indication of sublimation- and conduction rate having different dependencies on primary particle size, since Hadef et al. (2010) observed that the primary particle size increases the most with ϕ for $\phi < 2.3$.

In Paper V it was also shown that the maximum time derivative of the rising edge of the LII signal is proportional to the peak LII signal (the maximum value of a time resolved single LII signal). The peak LII signal is the best fraction of the LII signal to use in terms of being proportional to the soot volume fraction, according to the recommendations of Bladh et al. (2008). Furthermore, a correction term for analysis of the time derivative of LII lidar signals obtained from spatially extended soot distributions was derived:

$$f_v \propto G'(t) \approx S'(t) + \alpha S(t), \qquad (8.4)$$

where $\alpha = 1/\tau$ is the decay constant, utilizing either τ_{short} or τ_{long} whichever one that is most relevant for the soot present in the measurement volume.
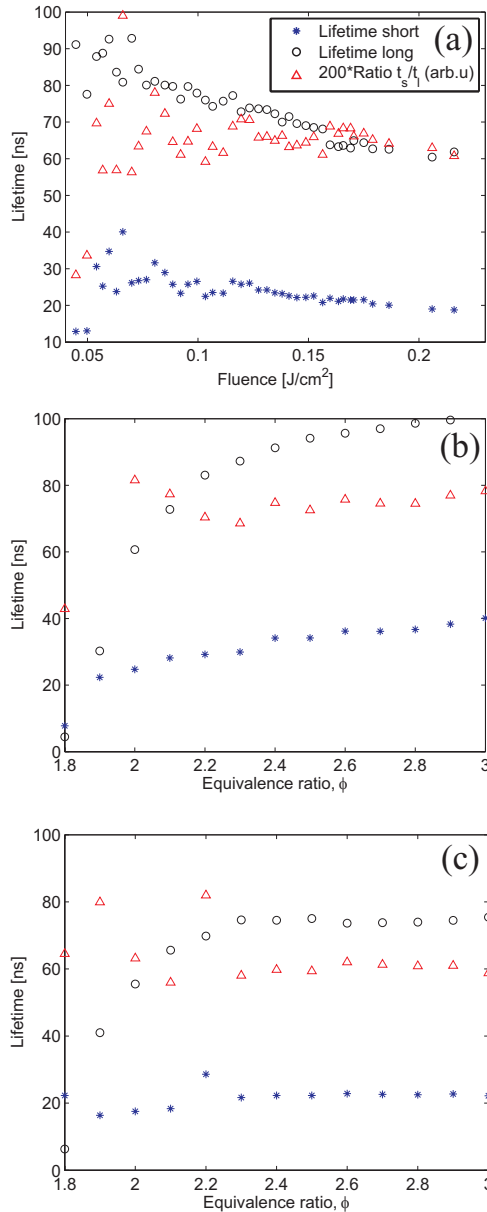
Figure 8.9 *Panel (a) shows the short (stars) and long (circles) lifetime components of the LII signal versus equivalence ratio. Panel (b) and (c) show the lifetimes versus equivalence ratio for the fluences 0.1 and 0.2 J/cm², respectively. The ratios between the two lifetimes are indicated with triangles in all three panels.*

For the measurements reported on in this work, τ_{short} was most relevant, since it dominates the LII signal the first ~10 ns, as can be seen in fig. 8.8, which corresponds to a lidar measurement range, $\Delta x = ct/2$, of 1.5 m.

The short lifetime component, i.e. τ_{short}, can be determined directly from the prompt decay of the acquired LII lidar curve if a region without soot follows after the sooty region. Since the prompt decay can be difficult to determine in a dynamic measurement, it may be easier to measure τ_{long} and then divide this value with the ratio τ_{long}/τ_{short}, which is presented in figs 8.9a-c for different measurements conditions.

To demonstrate the LII ps-lidar concept, measurements were made in two porous plug burners, providing ethylene flames with $\phi = 2.1$, placed along the laser beam path, with one of them movable along the beam path. The center-to-center distance between the burners was varied from 21 to 50 cm in six steps.

The results, evaluated using eq. 8.4, are shown in fig. 8.10 with the distance between the burners indicated in the legend. The LII signals from the two flames are well resolved at all distances. For validation purposes, perpendicular LII measurements using an ICCD camera were carried out simultaneously. These measurements showed that the flame located close to 2.2 m, i.e. the flame on the fixed burner, emitted roughly a factor of two stronger LII signal than the flame on the moveable burner, which is also observed in the lidar result corresponding to the 0.27 m center-to-center distance.
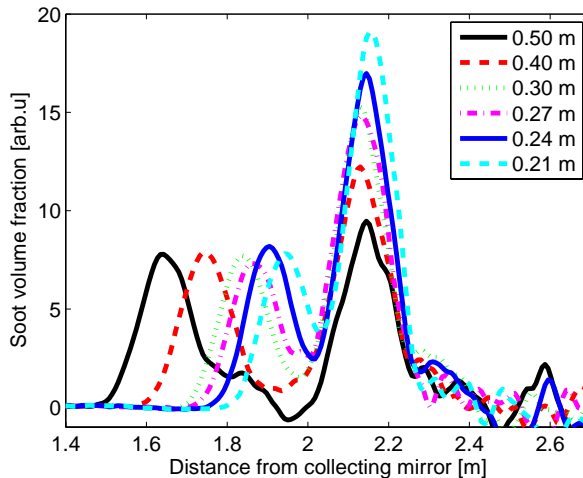

Figure 8.10 *Results from a demonstration of range resolved LII for mapping of soot volume fraction distribution. Two porous plug burners were used as soot sources, which center-to-center distance was varied, as indicated in the legend.*

At the smallest burner separation, the tail of the signal from the left flame elevates the signal of the right flame. For longer distances, the left burner with its stabilizing plate, positioned 21 mm above the burner, obscure the detector field of view, which decreases the signal received from the right flame.

The range resolution is expected to be limited by the time response of the detector, i.e. the microchannel-plate photomultiplier tube (MCP-PMT), since the rise time of LII signals excited by picosecond laser pulses is on the order of the laser pulse duration (Michelsen, 2006). The duration of the rise- and fall time of the detector is ~1 ns, which corresponds to a range resolution of 15 cm. The range resolution of this system was verified to be ~15 cm in a separate experiment. The left peak on the black curve, corresponding to a burner separation of 0.5 m, shows the LII lidar result of a relatively uniformly distributed soot source having a diameter of 6 cm. The result agrees well with the measured temporal response curve of the MCP-PMT.

Figure 8.11 shows two of the curves from fig 8.10 together with the results from the simultaneous perpendicular ICCD measurements. The latter have been convoluted with the TRF of the MCP-PMT to validate the lidar results. According to the discussion about obscured signal collection, the 0.21-m curves are expected to show good agreement with the right lidar peak being slightly overpredicted, while the same peak is expected to be underpredicted in the 0.5-m lidar curve. The expected trends are observed in the diagram.
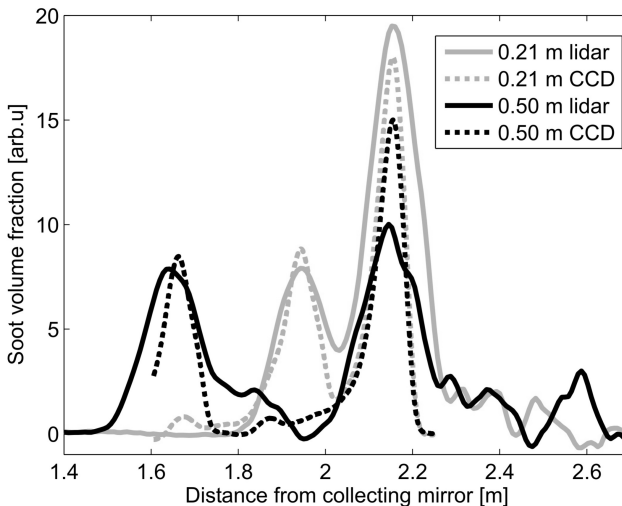
Figure 8.11 *Lidar curves (solid lines) are compared with results from perpendicular measurements to validate the lidar results.*

Chapter 9

Picosecond laser for temporal filtering

Laser sources with picosecond pulse duration opens up for new detection schemes utilizing temporal filtering. In many cases spectral filtering or polarization filtering can be used to discriminate against unwanted signal contributions, but in some cases, for example in the work by Edwards et al. (1987), where elastically scattered light interferes with the fluorescence of interest, a time filter may purify the signal.

A schematic image of signals with different time dependencies is shown in fig. 9.1, with τ being the time delay between the interfering signal and the onset of the gate function, and x representing the time jitter of the gate function relative to the signal.

9.1 Suppression of elastic scattering for fluorescence studies

If the signal of interest has a longer lifetime than the interference, the gate function may be temporally positioned to only cover the signal of interest, which is readily seen in fig. 9.1. The best possible time filter, in terms of only collecting the long lived signal, would be achieved with a gate function having as short rise time as possible, acting as an on-off button on the temporally extended signal.
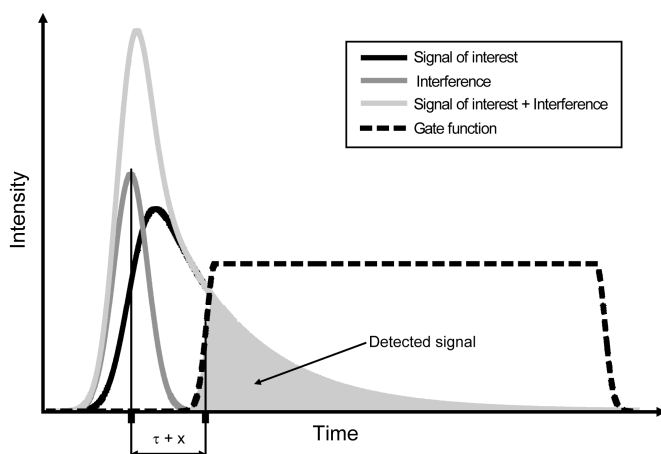
Figure 9.1 *A schematic illustration of the temporal filtering concept in a situation where the signal of interest has a longer lifetime than the interfering signal. The position of the gate function will determine the fractions collected of the signal of interest and interfering signal, respectively.*

A demonstration of the temporal filtering technique was conducted, revealing a jet of acetone vapor embedded in an aerosol of water droplets (Paper VI). The aerosol was generated by a nebulizer and the volume was illuminated with a laser sheet of 266-nm wavelength. The measurement object is schematically shown in fig. 9.2.
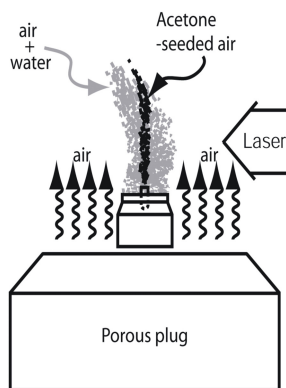
Figure 9.2 *A sketch of a measurement object used to demonstrate the temporal filtering concept. A plume of air and water mist from a nebulizer is containing an acetone jet. Temporal filtering is used to reveal the fluorescence from the acetone jet.*

After passing a spectral filter, transmitting only 1% at 266 nm (Schott, WG280), the signal was collected and detected with a gated ICCD camera having a 10-ns gate width with a characterized rise time of ~3 ns. By increasing the delay time, τ, in steps of 1 ns between each recording, the three single-shot images shown in fig 9.3 were acquired.

For the relative delay time -1.1 ns it is observed that the scattering from the water droplets is much stronger than the detected fluorescence, since merely a shadow effect is seen where the fluorescence is expected.

Increasing the delay time 2 ns, to 0.9 ns, removes the entire contribution from the droplets and reveals purely fluorescence from the acetone jet. The acetone fluorescence has a lifetime of ~1.5 ns, which might be compared with the 3-ns rise-time of the gate, thus the fraction of the total fluorescence signal captured after the gate has been temporally shifted until no scattering is observed could be expected to be quite low.

Delay Time : τ = -1.1 ns	Delay Time : τ = -0.1 ns	Delay Time : τ = 0.9 ns
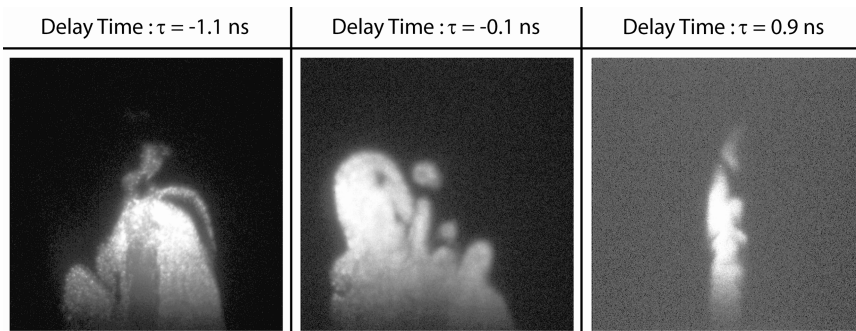
Figure 9.3 *Temporal filtering of planar LIF images. Three different delay times for the gate function were used. Scattering from the water mist dominates the two images with shortest delay times. In the image to the right all the water scattering have occurred before the opening of the gate (see fig. 9.1) and only the remaining fluorescence is observed.*

To investigate the effects of temporal filtering in a quantitative way, two parameters were defined, namely the filter transmission, $T(\tau)$, and the signal-to-signal-plus-interference ratio, SSIR(τ), ranging from 0 to 1, as a measure of the fraction of the totally detected signal originating from the signal of interest:

$$T(\tau) = \frac{I_{\text{gated}}^{\text{signal}}(\tau)}{I_{\text{ungated}}^{\text{signal}}} \qquad (8.5)$$

$$SSIR(\tau) = \frac{I_{gated}^{signal}(\tau)}{I_{gated}^{signal}(\tau) + I_{gated}^{interference}(\tau)} \tag{8.6}$$

where I^{signal} and $I^{interference}$ designate the signal of interest and the interfering signal, respectively. The ungated signal is collected using a long gate covering the whole signal.

A measurement series, recording the variables needed for calculating $T(\tau)$ and $SSIR(\tau)$ with τ varying from -10 to 10 ns, using a 10-ns gate width, was conducted. The results are plotted in fig. 9.4.
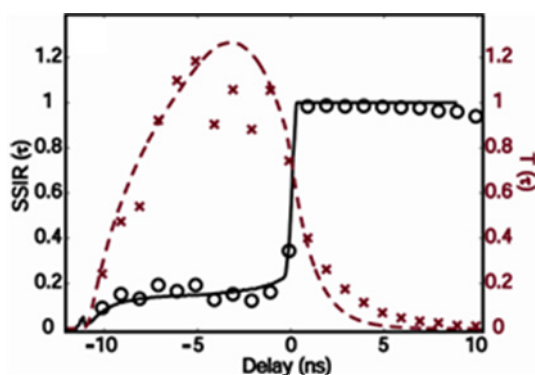
Figure 9.4 *Signal-to-signal-plus-interference ratio (SSIR) and transmission of the signal of interest (T) shown for measurements (stars and circles) and simulations (lines) of the setup illustrated in fig. 9.2.*

The lines represent the simulated performance of the filter, while the markers are measurement results. The simulations could be carried out after temporal characterization of the acetone LIF signal, the Mie scattering signal, the laser pulse, the laser pulse jitter, and the camera gate function, which is described in Paper VI.

9.2   Suppression of fluorescence signal for Raman-scattering studies

The temporal filtering function can also be used the other way around when the short lived signal is the one of interest. A large part of the long-lived signal will be

suppressed if the gate function, see fig. 9.1, is moved to the left until only the trailing edge of the gate function coincides with the signal of interest.

A typical situation in which it is attractive to detect only the initial part of the signal is when a weak Raman signal is hidden inside a spectrally broad fluorescence signal. Application of temporal filtering in such a situation was demonstrated in a Raman scattering experiment in a sample containing nitromethane, CH_3NO_2, contaminated by trace amounts of a dye solution(Rhodamine 590 in ethanol) (Levenius, 2009).

The excitation source was the picosecond Nd:YAG laser, generating pulses of 30-ps duration and 532-nm wavelength, and the signal was detected by the streak camera, averaging over 100 shots. A spectrograph (Spectral products, DKSP240) with a grating having 150 groves/mm and blaze wavelength 500 nm was positioned directly in front of the streak camera together with a holographic notch filter, OD 6, corresponding to a transmission of $e^{-6} < 0.3\%$, at 532 nm.

Since the streak camera detects the signal as a function of time, it is possible to make temporal filtering in the data postprocessing by integrating the spectrally resolved signal over a certain time range. Such processing was done to generate the spectra shown in fig. 9.5. The legend indicates the relative position corresponding to the trailing edge of the software gate function, while the leading edge is kept fixed at a time prior to the onset of the signal. When the trailing edge is moved towards earlier detection, Raman peaks of Nitromethane become visible as the amount of fluorescence decreases dramatically.

All spectra are normalized with their maximum intensities for comparison purposes. In practice, of course, all evaluated intensities are lower than in the 13.87 ns spectrum, which is, apart from the residual of elastic scattering around 0 cm^{-1} and weak contributions from Raman scattering at 3000 cm^{-1}, an almost pure fluorescence spectrum.

By moving the rising edge of the gate to a temporal position past the occurrence of Raman scattering and elastic scattering, the acquired result would be a clean fluorescence spectrum, $f(\lambda)$, as illustrated by SSIR(τ) in fig. 9.4. A cleaner Raman spectrum than the 1.31-ns spectrum, without the interfering broadband fluorescence structure, might be obtained if a normalized $f(\lambda)$ is subtracted, which was demonstrated by Ehn et al. (2012c) using ICCD cameras for temporal filtering of two dimensional images.The best possible $T(\tau)$ achievable for the fluorescence signal when SSIR=1 is dependent on laser pulse duration and limited by the relation between the slope of the trailing edge of the laser pulse and the decay constant of the fluorescence.
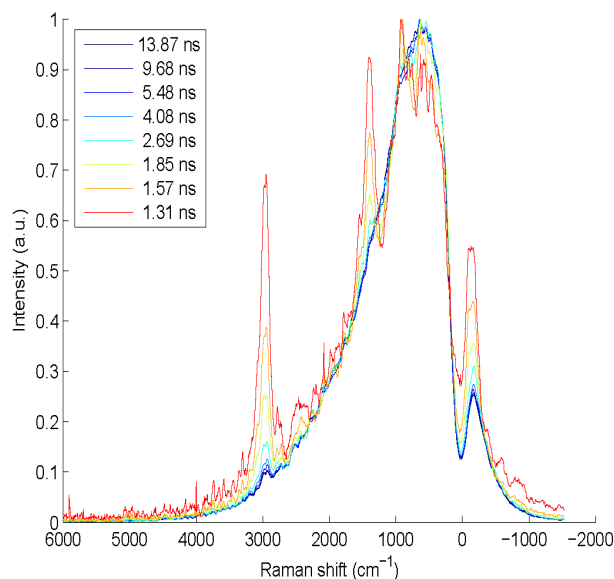
Figure 9.5 *Raman spectra recorded in nitromethane contaminated by a trace amount of a dye solution (Rhodamine 590). The different spectra correspond to software gate functions with different length. The leading edge of the gate functions is fixed, while the trailing edge is moved according to the time indicated in the legend. The spectra have been normalized with their maximum intensities. (Courtesy of Martin Levenius).*

However, the ultimate SSIR for a Raman signal, compare with $1-\mathrm{SSIR}(\tau)$ in fig. 9.4, is not expected to be as strongly influenced by the laser pulse duration, since the rising edge of both the Raman and the fluorescence signal has a risetime governed by the temporal shape of the laser pulse with the fluorescence rise time being ~2-3 times longer. The limit will instead be dictated by the ratio between the peak fluorescence signal and the maximum Raman signal. To achieve the ultimate $T(\tau)$ while having maximum $\mathrm{SSIR}(\tau)$, the trailing edge of the gate function should be as short as possible.

An example of Raman imaging of a levitated water droplet in a bath gas consisting of nitrogen and toluene is shown in fig. 9.6. The laser wavelength 266 nm was used and a dimethylformamide liquid filter was positioned in front of the camera for suppression of the elastically scattered light. When a longer camera gate, 20 ns, was used, a greater part of the toluene fluorescence signal was detected and the water droplet was not discernible, as can be seen in fig. 9.6a. Figure 9.6b shows the result obtained when a short gate function of 2 ns was used, letting the

trailing edge of the gate cut off the majority of the fluorescence tail. It can be seen that the Raman signal from water reveals the presence of the water droplet embedded in the toluene gas. The fluorescence lifetime of toluene in nitrogen bath gas is 82 ns (Hickman et al., 1996), which makes Raman imaging using temporal filtering an extremely powerful tool.
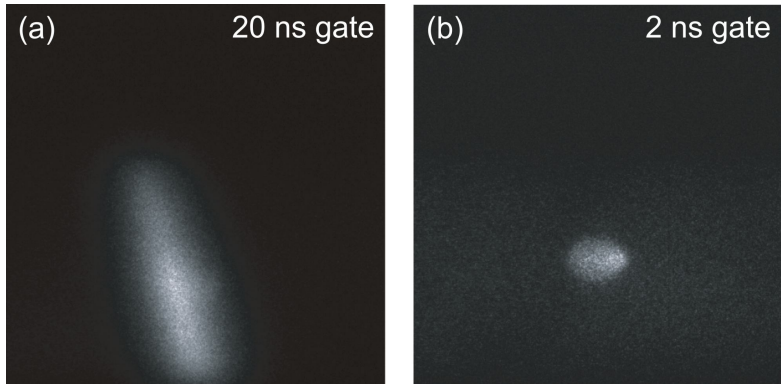
Figure 9.6 *Images of a levitated water droplet surrounded by toluene vapor. In (a) a longer gate, 20 ns, is used to acquire a greater part of the toluene fluorescence. In (b) a short gate, 2 ns, is applied, utilizing the sharp trailing edge of the gate to cut off the major part of the fluorescence tail, which reveals the Raman scattering from the droplet (Courtesy of Andreas Ehn).*

Chapter 10

Conclusions

The main conclusion drawn from the work presented in this thesis is that laser-based combustion diagnostics utilizing picosecond pulses is suitable for large-scale measurement objects in general, and objects restricted to one optical access in particular.

The ultimate range resolution of the ps-lidar measurements was found to be 4.6 mm, limited by the laser pulse duration. By using a state-of-the-art streak camera together with laser pulses of a few picoseconds duration, it might be possible to obtain a range resolution on the order of parts of millimeters. Such a range resolution opens up for single-ended measurements on smaller objects as well, where the hard target return from the rear surface of the object will probably be the major challenge.

Picosecond lidar yields range resolved results for:

- Quantitative Rayleigh scattering thermometry (RST)
- Quantitative species detection employing differential absorption lidar (DIAL)
- Qualitative species detection using laser-induced fluorescence (LIF)
- Qualitative particle volume fraction measurements using Mie scattering
- Qualitative soot volume fraction measurements using laser-induced incandescence (LII).

Rayleigh scattering thermometry yields excellent results from measurements in ambient laboratory air. Furnace measurements, validated with carefully performed

thermocouple measurements, have shown that the agreement is within a few percent. Rayleigh scattering thermometry in ambient air is found to be less prone to spurious Mie scattering when performed in a lidar configuration, i.e. collection of backscattering, than for traditional setups where the signal is collected perpendicularly to the direction of the laser beam. There is currently no comprehensive explanation for this feature, thus further studies are needed, but it seems reasonable to assume that it is linked to the properties of the scattering phase function. The method is applicable in combustion environments for quantitative measurements as long as the particulate matter concentration is kept low (for premixed ethylene flames this means that $\phi \leq 1.3$), which has to be verified carefully.

Picosecond DIAL can detect down to 5% fractional absorption, which for example corresponds to 40 ppm ammonia over a 15-cm path length at ambient conditions. This minimum detectable fractional absorption is in good agreement with other lidar and absorption measurements. The absorption is dependent on the product of range resolution (determining absorption path length) and absorption cross section. DIAL should be possible to use in particle laden regions, particularly if the particles are uniformly distributed. In such cases, particle scattering will actually be advantageous since it increases the signal-to-noise ratio in the recorded lidar curves as long as light extinction is not too severe.

Laser-induced fluorescence enables qualitative trace species mapping for much lower concentrations than DIAL. If a DIAL measurement is used to determine the average concentration along the line of sight, that result might be used to calibrate the concentration distribution obtained from LIF measurements.

For soot diagnostics, ps-lidar can be used in combination with LII for qualitative measurement of soot volume fraction distributions down to levels of 1 ppm.

Picosecond lidar can be used as a temporal filter for measurements of prompt signals from remote signal sources swamped in its own fluorescence. It can also be used the other way around, i.e. for suppression of intense scattering from an object close to a source having a long-lived signal of interest.

In summary, ps-lidar enables studies within the field of energy science that, to this day, have not been possible to realize in any other way.

Chapter 11

Outlook

After several years of development, ps-lidar has in the latter part of the work shown exciting results and potential for more to come.

Particularly the possibility to use two tunable picosecond laser sources has opened up for a variety of new measurement opportunities. All species measured with atmospheric DIAL are, in principle, possible to detect also with ps-DIAL. Further on, all fluorescing molecules exhibiting fluorescence signal intensities at least comparable with the Rayleigh scattering signal intensity may be probed and mapped qualitatively.

The preliminary results of the work on Raman scattering was obtained using the harmonics of an Nd:YAG laser. Due to the low cross sections of Raman processes, the studies were restricted to liquid samples. As resonance Raman scattering has been shown to provide a dramatic enhancement of the Raman cross sections, exciting possibilities may arise with a tunable laser source available that might allow for range resolved detection of species in gaseous phase.

Soot diagnostics using the LII ps-lidar concept may be of direct use in practical applications. Since backward detection of LII has already been applied outside laboratories, limited to line-of-sight measurements though, this concept could provide new interesting possibilities in such situations.

Although ps-lidar has been used for practical diagnostics in room-fire experiments, it would be of great interest to bring the system out in the real world of power plants and boilers, which it has been developed for. Measurement of spatial distributions of parameters such as particulate matters (Mie scattering) and

species concentrations (DIAL) is a challenging task that completed really could deliver new knowledge to the combustion community as well as important feedback for further development of ps-lidar.

In the development work there are several interesting aspects that deserve closer attention. One of the aspects that is of fundamental theoretical nature is the impact of properties such as depolarization of scattered light, and scattering phase function of particulate matter, which is an essential interference source in Rayleigh scattering thermometry. Another area for further investigations is practical solutions for and demonstrations of two-dimensional lidar in larger planes than those demonstrated so far, which have been limited along one axis to the ~1-cm diameter of the collimated laser beam. It would also be of interest to investigate the far range limit (distance from lidar telescope) for highly range resolved ps-lidar measurements (sub centimeter) while for example enhancing the obtained signal with the use of a Fresnel lens.

A more farfetched but exciting development would be to combine the idea of white-light lidar (Kasparian et al., 2003) with combustion research. The white-light filaments, based on femtosecond laser pulses, opens up for simultaneously detection of several species in combination with an order of magnitude increased scattering in the backward direction.

In a wider context, for ps-lidar to gain interest and be of practical use to researchers and engineers in the combustion community, it is of utmost importance to find easy and cheap solutions for how to implement ps-lidar diagnostics in practical applications, while continuing to demonstrate its feasibility in new applications and for detection of even more species of interest.

Acknowledgements

For six years I have been a part of the division of combustion physics. My life during these years has been exciting in a tremendous amount of ways. During the first years I had the possibility to spend as much time as needed on every task that appeared, with the pros and cons that meant, while the last years, with the responsibility and new priorities that children have brought to my life, have taught me how to produce and finish work in an effective way I did not now I was capable of.

Throughout these different approaches to the work and the work place I have found combustion physics a really good place to work at, with a friendly and stimulating work climate. I think that somewhere between sixty and seventy people have worked at the division during these years and I would truly like to thank you all for that you have contributed to make my time at the division to a pleasure.

Joakim Bood was the one who choose me for the position and he has also been my supervisor during the work. For me, he is a great source of knowledge about physics in general and laser diagnostics in particular and he has always been willing to share it in a pedagogical manner. I have not worked with anyone else being as quick as him when it comes to producing nice plots of preliminary data from the lab, directly revealing the measurements level of success. Without the scientific support and foundation Joakim has given me, I would not have been able to reach the level of scientific research where I am today. He is also a very good friend, and since he moved to Malmö I have had the opportunity to spend a couple of days at his balcony, with a nice view of Öresund, discussing physics and other more or less essential topics.

Marcus Aldén has been my assisting supervisor and he is also the head of the division. I would like to thank him for being the heart of the stimulating environment we work in, and for letting me be a part of that. He has always, with

short notice, been available for discussions about the greater perspective of the work and research I have been involved in.

Olof Johansson shared office with me for five years. He began his career at the division exactly the same day as I did, but he finished his way ahead of me. At work he was a never ending source of mathematical skills that I have never possessed. What I could do using matlab for two days, Olof could do with a slide-rule in two minutes. We had the opportunity to discuss matters ranging from utopian political systems to figurines, but maybe more often, as he proclaimed his passion for Canadian ice hockey in general, and Peter Forsberg in particular, we had the chance to bicker about sports. He is a great friend, obsessed with nicknames, but nevertheless, always willing to help out, even with the most troublesome of tasks.

Andreas Ehn is one of the most complicated acquaintances I have. At many levels I think we have a lot in common, but in many ways we organize our thinking and arguing surprisingly different. I think that makes him an important source of learning different ways of handling things and dealing with life for me. He is really clever and stubborn as few others, which combined with being the greatest teaser of them all and caring enormously for people around him makes him a valuable friend.

My production of scientific work has involved several other people to which I am grateful. I would especially like to mention some of them.

Christian Brackmann came as breath of spring and assisted our growing group with senior features. He has been a high performing sparring partner for me throughout the experimental work and manuscript preparation of the last measurement campaigns. He has sacrificed his leisure time to let me finish our manuscripts in time. **Malin Jonsson**, who joined our research group during the latter part of my work and with great enthusiasm has helped me with several measurements. **Jonathan Wahlqvist**, who had to endure my eager work with the room-fire manuscript, supplying me with the information and data I needed, and listen to my never-ending suggestions regarding possible interpretation of our results. **Sven-Göran Pettersson** introduced me to and helped me with many complicated aspects of geometric optics. He also let me try his bike, *raketen*, which was an odd experience. **Martin Algotsson**, who almost carried the engine on his shoulder to get it working during our attempts to contribute to the most efficient

diesel-engine in the world. **Edouard Berrocal**, provided with a large amount of French humor and driving force, brought us into the world of light scattering spheres, transforming our lab to a forward-backward-everywhere scattering experiment for a couple of weeks. **Mattias Richter** came in during his vacation one summer and showed his huge ability to act while helping me and Olof aligning the laser referred to as the *ice machine*. Moreover, he has been helping out with all engine related questions I have encountered. **Rutger Lorensson**, who is handy as no one else and very enjoyable talking to. If he had to, he could probably build a car using the crowd of interesting equipment being kept in the basement. He has helped out several times without notice, solving practical issues with experimental equipment that without his help would have hampered the continuing of whole measurement campaigns. **Ronald Whiddon**, who despite a packed schedule, has solved several electronic- computer- and language related issues in a rapid and professional way. **Tomas Leffler** showed never ending enthusiasm and handiness, creating a measurement object that could vaporize salt without vaporizing itself, which finally, after a multitude of previous discouraging tries, led to a successful experiment. **Robert Collin** has made his best to keep me alive, handling the sometimes a bit ungrateful task of controlling all safety aspects regarding the laboratory work.

I have spent some time with **Henrik Bladh**, **Frederik Ossler**, **Per-Erik Bengtsson**, **Johannes Lindén**, and **Elias Kristensson** through the years. They are all artistic and humble persons with interesting personalities and I have enjoyed being with these talented people a lot.

Sven-Inge Möller and **Andreas Lantz** have always been ready for a laugh. They are the kind of persons who enlighten the working days for their colleagues.

In connection with one of the Gordon conferences I spent a couple of exciting days in New York with a dynamic duo consisting of **Johan Zetterberg** and **Jonathan Johnsson**. We had a nice time, although they tried to sleep through the whole stay. I hope our route from New York to Waterville Valley, even though it gave us an interesting insight in the New Hampshire countryside, will never be used by anyone without a terrain vehicle again. During two other conference trips to Florida and Montreal I spent some time with **David Sedarsky**, who is a really helpful and language-interested friend.

Acknowledgements

I have had the opportunity to supervise two undergraduate students, **Linus Frantzich** and **Martin Levenius**, who both contributed with material and work that have helped me. They also gave me a chance of practicing the noble art of teaching.

Kajsa Larsson has been sharing office with me the last period of time when I have been out of office, doing experimental work in the lab or thesis writing at home, most of the time. She is very easy to be around and has shown a friendly understanding for the lack of company at the office I may have caused.

Handling the administrative duties as a newcomer, may tend to be an insurmountable task. **Anneli Nilsson-Ahlm** did a superior job, guiding me through this and welcoming me to the division. **Cecilia Bille** has booth been a splendid help and friendly chit-chatter over the years. **Eva Persson** is probably my number one receiver of forms of different sizes, colors, and lengths, which she has handled perfectly. **Minna Ramkull**, a major contributor to the joyfulness at the division, has helped with all kind of administrative issues in the late part of my time at the division.

During the work with my master thesis I had the opportunity to have **Sune Svanberg** as supervisor. His passion for conveying the core of physics, to understand it in a way that makes sense, has been truly inspiring and has indeed influenced both my choice of working with applied molecular physics and my way of thinking about physics.

My senior high school physics teacher **Mikael Stendrup** taught me not only physics, but also how to like physics and science, which has been of great importance for my career choices. By his concern for us students, he showed how to be a good fellow human and how to enjoy life.

When I started the undergraduate physics studies I came in touch with many sharp minds. One of them, who became my friend, was **Klas Bogsjö,** who at that time was a modest man, enjoying what the world had to offer. I tried to keep in pace with him while we were struggling with a lot of plaguesome work together. Especially matlab was a source of everlasting pain for some years. I think that one of our friends, **Jörgen Larsson**, with his fighting spirit during these years, showed us youngsters how to aim for the stars and only be limited by yourself, not by any external circumstances.

I would also like to thank all friends that have filled my life with so many interesting experiences not related to physics: music, sport, travel and much more. They have all supplied me with energy, not to drop off during the vast years of studies leading to this final academic degree.

I would not have come this far without my family: **mamma**, **pappa** och **Henke**. They have let me do what I have been destined for, with their unaffected love and support, although my studies and work have surpassed their sphere of interest very long ago. I am very grateful for the financial and practical support my parents give at this moment to prepare the best possible celebration when this work is finished.

My greatest source of energy and inspiration, during the last years of the work with this thesis, has been the ones I am living with: **Sara**, **Ville** and **Vera**.

Sara has, for several months, taken care of our home and children, more or less alone, while I have been stuck in the basement day and night writing, calculating, submitting, and listening to *Hunger Hotell* over and over, and she has really been, and still is, the best. I look so much forward to returning to my life, as I used to know it, with her, after this work is finished.

Ville has been the only one working with me in the basement. Occasionally, he has come down to sit beside me and work, and at the moment I have thirty-three fantastic drawings here at the desk. During the intense part of this work, at a short break in the garden, he delivered the following quote: "Humlor bränns inte, för de har inga tändstickor i händerna", which turns the stringent logic I have been working with into a strange kind of relative concept.

The unconditional smiles Vera gives me when spotting me, despite me being absent so much the last months, have made it easier for me fulfilling the work.

References

Aldén, M., and Wallin, S. (1985)
   CARS experiments in a full-scale (10 × 10 m) industrial coal furnace
      Appl. Opt. **24**, 3434-3437

Aldén, M., Bood, J., Li, Z., and Richter, M. (2011)
   Visualization and understanding of combustion processes using spatially and temporally resolved laser diagnostic techniques
      Proc. Comb. Inst. **33**, 69-97

Aldén, M., Edner, H., Holmstedt, G., Svanberg, S., and Högberg, T. (1982)
   Single-pulse laser-induced OH fluorescence in an atmospheric flame, spatially resolved with a diode array detector
      Appl. Opt. **21**, 1236-1240

Andresen, P., Bath, A., Gröger, W., Lülf, H., Meijer, G., and ter Meulen, J. (1988)
   Laser-induced fluorescence with tunable excimer lasers as a possible method for instantaneous temperature field measurements at high pressures: checks with an atmospheric flame
      Appl. Opt. **27**, 365-378

Ansmann, A., Riebesell, M., Wandinger, U., Weitkamp, C., Voss, E., Lahmann, W., and Michaelis, W. (1992)
   Combined Raman elastic-backscatter LIDAR for vertical profiling of moisture, aerosol extinction, backscatter, and LIDAR ratio
      Appl. Phys. B, **55**, 18-28

Argall P., and Sica, R. (2002)
   Encyclopedia of Imaging Science and Technology
      Ed. Hornak, J.
      John Wiley & Sons Inc, pp. 869

References

Banwell, C., and McCash, E. (1994)
Fundamentals of molecular spectroscopy, 4th ed.
McGraw-Hill, Maidenhead (UK)

Barat, R., Longwell, J., Sarofim, A., Smith, S., and Bar-Ziv, E. (1991)
Laser Rayleigh scattering for flame thermometry in a toroidal jet stirred combustor
Appl. Opt. **30**, 3003-3010

Barlow, R., Dibble, R., and Lucht, R. (1989)
Simultaneous measurement of Raman scattering and laser-induced OH fluorescence in nonpremixed turbulent jet flames
Opt. Lett. **14**, 263-265

Bechtel, J., and Teets, R. (1979)
Hydroxyl and its concentration profile in methane-air flames
Appl. Opt. **18**, 4138-4144

Bengtsson, P.-E., and Alden, M. (1990)
Optical investigation of laser-produced C_2 in premixed sooty ethylene flames
Combust. Flame. **80**, 322-328

Bergano, N., Jaanimagi, P., Salour, M., and Bechtel, J. (1983)
Picosecond laser-spectroscopy measurement of hydroxyl fluorescence lifetime in flames
Opt. Lett. **8**, 443-445

Bladh, H., Johnsson, J., and Bengtsson, P.-E. (2008)
On the dependence of the laser-induced incandescence (LII) signal on soot volume fraction for variations in particle size
Appl. Phys. B **90**, 109–125

Born, M., and Wolf, E. (1980)
Principles of optics, 6th ed.
Oxford: Pergamon

Boyd, R. (1992)
Nonlinear optics
Academic press, San Diego

Bradley, D., Liddy, B., and Sleat, W. (1971)
Direct linear measurement of ultrashort light pulses with a picosecond streak camera
Opt. Commun. **2**, 391-395

Bransden, B., and Joachain, C. (2003)
Physics of atoms and molecules
Pearson Education, Prentice Hall

Cavalcabo, G., Fiorina, L., Monguzzi, M., Nice, P., and Zanzottera, E. (1993)
Development of a lidar system for the diagnostics of combustion and emissions in a power plant
Proc. SPIE 1717, 142–148

Cheng, B., Lu, H-C., Chen, H-K., Bahou, M., Lee, Y-P., Mebel, A., Lee, L., Liang, M-C., and Yung, Y. (2006)
Absorption cross sections of NH_3, NH_2D, NHD_2, and ND_3 in the spectral range 140-220 nm and implications for planetary isotopic fractionation
The Astrophysical Journal **647**, 1535-1542

Crosley, D. (1989a)
Semiquantitative laser-induced fluorescence spectroscopy for combustion diagnostics
Combust. Flame. **78**, 153-167

Crosley, D. (1989b)
Rotational and translational effects in collisions of electronically excited diatomics hydrides
J. Phys. Chem. **93**, 6273-6289

Daily, J. (1977)
Saturation effects in laser induced fluorescence spectroscopy
Appl. Opt. **16**, 568-571

Dibble, R., and Hollenbach, R. (1981)
Laser Rayleigh thermometry in turbulent flames
Proc. Comb. Inst., **18**, 1489-1499

References

Demtröder, W. (1993)
    Laser spectroscopy
        Springer-Verlag, Heidelberg

Duncan, A. (1935)
    The ultraviolet absorption spectrum of ammonia
        Phys. Rev. **47**, 822-827

Eberhard, W. (2010)
    Correct equations and common approximations for calculating Rayleigh scatter in pure gases and mixtures and evaluation of differences
        Appl. Opt. **49**, 1116-1130

Edwards, T., Weaver, D., and Campbell, D. (1987)
    Laser-induced fluorescence in high pressure solid propellant flames
        Appl. Opt. **26**, 3496-3509

Eckbreth, A. (1996)
    Laser diagnostic for combustion temperature and species, 2nd ed.
        Gordon and Breach Publishers, Amsterdam

Edwards, T., Weaver, D., and Campbell, D. (1987)
    Laser-induced fluorescence in high pressure solid propellant flames
        Appl. Opt. **26**, 3496-3509

Ehlerding, A., Johansson, I., Wallin, S., and Östmark, H. (2011)
    Resonance-enhanced Raman spectroscopy on explosives vapor at standoff distances
        International Journal of Spectroscopy, **2012**, 158715

Ehn, A., Johansson, O., Arvidsson, A., Li, B., Aldén, M., and Bood, J. (2012a)
    Single-laser shot fluorescence lifetime imaging on the nanosecond timescale using a dual image and modeling evaluation algorithm.
        Opt. Express, **20**, 3043-3056

Ehn, A., Jonsson, M., Johansson, O., Aldén, M., and Bood, J. (2012b)
    Quantitative oxygen concentration imaging in toluene atmosphere using dual imaging with modeling evaluation
        Manuscript submitted to Exp. Fluids.

Ehn, A., Levenius, M., Jonsson, M., Aldén, M., and Bood, J. (2012c)
Temporal filtering in spontaneous Raman studies
Manuscript submitted to Journal of Raman spectroscopy

Feynman, R., Leighton, R., and Sands, M. (1965)
The Feynman lectures on physics. Vol 2, chap. 32, sect. 3
Addison-Wesley, Reading, MA

Forsberg, C., Broström, M., Backman, R., Edvardsson, E., Badiei, S., Berg, M., and Kassman, H. (2009)
Principle, calibration, and application of the in situ alkali chloride monitor
Rev. Sci. Instrum. **80**, 023104

Fujikawa, T., Fukui, K., Hattori, Y., and Akihama, K. (2006)
2-D Temperature Measurements of Unburned Gas Mixture in an Engine by Two-line Excitation LIF Technique
SAE Technical Paper 2006-01-3336

Fujii, T., and Fukuchi, T. (Eds.) (2005)
Laser remote sensing
Taylor & Francis, London

Gai, M., Gurioli, M., Bruscaglioni, P., Ismaelli, A., and Zaccanti, G. (1996)
Laboratory simulations of lidar returns from clouds
Appl. Opt. **35**, 5435–5442

Glassman, I. (1996)
Combustion
Academic press

Hadef, R., Geigle, K., Meier, W., and Aigner, M. (2010)
Soot characterization with laser-induced incandescence applied to a laminar premixed ethylene air flame
Int. J. Therm. Sci. **49**, 1457-1467

Halldórsson, T., and Langerholc, J. (1978)
Geometrical form factors for the lidar function
Appl. Opt. **17**, 240-244

References

Harms, J. (1979)
  Lidar return signals for coaxial and noncoaxial systems with central obstruction
    Appl. Opt. **18**, 1559-1566

Harsdorf, S., Janssen, M., Reuter, R., Toeneboen, S., Wachowicz, B., and Willkomm, R. (1999)
  Submarine lidar for seafloor inspection
    Meas. Sci. Technol. **10**, 1178–1184

Haus, H. (2000)
  Mode-locking of lasers
    IEEE Journal on Selected Topics in Quantum Electronics, **6**, 1173-1185

Hecht, E. (2002)
  Optics, 4th ed.
    Addison-Wesley

Heiser, J., and Sedlacek, A. (2006)
  Using LIDAR to measure perfluorocarbon tracers for the verification and monitoring of cap and cover systems
    Water, Air, Soil Pollut. **170**, 345-357

Hilborn, R. (1982)
  Einstein coefficients, cross sections, f values, dipole moments, and all that
    Am. J. Phys. **50**, 982-986

Johansson I., Ehlerding, A., Wallin, S., and Östmark, H. (2010)
  Resonance enhanced Raman spectroscopy for explosives detection
    Technical Report, FOI-R--2976—SE, FOI, Swedish Defense Research Agency

Kasparian, J., Rodriguez, M., Méjean, G., Yu, J., Salmon, E., Wille, H., Bourayou, R., Frey, S., André, Y.-B., Mysyrowicz, A., Sauerbrey, R., Wolf, J.-P., and Wöste, L. (2003)
  White-Light Filaments for Atmospheric Analysis
    Science **301**, 61-64

Kiefer, J., Ewart, P. (2011)
  Laser diagnostics and minor species detection in combustion using resonant four-wave mixing
    Prog. Energy. Combust. Sci. **37**, 525-564

Kohse-Höinghaus, K. (1994)
  Laser Techniques for the quantitative detection of reactive intermediates in combustion systems
    Prog. Energy combust. Sci. **20**, 203-279

Kovalev, V., and Eichinger, W. (2004)
  Elastic Lidar
    John Wiley & Sons, Inc.

Kychakoff, G., Howe, R., Hanson, R., and McDaniel, J. (1982)
  Quantitative visualization of combustion species in a plane
    Appl. Opt. **21**, 3225-3227

Leonard, D. (1967)
  Observation of Raman scattering from the atmosphere using a pulsed nitrogen ultraviolet laser
    Nature, **216**, 142-143

Lucht, R., Sweeney, D., and Laurendeau, N. (1980)
  Balanced cross-rate model for saturated molecular fluorescence in flames using a nanosecond pulse length laser
    Appl. Opt. **19**, 3295-3300

Luong, M., Zhang, R., Schulz, C., and Sick, V. (2008)•
  Toluene laser-induced fluorescence for in-cylinder temperature imaging in internal combustion engines
    Appl. Phys. B **91**, 669–675

Loeb, L. (1961)
  The kinetic theory of gases
    Dover publications, New York

References

Mansour, S. (1993)
> *Two-plane two-dimensional Rayleigh thermometry technique for turbulent combustion*
>> Opt. Lett. **18**, 537-539

Maricq, M., Harris, S., and Szente, J. (2003)
> *Soot size distributions in rich premixed ethylene flames*
>> Combust. Flame. **132**, 328-342

Mazzoleni, C., Kuhns, H., and Moosmüller, H. (2010)
> *Monitoring Automotive Particulate Matter Emissions with LiDAR: A Review*
>> Remote Sens. **2**, 1077-1119

Michelsen, H. (2006)
> *Laser-induced incandescence of flame-generated soot on a picosecond time scale*
>> Appl. Phys. B **83**, 443-448

Measures, R. (1984)
> *Laser remote sensing: Fundamentals and applications*
>> John Wiley & Sons

Melton, L. (1984)
> *Soot diagnostics based on laser heating*
>> Appl. Opt. **23**, 2201-2208

Miles, R., Lempert, W., and Forkey, J. (2001)
> *Laser Rayleigh scattering*
>> Meas Sci Technol **12**, R33-R51

Namer, I., and Schefer, R. (1985)
> *Error estimates for Rayleigh scattering density and temperature measurements in premixed flames*
>> Expts. Fluids **3**, 1-9

Ohe, S. (n.d)
> *Distillation, Vapor pressure, Vapor-liquid Equilibria*
>> http://www.s-ohe.com.

Ossler, F., Metz, T., Martinsson, L., and Aldén, M. (1998)
Two-dimensional visualization of fluorescence lifetimes by use of a picosecond laser and a streak camera
Appl. Opt. **37**, 2303-2314

Osterink, L., Foster, J. (1968)
A mode-locked Nd:YAG laser
J. Appl. Phys. **39**, 4163-4165

Pedrotti, F., and Pedrotti, L. (1996)
Introduction to optics, 2nd ed.
Prentice Hall, New Jersey

Pettersson, A., Johansson, I., Wallin, S., Nordberg, M., Östmark, H. (2009)
Near real-time standoff detection of explosives in a realistic outdoor environment at 55 m distance
Propellants Explos. Pyrotech. **34**, 297 – 306

Raman, C., and Krishnan, K. (1928)
A new type of secondary radiation
Nature **121**, 501-502

Ray, M., Sedlacek, A., and Wu, M. (2000)
Ultraviolet mini-Raman lidar for stand-off, in situ identification of chemical surface contaminants
Rev. Sci. Instrum. **71**, 3485-3489

Reif, F. (1965)
Fundamentals of statistical and thermal physics
McGraw Hill, Singapore

Rosmus, P., Botschwina, P., Werner, H., Vaida, V., Engelking, P., and McCarthy, M. (1987)
Theoretical A1A"2–X1A1 absorption and emission spectrum of ammonia
J. Chem. Phys. **86**, 6677-6692

References

Santoro, R., and Shaddix, C. (2002)
  Applied Combustion Diagnostics
    Eds. Kohse-Köinghaus, K., and Jeffries, J.
    Taylor & Francis, London, pp. 252–286

Sappey, A., Howell, J., Masterson, P., Hofvander, H., Jeffries, J.B., Zhou, X., and Hanson, R. K. (2004)
  Determination of O_2, CO, H_2O Concentrations and Gas Temperature in a Coal-Fired Utility Boiler Using a Wavelength-Multiplexed Tunable Diode Laser Sensor
    in Abstracts of Work-In-Progress Posters of the 30th International Symposium on Combustion. The Combustion Institute

Schelev, M., Richardson, M., and Alcock, A. (1971)
  Image-converter streak camera with picosecond resolution
    Appl. Phys. Lett. **18**, 354-357

Schulz, C., and Sick, V. (2005)
  Tracer-LIF Diagnostics: Quantitative Measurement of fuel concentration, temperature and air/fuel ratio in practical combustion situations
    Prog. Energ. Combust. Sci. **31**, 75

Schwarzwald, R., Monkhouse, P., and Wolfrum, J. (1987)
  Picosecond fluorescence lifetime measurement of the OH radical in an atmospheric pressure flame
    Chem. Phys. Let. **142**, 15-18

Schulz, C., Kock, B. F., Hofmann, M., Michelsen, H., Will, S., Bougie, B., Suntz, R., and Smallwood, G. (2006)
  Laser-induced incandescence: recent trends and current questions
    Appl. Phys. B **83**, 333–354

Sharma, S., Roy, A. (2000)
  New approximate phase functions: test for nonspherical particles
    JQSRT. **64**, 327-337

Steinacker, J., Henning, T., Bacmann, A., and Semenov, D. (2003)
  3D continuum radiative transfer in complex dust configurations around stellar objects and active galactic nuclei. I. Computational methods and capabilities
    A&A **401**, 405–418

Stettner, R., Bailey, H., and Silverman, S. (n.d)
: *Three dimensional flash ladar focal planes and time dependent imaging*
  Advanced Scientific Concepts, Inc. Santa Barbara, CA

Sugimoto, N. (1999)
: *Feasibility of a lidar utilizing the glory for measuring particle size of water clouds*
  Optical Review **6**, 539-544

Sutton, J., and Driscoll, J. (2004)
: *Rayleigh scattering cross sections of combustion species at 266, 355, and 532 nm for thermometry applications*
  Opt. Lett. 29, 2620-2622

Svanberg, S. (2001)
: *Atomic and molecular spectroscopy basic aspects and practical applications, 3rd ed.*
  Springer-Verlag, Heidelberg

Svelto, O. (1989)
: *Principles of lasers, 4th ed.*
  Plenum press, New York

Seyfried, H., Särner, G., Omrane, A., Richter, M., Schmidt, H., and Aldén, M. (2005)
: *Optical diagnostics for characterization of a full-size fighter-jet afterburner*
  Proceedings of the ASME Turbo Expo, 813-819

Thurber, M. (1999)
: *Acetone laser-induced fluorescence for temperature and multiparameter imaging in gaseous flows*
  Topical Report TSD-120, Stanford University

Turns, S. (2000)
: *An introduction to combustion: concepts and applications, 2nd ed*
  McGraw-Hill, Singapore

Versluis, M., Georgiev, N., Martinsson, L., Aldén, M., and Kröll, S. (1997)
: *2-D absolute OH concentration profiles in atmospheric flames using planar LIF in a bi-directional laser beam configuration*
  Appl. Phys. B, **65**, 411-417.

References

Vestin, F., Afzelius, M., Brackmann, C., and Bengtsson, P-E. (2005)
  Dual-broadband rotational CARS thermometry in the product gas of hydrocarbon flames
      Proc. Comb. Inst., **30**, 1673-1680.

Visco, A., Drake, R., Froula, D., and Glenzer, S. (2008)
  Temporal dispersion of a spectrometer
      LLNL-CONF-403770, High Temperature Plasma Diagnostics
      Albuquerque, NM, United States

Wang, H., Frenklach, M. (1991)
  Detailed reduction of reaction mechanisms for flame modeling
      Combust. Flame. **87**, 365-370

Weitkamp, C. (ed.) (2005)
  Lidar range-resolved optical remote sensing of the atmosphere
      Springer Verlag, Berlin-Heidelberg

Wu, J., Song, K.-H., Litzinger, T., Lee, S.-Y., Santoro, R., Linevsky, M., Colket, M., and Liscinsky, D. (2006)
  Reduction of PAH and soot in premixed ethylene–air flames by addition of ethanol
      Combust. Flame. **144**, 675-687

Young, A. (1981)
  Rayleigh scattering
      Appl. Opt. **20**, 533-535

Zhao, F., and Hiroyasu, H. (1993)
  The Application of laser Rayleigh scattering to combustion diagnostics
      Prog. Energy Combust. Sci. **19**, 447-485

Summary of papers

Paper I

The features of picosecond lidar (ps-lidar), as a candidate for single-ended measurements on inaccessible large-scale combustion-related measurement objects, were investigated, demonstrated, and characterized in this paper. The range resolution of a ps-lidar system utilizing a streak-camera was demonstrated to be 0.46 cm, which in most situations may be considered high enough for temperature- and species mapping in the aforementioned objects. Temperature measurements using Rayleigh scattering thermometry were conducted on lean and rich Bunsen burner flames at 2.5 m distance, revealing, through temperature images, rough information about such details as the flame front position. Two dimensional temperature measurements on a porous plug burner ethylene flame were also demonstrated for different equivalence ratios, ϕ, showing excellent agreement with temperatures obtained from CARS measurements up to $\phi = 1.3$, above which the temperatures are underestimated due to interferences from particulate matters. DIAL measurements on two acetone sources, being an often used fuel visualization agent, at 3-4 m distance were demonstrated using the second and fourth harmonics of the Nd:YAG laser, i.e. 532 and 266 nm, respectively. Number density curves showed good agreement with the expected concentration, 6.6×10^{18} cm^{-1}, due to the vapor pressure of acetone, taking the limiting experimental range resolution into account.

I was responsible, and evaluated the data, for all experiments except the DIAL experiment and data evaluation, which Joakim Bood was responsible for. I wrote the manuscript except for the DIAL part, which was written by Joakim Bood.

Paper II

Picosecond lidar may be used for measurements in a volume surrounded by highly scattering media. In such cases the detection with temporal resolution may be used to discriminate from the scattering before and after the measurement volume. To further reduce the unwanted scattering, or use the scattering for particle mapping purposes simultaneously as utilizing Rayleigh scattered light from the

measurement volume, optical suppression of signals in parts of the measurement range can be achieved. This concept was demonstrated with a highly scattering diffusion flame positioned in front of a tube furnace. Range resolved temperature curves were obtained from the furnace tube simultaneously as the particle scattering from the flame was detected within the dynamic range of the streak camera.

I was responsible for this work.

Paper III

Ammonia (NH_3) detection is of importance, since it is used for reduction of nitric oxides in boilers and furnaces. In this work picosecond differential absorption lidar (ps-DIAL) was demonstrated on NH_3, employing a tunable picosecond laser source and a photo multiplier tube providing a range resolution of 16 cm. The detection limit obtained was 40 ppm. Demonstrations of range resolved measurements with two NH_3 sources were made.

Christian Brackmann and I planned the experiments and did the experimental work. I evaluated the data except for the cross section from fig. 3, which Joakim Bood was responsible for. I wrote the manuscript except for the introduction, which Christian Brackmann was responsible for.

Paper IV

In fire safety it is of importance to measure temperature and species concentrations over large volumes. It is highly cumbersome and unpractical to use physical probes at thousands of positions simultaneously. In this work ps-lidar was proposed as an aspirant for measurements in a room-fire scenario, and a software filtering routine for improved temperature results was developed. The feasibility for doing Rayleigh temperature measurements in regions possibly contaminated with particles was investigated. Two-dimensional- quantitative temperature images and qualitative particle maps were obtained using different fire sources for a vertical plane in the doorway and a horizontal plane inside the room.

The experiment was planned in cooperation with the coauthors from the fire safety department. I was responsible for the organization and implementation of the laser diagnostic part of the experiment. Jonathan Wahlqvist was responsible for providing the measurement object, i.e. the room including fire source and for the CFD simulations. I evaluated the laser diagnostic data and wrote the manuscript except for

Section 3.2 describing the CFD simulation, which was written by Jonathan Wahlqvist.

Paper V

Laser induced incandescence (LII) is a technique used for soot diagnostics. By heating the soot particles to temperatures well above flame temperature and studying both the intensity and temporal behavior of the emitted Planck radiation, information regarding parameters such as soot volume fraction and particle size can be obtained. When combining LII with ps-lidar it is possible to do single ended range resolved soot diagnostics. In this paper it was derived how to evaluate soot volume fraction distribution from ps-lidar signals. The concept was discussed and partly experimentally verified using a porous plug burner ethylene flame. Moreover, a demonstration was made using two porous plug burners for qualitative range resolved measurements of soot volume fraction with a range resolution of 16 cm limited by the photo multiplier tube.

I planned the experiments together with Christian Brackmann. We also did the experimental work together. I was responsible for the evaluation idea and evaluated the experimental data, except for validation data recorded with an ICCD camera, which Christian Brackmann evaluated. I was responsible for writing the paper, with Christian Brackmann being responsible for the conclusions section.

Paper VI

Different types of signals that stem from various types of light-matter interaction may in some cases differ in their temporal characteristics. For example fluorescence has a lifetime on the order of 1-100 ns, while Rayleigh and Raman scattering can be considered instantaneous, which in practice means having the same duration as the laser pulse. If the signals of interest are spectrally overlapping, the standard method of using spectral filters for separating the signals is not applicable. In these cases it may be useful to record the signals time resolved, employing a picosecond laser source, to be able to do temporal filtering of the signals. The same principle, i.e. choosing what temporal part of a signal to collect, can be used for imaging, using a temporally gated ICCD camera having a steep gate function. This was demonstrated for toluene flow visualization in two measurement setups, namely close to a surface emitting interfering radiation, and inside a steam of water droplets. A mathematical model of the signal was provided

and validated. The model contains parameters, such as camera gate characteristics, time jitter, laser pulse duration, and signal- and interfering signal characteristics.

Andreas Ehn was main responsible for this work. We planned the experiments together and I was involved in the experimental work and some of the image evaluation. The mathematical model and the validation of it that was Andreas Ehn's work though. Joakim Bood and Andreas Ehn wrote the manuscript after having planned the layout of the manuscript together with me.